Materials Advances

ROYAL SOCIETY OF CHEMISTRY

PAPER

View Article Online
View Journal

Cite this: DOI: 10.1039/d5ma01177a

Tunable multifunctionality in $BaTiO_3$–$La_{0.835}Na_{0.165}MnO_3$ composites: from UV-to-visible light absorption and nonmagnetism to room-temperature ferromagnetism

Lozil Denzil Mendonca,[a] El Kebir Hlil[b] and Mamatha D. Daivajna *[a]

The composites of ferroelectric $BaTiO_3$ and ferromagnetic $La_{0.835}Na_{0.165}MnO_3$, denoted as (1−*x*)$BaTiO_3$:(*x*)$La_{0.835}Na_{0.165}MnO_3$ (*x* = 0, 10, 20, 30, 50, 100 wt%), were prepared using the conventional solid-state reaction method. This work investigates the effect of magnetic inclusion in a nonmagnetic matrix. The synthesized nonmagnetic $BaTiO_3$ majorly crystallized in a ferroelectric tetragonal structure belonging to the *P*4*mm* space group, while the magnetic inclusion $La_{0.835}Na_{0.165}MnO_3$ exhibited phase segregation into a rhombohedral lattice belonging to the $R\bar{3}c$ space group and a monoclinic lattice belonging to a $La_{0.9}MnO_3$-like deficient structure of the *I*12/*a*1 space group. The resulting composites were immiscible solid solutions composed of Ti-deficient $BaTiO_3$ and A-site-deficient $La_{0.835}Na_{0.165}MnO_3$. $BaTiO_3$ and $La_{0.835}Na_{0.165}MnO_3$ were morphologically distinct, with contrasting grain sizes and distributions. Composites showed a loosely bound immiscible grain distribution. The mixing of a nonmagnetic insulator and a ferromagnetic metal/semiconductor endowed the composites with unique optical properties. The band gap was effectively tuned from the ultraviolet to the visible region of the electromagnetic spectra. The composites exhibited a large Urbach energy. $BaTiO_3$ in its non-stoichiometric form was found to be a weak ferromagnet at room temperature and exhibited spin-glass-like frustration at low temperatures. $La_{0.835}Na_{0.165}MnO_3$ showed a double magnetic transition due to structural phase segregation. The composites showed robust ferromagnetism at room temperature, inheriting it from the magnetic component $La_{0.835}Na_{0.165}MnO_3$. The salient ferroelectricity of $BaTiO_3$ disappeared in the composites due to large leakage currents. However, at low bias voltages, a leaky ferroelectric nature with ferromagnetism existed at room temperature for the *x* = 10% specimen, making it a photosensitive, multiferroic, magnetoelectric composite oxide suitable for room-temperature applications.

Received 12th October 2025,
Accepted 6th January 2026

DOI: 10.1039/d5ma01177a

rsc.li/materials-advances

1. Introduction

Multiferroic materials are a class of condensed-matter systems with two or more switchable ferroic ground states, such as ferromagnetic (FM), ferroelectric and (FE) ferroelastic (FEL).[1] Recently, there has been increased attention towards multiferroic materials, especially for magnetoelectric (ME) materials, in which an electric field controls the magnetic polarization and *vice versa*.[2] The escalation in the attempts to obtain such materials is rooted in a developing new area called versatile memory devices due to their unparalleled efficiency while reading and writing of data.[3] The current-driven magnetization switching needs charge mobilization, which comes at the cost of Joule heating, energy dissipation and excessive power consumption. In contrast, the energy dissipation in electric field switching is very low, (reduced by an order) due to charging/discharging process. Ideally, the control of magnetism by the electric field can significantly enhance the non-volatile functionality of memory devices and reduce switching power. In ME materials, the electric field is coupled to magnetization or the magnetic field is coupled to electric polarization. Therefore, they can achieve low-power, high-density data storage with swift electrical writing and magnetic reading. Other than these next-generation memory devices, many other applications exploit ME coupling as their working principle, namely, AC and DC magnetic-field sensors, gyrators for voltage gain, ME transformers, and current sensors. The ME effect can also be employed in microwave devices like resonators, phase shifters and filters.[4]

It is very rare to have a single material that exhibits ME at room temperature (RT). This rarity is arises from the intrinsic

[a] Department of Physics, Manipal Institute of Technology, Manipal Academy of Higher Education, Manipal 576104, Karnataka, India.
E-mail: mamatha.daijna@manipal.edu, mamata.shet@yahoo.com
[b] Institute Néel, University Grenoble Alpes, CNRS, Grenoble INP, PB 38000 Grenoble, France

nature of materials, where the coexistence of FE and FM can vanish when magnetic order is developed and *vice versa*. This lies at the core of the matter where the former requires filled orbitals in atoms, and the latter requires unfilled orbitals.[5] Thus, to enhance the availability of new ME materials, several fabrication alternatives have been explored. This includes the substitution of different magnetic or nonmagnetic ions at an appropriate site in FE and FM materials or the fabrication of a ferromagnetic/ferroelectric superlattices and heterostructures. The disadvantage of superlattices or heterostructures is that they show substrate clamping effect, which has an undesirable effect on ME coupling; nevertheless, they provide a clean single-crystalline structure.[6] A simple way to obtain ME material is to develop a solid solution in the form of bulk or nanostructured composites and multiphase materials. Composites composed of FE and FM constituents, preferably having a similar structure, offer improved phase connectivity between the constituent phases. Furthermore, size reduction can offer a large surface area for interactions, and the core–shell structure can enhance the ME effect through better mechanical coupling between the constituent phases.[7] In such composites (bulk/nano), preferably with FE and FM ground states, ME coupling can arise from the interplay of piezoelectricity and magnetostriction, or from charge-carrier modulation in the ferromagnetic phase *via* the so-called as field effect.[8] Because the preparation of bulk solid-solution composites of two distinct ferroic materials is easy and economical, it is practical to consider a prototype FE material, like barium titanate (BTO), and an FM material, such as colossal magnetoresistance (CMR) manganites or ferro-/ferrimagnetic oxides, as parent composition for composites.

$BaTiO_3$ is an outstanding ferroelectric and piezoelectric material that is widely employed in piezoelectric transducers, high-permittivity capacitors and infrared detectors.[9] BTO is also employed in water splitting and wastewater treatment for degrading the water pollutants, such as dyes, due to its tunable bandgap (E_g) in the ultraviolet (UV) region.[10–13] It exhibits a vivid temperature-dependent crystal structure and correspondingly varying dielectric properties. BTO has a paraelectric cubic structure ($<$393 K) belonging to the $Pm\bar{3}m$ space group (SG). A phase transition occurs below 393 K to a tetragonal lattice (SG: $P4mm$), which is a polar phase responsible for the emergence of FE in BTO. This phase sustains up to 278 K, below which further phase transitions occur to orthorhombic and, at $<$183 K, rhombohedrally distorted structure, both of which are also FE. The abrupt distortion of the crystal lattice at 393 K is responsible for spontaneous polarization, P_s = 18 μC sm^{-2}, which then increases to 26 μC sm^{-2} at RT.[14–17] In fact, the physical quantities such as the large electric polarization, high piezoelectric coefficient and tunable wide band gap make $BaTiO_3$ a truly multifunctional material. However, pure BTO is diamagnetic, and thus it is unattractive for magnetoelectric functionality.[18] There were several attempts to improve the ME effects in BTO, such as the substitution of Ti^{4+} and Ba^{2+} with magnetic ions or the fabrication of FE/FM heterostructures. However, forming composites of BTO with another FM perovskite appears to be a simple and viable option.

Mixed-valent rare-earth manganites (MVMs) are one such oxides that display a robust ferromagnetic metallic (FMM) ground state. Hole or electron doping in these materials induces mixed valency, which is responsible for the FMM behavior. Depending on the percentage of substitution, MVMs display distinct magnetic and electrical ground states,[19–22] and hence they have been exploited in various applications such as magnetic field sensors, temperature sensors, gas sensors, electric field sensors, spin transistors, spin valves, p–n junctions, field-effect devices, capacitors, and energy storage devices.[23] The most intriguingly and vastly studied property of MVMs is magnetoresistance (MR).[24] Manganites have also been explored in their composite forms with other oxides, metals, and polymers for applications in magnetoresistance, magnetocaloric effects and their optical activity. In this context, due to the stable RT FMM state of MVMs, they appear as an appropriate candidate for forming composites with BTO to realise a stable ME material. Both barium titanate and manganites possess perovskite structure, so that maximum compatibility between the constituent phases can be achieved; meanwhile, the starting material and synthesis procedure are easy and economical.[25,26] To narrow down a manganite precursor from a vast array of compositions, one must choose a material with a magnetic transition temperature (T_C) at or above RT and a formation temperature comparable to that of BTO. In a given set, MVMs with a 67 : 33 Mn^{3+} to Mn^{4+} ratio exhibit the maximum possible T_C. Thus, amongst the possible choices, $La_{0.835}Na_{0.165}MnO_3$ (LNMO), with a T_C of 343 K,[27] can be a starting material for composite formation.

Due to the similar structure of BTO and LNMO, and the close ionic radii and valence states of the elements involved in the composites, the formation of stable composite specimens with improved magnetic properties is quite expected.[28] Apart from achieving multiferroicity, nowadays, researchers also focus on how to obtain large MR and magnetocaloric effects (MCEs) at low magnetic fields and at RT for practical applications.[29] MR can arise from intrinsic effects as well as extrinsic effects. Intrinsic effects, being universal and material-independent, offer less freedom for tailoring. However, extrinsic MR is commonly attributable to grain-boundary (GB) effects related to the natural and artificial GB. This extrinsic MR is ascribed to the spin-polarised inter-grain tunnelling of conduction electrons. If a composite is formed in such a way that one of the constituents is an insulator, it might adjust the tunnelling barrier and act as a pinning centre for domain-wall displacement. Thus, a small applied magnetic field is sufficient to align neighbouring ferromagnetic grains to enhance the magnetoresistance.[28,30–33] Another major issue in MCE materials is their narrow range of working temperature (T_{FWHM}) around the T_C. Materials with large entropy changes show sharp phase transition, limiting the T_{FWHM} to few kelvins around the T_C ($<$ 10 K). Composites essentially extend the magnetic transition range through interfacial exchange coupling, strain effects, diffusion and grain-scale inhomogeneity, thus improving T_{CFWHM}. Furthermore, the visible and near-infrared band gap of manganites may tailor the ultraviolet band gap of BTO to enable visible range optical activity, which is an attractive feature for photovoltaic applications (*e.g.*, photoelectrochemical

water splitting) and photocatalysis (dye degradation). Thus, with these motivations, the composites of BTO and LNMO with compositions $(1-x)$BTO:xLNMO in the bulk form were prepared to investigate their structural, optical, magnetic and ferroelectric properties, with the aim of tuning the E_g towards the visible side of the EM spectrum and realizing a ferromagnetic ground state in the composites.

2. Materials and methods

The synthesis of composite materials, consisting of varying percentages of $BaTiO_3$ and $La_{0.835}Na_{0.165}MnO_3$, with compositions denoted as $(1-x)$BTO:xLNMO (where x ranges from 0 to 100%; samples are code as BL0, BL10, BL20, BL30, BL50, and BL100), were achieved through a two-step solid-state reaction process. Precursors such as highly pure (Sigma Aldrich, powders, >99.5% trace metals basis) La_2O_3, Na_2CO_3 and MnO were weighed in a stoichiometric ratio of 0.835 : 0.165 : 1 and ground. Isopropyl alcohol (IPA) was used as the wet medium for grinding. The resulting mixture was dried and then calcined at 800 °C for 12 hours in three cycles. The resulting mixture was pressed into pellets and sintered at 950 °C for 12 hours. Similarly, $BaTiO_3$ was prepared by weighing $BaCO_3$ and TiO_2 in a 1 : 1 ratio and mixing them using the same procedure as for the manganite. The mixture was calcined at 1200 °C for 4 hours in three cycles. The resulting powder was pressed into pellets and sintered at 1300 °C for 4 hours.

The second step involved processing the pellets obtained from the first step into a fine powder. The crushed powders were weighed in stoichiometric proportion, ground using an agate mortar and pestle in a wet medium containing IPA, dried, and then ground a second time with polyvinyl alcohol (PVA) as a binder. The resulting solid solution was pressed into rectangular pellets and sintered at 950 °C for 4 hours.

To investigate the structure of the prepared specimens, XRD patterns were recorded using a Bruker D2 phaser powder X-ray diffractometer (angular accuracy of ±0.02° and minimum step size of 0.005°). Morphology and elemental compositions were traced using a ZEISS Ultra-55 field-emission scanning electron microscope (lateral resolution of 1.0–4.0 nm at 15–0.1 kV, with typical accuracy <1 nm). Elemental composition and chemical states were analyzed using a Trmo scientific K-alpha X-ray photoelectron spectrometer (Al K-alpha source, energy resolution of ~0.5 eV and accuracy of ±0.1–0.2 eV). Optical characters were studied using a PerkinElmer Lambda 950 UV-visible-NIR spectrometer (adjustable resolution of 0.05–5.00 nm and wavelength accuracy ≤±0.08 nm) over the spectral range from 175 nm to 2000 nm. Ferroelectric measurements were carried out using a *P–E* loop tracer (Radiant Technologies, accuracy of ±0.1–0.25% of full scale). Magnetic measurements were carried out using a superconducting quantum interference device (SQUID)-based vibrating sample magnetometer (magnetic field of ±7 T (0.1–0.5% of the set value), a temperature range of 2 K to 400 K (± 0.2–0.5 K) and accuracy over moment of 10^{-8}–10^{-7} emu) with a magnetic field sweep of ±50 kOe over a temperature range of 5–400 K.

3. Results and discussion

3.1 Structure, morphology and electronic structure

After the synthesis of $BaTiO_3$ and $La_{0.835}Na_{0.165}MnO_3$, X-ray diffraction patterns were recorded at RT in the 2θ range of 10° to 90° to examine the structural dynamics of the parent compounds and their composites. The XRD patterns are shown in Fig. 1. Theoretical validations of structure formability and stability are discussed in the SI.

Clearly, BL0 and BL100 exhibit distinct XRD patterns, and the composites show the presence of contributions from both BL0 and BL100 depending on the percentage of substitution. The approximate percentage of constituent phases present in the composites after final sintering was calculated from the intensities of these powder X-ray diffraction (PXRD) patterns. The major reflections corresponding to BL0 and BL100 were considered, and the relation $\text{Phase}\% = \frac{I_{\text{BL0/BL100}}}{I_{\text{BL0}} + I_{\text{BL100}} + I_{\text{impurity}}}$ was used to estimate the percentage of each phase present in the composites.[34] The calculated percentages are shown in Table 2, and they are approximately equal to the mole percentages used during synthesis. $BaTiO_3$ often crystallizes in a tetragonal structure with space group (SG) *P*4*mm* (SG no. 99).[35,36] On the other hand, $La_{0.835}Na_{0.165}MnO_3$ crystalizes in a rhombohedral structure with SG $R\bar{3}c$ (SG no. 167).[37] With this knowledge, to confirm tetragonal and rhombohedral distortions in BL0 and BL100, and to prove the immiscibility of the parent structure in the composites, it is essential to extract the best estimate for Bragg peak intensities (Miller indices and *hkl*) and then to perform structure matching across the whole diffractogram. Therefore, whole powder pattern decomposition (WPPD) was performed using the Le Bail (LB) method to extract the peak intensities.[38,39] The LB method successfully decomposed the whole powder pattern of BL0 under the *P*4*mm* SG, even though there were some unindexed peaks prominently visible at 24°, 28° and 30.6°. On the other hand, there was a complete failure of profile matching in BL100 under the $R\bar{3}c$ space group alone. Ideally, the PXRD pattern of a rhombohedral crystal exhibits twin peaks at the major reflections.[40–43] However, in BL100, there exists a shoulder at the immediate lower 2θ of the major peak (indicated as $ in Fig. 1), which persists even in the composites. This indicates the existence of an overlapping contribution to the diffracted X-ray intensity essentially from another phase. With rigorous investigations, this phase was identified as a monoclinic self-doped $La_{0.90}MnO_3$-like structure with space group *I*12/*a*1 (SG no. 15).[44] The reason behind segregation is the volatility of alkali metal carbonates (one of the precursors) at high temperature (above 850 °C) and their solubility.[45,46] If the reaction temperature is raised to an extent where rare-earth manganites usually form (1300 °C to 1500 °C), the resultant composition will become self-doped or deficient manganite due to the evaporation of Na_2O or other Na-containing vapours.[47–49] Suppose a lower sintering temperature is adopted, the diffusion of constituents during the solid-state reaction is inhibited, leading to inhomogeneity and the formation of mixed phase manganites.[50] There were also unindexed peaks at 31.6° and 36.1°, which were identified as

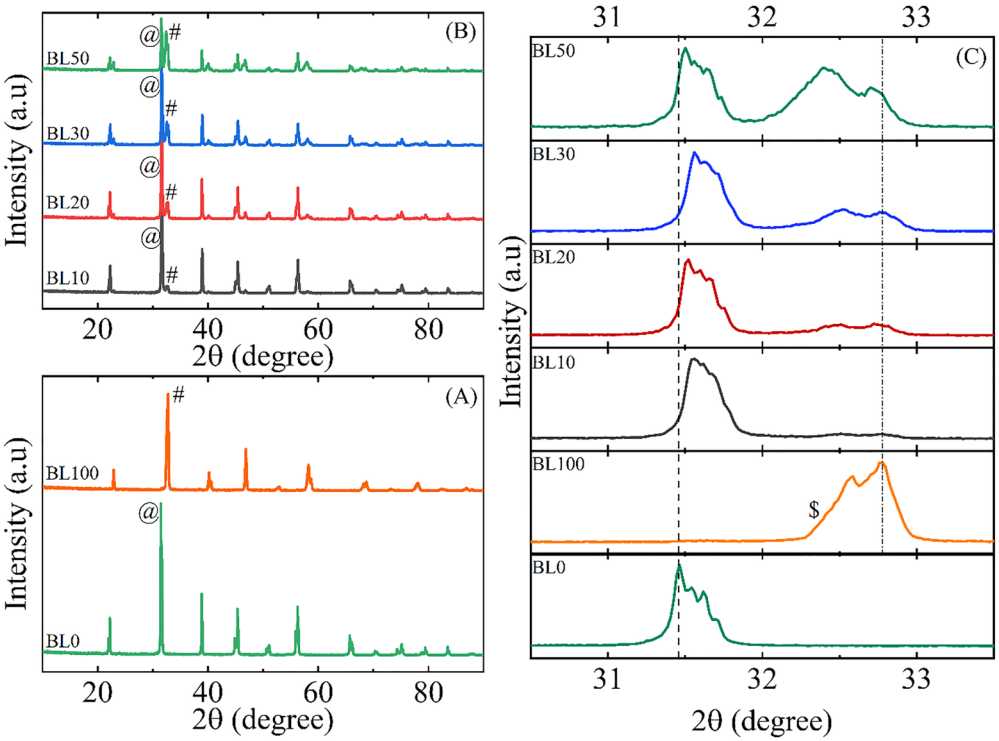

Fig. 1 (A) RT XRD patterns of BL0 and BL100. The @ and # indicate the major reflections of BL0 and BL100, respectively. (B) Stacked RT XRD patterns of the composite samples. (C) Stacked major reflections of the prepared samples, presented to visualize the evolution of each phase in the composites.

bixbyite La_2O_3 with a cubic structure belonging to the $Ia\bar{3}$ SG SG and parasitic Mn_3O_4 formed due to the evaporation of sodium or incomplete reaction of MnO, which crystalizes in a tetragonal structure ($I4_1/amd$ SG), respectively. Once the profile matching is completed, Rietveld refinement was performed for structure matching, considering outputs from the LB method (lattice parameters, zero-point, background and profile parameters). The Rietveld-refined powder XRD patterns are shown Fig. 2. The summary of the refinement is tabulated in Table 1.

The linear nature of the difference curve, the small difference between R_{wp} and R_{exp}, the value of χ^2 close to unity and the small values of R_B are indicators of good agreement between the experimental and calculated data governed by the proposed structural model (the meaning and implications of R factors are given in the SI). Thus, it is confirmed that the specimen BL0 belongs to a polar tetragonal structure, and BL100 has nonpolar rhombohedral structure. The synthesis of single-phase $BaTiO_3$ is a challenging due to the complex phase diagram of BaO/$BaCO_3$ and TiO_2 precursors, depending on the Ba/Ti ratio ($g^\star$), temperature (T) and oxygen partial pressure (PO_2). For a fixed T and PO_2, it was found that if $g^\star$ is close to 1, then single-phase $BaTiO_3$ with systematically tunable ferroelectric properties can be realised. However, if $g^\star$ is far away from unity, the solubility of either of the precursors terminates, and defects (partial Schottky defects and oxygen vacancy defects in the $BaTiO_3$ solid solution) are established in the Ba, Ti and O sublattices. The defects promote the perturbation of equilibrium, and Ti-rich or Ba-rich phases are formed alongside $BaTiO_3$. On the Ba-rich side ($g^\star > 1$), Ba_2TiO_4 and $Ba_{1.054}Ti_{0.946}O_{2.946}$ are the most favourable secondary phases, depending on $g^\star$, T and whether they are quenched or slow cooled to ambient temperature. Similarly, on the Ti-rich side ($g^\star > 1$), the secondary phases are $BaTi_2O_5$ and $Ba_6Ti_{17}O_{40}$. Furthermore, the thermodynamic stability of $Ba_{1.054}Ti_{0.946}O_{2.946}$ and $BaTi_2O_5$ is limited to relatively lower temperatures (1150 °C and 1120 °C–1250 °C, respectively). Once these temperatures are crossed, these compositions undergo peritectoid reactions to form $BaTiO_3$ and $Ba_2TiO_4/Ba_6Ti_{17}O_{40}$. A serious consideration on secondary phases in ferroelectric and ferroelastic materials is required, as the surface nucleation of these secondary phases on the primary $BaTiO_3$ phase can create stresses and affect ferroelectric properties due to different thermal coefficients of expansion between the two phases.[51,52] Therefore, if the temperature is fixed at 1300 °C–1320 °C (as in the present case, sintering was carried out at 1300 °C) and the PO_2 is normal, the possible secondary phases that can be identified in the present investigation are Ba_2TiO_4, $BaTi_4O_9$[53] and $BaCO_3$[52] (the phase fraction of each secondary phase is $<1.7\%$). The short soaking time and slow cooling of BL0 to ambient temperature contributed to the precipitation of secondary phases.[52] Though these secondary phases may have obvious effects on physical and optical properties, the major phase fraction (98%) is essentially polar $BaTiO_3$ with a tetragonal lattice.

The phase equilibrium in the binary La_2O_3–Mn-based oxide system is well established, and it has been found that the major ternary phase that can form in the perovskite phase is $LaMnO_3$ solid solution.[54] Any other impurity phases are formable only at very high temperature (1650 K), under a reducing atmosphere,

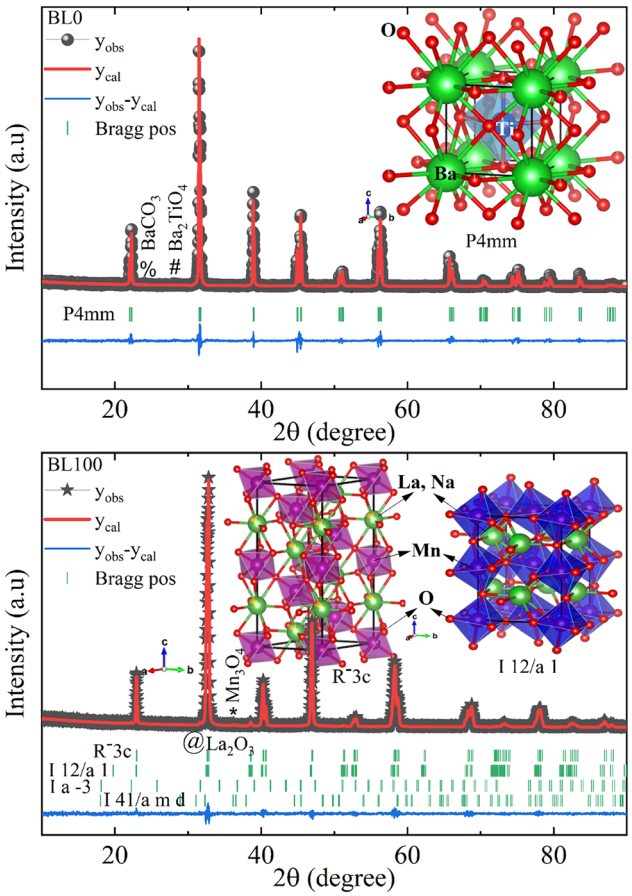

Fig. 2 Rietveld-refined powder XRD patterns of BL0 and BL100. Symbols (bubbles and asterisks) represent the observed data (y_{obs}), the overlaid solid curve corresponds to the calculated profile (y_{cal}), the vertical bars indicate the Bragg peak positions (Bragg pos) and the nearly horizontal line at the bottom represents the difference curve (y_{obs}–y_{cal}). The respective SG are marked on the left of the Bragg positions.

or at pressures greater than 30 kbar. However, phase segregation in BL100 arises from three main factors: (i) thermal stability and solubility of one of the precursors at 950 °C (Na_2CO_3), (ii) limited solid-state diffusion at relatively low sintering temperatures, and (iii) incomplete oxidation of the MnO precursor. The successful substitution of Na^+ for La^{3+} depends on the solubility of Na^+ in the host matrix and compensation for Na^+ volatilization at high T. Monovalent cations have a narrow solid solubility range in rare-earth manganites, typically up to about $x < 0.15$–0.2.[55–57] Beyond this value of x, there occurs the precipitation of secondary phases such as Mn_3O_4 or corresponding metallic phases, as observed in the case of Na^+ and Ag^+ substitution.[58,59] Furthermore, even if the concentration of monovalents is restricted below the critical concentration ($x < 0.15$), elevated soaking temperatures and prolonged dwell times may cause evaporation of monovalents. To avoid such evaporation, either flux-assisted synthesis, addition of excess metal carbonates and microwave-assisted synthesis or chemical synthesis routes are employed.[60–63] In the present synthesis, 5% excess Na_2CO_3 was added to compensate for evaporation. The other precursor that needs attention at this point is MnO. Usually, the preferred precursor for the solid-state synthesis of manganites is MnO_2, as it can be easily reduced to form Mn^{3+} cat the B-site of the perovskite or a mixed valence state of Mn^{3+}/Mn^{4+} at low temperatures. In contrast, MnO, having Mn^{2+}, must be oxidized to achieve such charge states in the perovskite structure. Finally, the calcination temperature adopted in the present study was 800 °C. Considering all these parameters, the existence of secondary phases, majorly the $La_{0.9}MnO_3$-like phase and small traces of La_2O_3 and Mn_3O_4, is attributable to the lack of diffusion and can be understood based on bulk diffusion-controlled kinetics at the immediate phase boundaries of La_2O_3/Na_2CO_3 and MnO. It is established that the actual formation of lanthanum manganite takes place at the La_2O_3/$LaMnO_3$ phase boundary. O and Mn ions diffuse from the MnO/$LaMnO_3$ phase boundary and annihilate with the corresponding vacancies at the La_2O_3/$LaMnO_3$ interface. O_2(gas) also takes part in the reaction, as in MnO, Mn is present in the 2+ oxidation state. O_2 transport takes place preferably *via* pores along the La_2O_3/product interface. At low sintering temperatures, it is seen that in the solid-state diffusion of ions, La^{3+} is quite slower (at least one orders smaller) species compared Mn^{3+}/Mn^{4+}, and diffusion of Na^+ is quite restricted due to charge-compensation mechanisms with O. Apart from the ionic transport of Mn^{3+} and/or Mn^{4+}, there is ambipolar diffusion of Mn–O pairs due to comparable activation energies for Mn^{3+} and O^{2-}, which are again sluggish species in solid-state diffusion. Considering all

Table 1 Summary of Rietveld refinement results for BL0 and BL100

	Sample code				
P.Q	BL0	BL100			
Space group	*P4mm*	*R*$\bar{3}$*c*	*I*12/*a*1	*Ia*$\bar{3}$	*I*4$_1$/*amd*
$a = b$ (Å)	3.99 ± 0.003	5.48 ± 0.009	7.77 ± 0.001	9.789	5.75 ± 0.007
b (Å)	3.99 ± 0.003	5.48 ± 0.009	5.50 ± 0.005		5.75 ± 0.007
c (Å)	4.03 ± 0.004	13.32 ± 0.001	5.46 ± 0.009		9.49 ± 0.004
V (Å^3)	64.30	347.62 ± 0.003	233.93 ± 0.006	937.96 ± 0.009	314.60 ± 0.003
Phase fraction (%)	100	63.52	35.63	0.44	0.41
ρ_{est} (g cm^{-3})	6.02 ± 0.002	6.33	6.59 ± 0.003	9.22 ± 0.009	3.81 ± 0.008
R_{wp}	16.3	12.5	12.5	12.5	12.5
R_{exp}	11.68	11.62	11.62	11.62	11.62
χ^2	1.95	1.16	1.16	1.16	1.16
R_B	4.60	2.65	3.88	54.7	68.6

these characteristics of diffusion kinetics and their dependence on annealing temperature and PO_2, Marian Palcut *et al.*[64] have inferred that the compositional limit on the La-deficient side of $LaMnO_3$ formation is $La_{0.89\pm0.01}MnO_{3\pm\Delta}$. Once formed, it is significantly stable with a change of temperature and oxygen partial pressure. A similar finding has been reported for $NdMnO_3$, where a stable Nd-deficient composition, $Nd_{0.88}MnO_{2.92}$, was found. The Nd_2O_3 and Mn_3O_4 phases have precipitated beyond the solubility limit.[65] The final stoichiometry of lanthanum manganite depends on its thermal history, and it is of paramount importance in defect chemistry of these materials. This, in fact, is true as a sample prepared elsewhere with similar initial conditions as ours, but with MnO_2 as the precursor, exhibited (though not identified by the author) similar structural distortions in XRD patterns (a shoulder on the main peak), consistent with $La_{0.89\pm0.01}MnO_{3\pm\Delta}$, even after post-annealing treatment at 1150 °C for 72 h.[66] In the present investigation, it is asserted that the low calcination temperature contributed to the generation of secondary phase, perhaps similar in structure to $La_{0.9}MnO_3$, due to diffusion inhibition during the solid-state reaction. The activation energy at the given annealing temperature (800 °C) was sufficiently high to prevent diffusion of the constituent ions and ambipolar Mn–O pairs, which led to phase segregation. Furthermore, as the samples were air-annealed, the supply of oxygen was insufficient to completely oxidize MnO. As a result, the La_2O_3/Na_2CO_3–MnO system could not attain equilibrium, and based on the local availability of the mixture, a phase-segregated $La_{0.835}Na_{0.165}MnO_3$:-$La_{0.9}MnO_3$ perovskite composite was formed. Furthermore, based on the thermal history of the solid-solution, once the $La_{0.9}MnO_3$ phase is formed, it continues to exist even after repeated high-temperature annealing, thus asserting the cause for the existence of the monoclinic $La_{0.9}MnO_3$-like phase in BL100 and the composites.

Fig. 3 shows Rietveld-refined PXRD patterns of all the composites, and Table 2 shows the consolidation of the output of the refinement. The proximity of R factors R_{wp} and R_{exp} indicates the goodness of fit. Furthermore, the R_B is expected to be a small number, and χ^2 is close to unity. The negligible difference between y_{abs} and y_{cal} is a visual marker of goodness of fit. The refinement thus confirms the expected immiscible two-phase characteristic of the composite. The phase fractions obtained from the refinement are close to the nominal values (Table 2). The disagreement between phase fractions obtained from the intensity ratio $I_{(B/L)}/T_T$ and those from Rietveld refinement is because of the non-included intensity of impurity phases like $La_{0.9}MnO_3$, La_2O_3 and Mn_3O_4 during the calculation. Furthermore, even within the Rietveld-refined phase fractions, there are deviations in phase fractions at higher concentrations, such as in BL30 and BL50. This led to the identification of a new phase in the composites alongside Ba_2TiO_4 and Mn_3O_4 (marked as & and # in Fig. 3). Careful examination of the PXRD patterns for composites (BL30 and BL50) reveals a new peak at $2\theta = 26.3^\circ$, which belongs to the [103] reflection of a hexagonal structure with a $P6_3/mmc$ SG. This very minor phase (phase fraction < 3%) belongs to moderately substituted $BaTi_{1-x}Mn_xO_3$[67,68] or an oxygen-deficient $BaTiO_3$ structure.[69,70] Mn cations can readily replace Ti in $BaTiO_3$ due to close proximity in their ionic radius (Ti^{4+}: 0.605 Å. Mn^{3+}: 0.645 Å and Mn^{4+}: 0.53 Å). At the higher reaction temperature of 950 °C, the diffusion of cations, Mn and Ti, can replace each

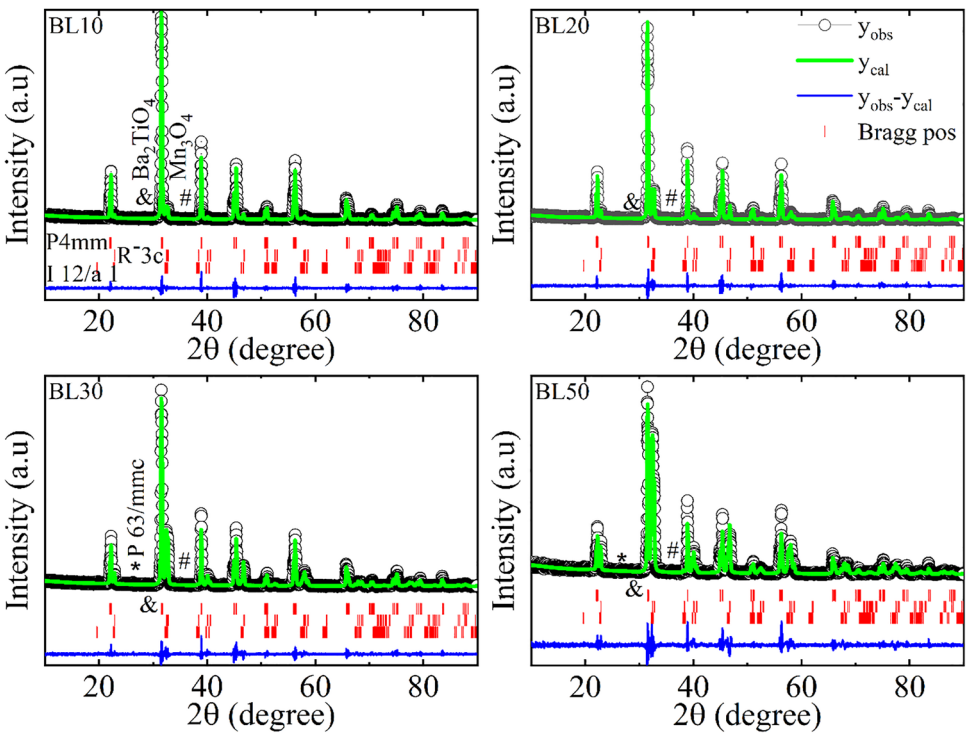

Fig. 3 Rietveld-refined powder XRD patterns of BL10, BL20, BL30 and BL50. The respective SG are indicated to the left of the Bragg positions.

Table 2 Summary of Rietveld refinement results for BL10, BL20, BL30 and BL100

	SC											
PQ	BL10			BL20			BL30			BL50		
Space group	*P*4*mm*	*R*$\bar{3}$*c*	*I*12/*a*1	*P*4*mm*	*R*$\bar{3}$*c*	*I*12/*a*1	*P*4*mm*	*R*$\bar{3}$*c*	*I*12/*a*1	*P*4*mm*	*R*$\bar{3}$*c*	*I*12/*a*1
$a = b$ (Å)	3.99 ± 0.005	5.51 ± 0.004	7.85 ± 0.002	3.99 ± 0.004	5.51 ± 0.001	7.83 ± 0.005	3.99 ± 0.005	5.51 ± 0.005	7.84 ± 0.008	3.99 ± 0.004	5.52 ± 0.001	7.85
b (Å)	3.99 ± 0.005	5.51 ± 0.004	5.53 ± 0.002	3.99 ± 0.004	5.51 ± 0.001	5.52 ± 0.005	3.99 ± 0.005	5.51 ± 0.005	5.53 ± 0.005	3.99 ± 0.004	5.52 ± 0.001	5.53 ± 0.008
c (Å)	4.03 ± 0.001	13.34 ± 0.001	5.48 ± 0.004	4.03 ± 0.001	13.33 ± 0.004	5.47 ± 0.008	4.03 ± 0.001	13.33 ± 0.009	5.48 ± 0.009	4.03 ± 0.001	13.33 ± 0.002	5.50
V (Å^3)	64.34 ± 0.002	351.26 ± 0.003	238.20 ± 0.007	64.31 ± 0.002	350.66 ± 0.008	237.11 ± 0.004	64.33 ± 0.004	351.40 ± 0.007	238.43 ± 0.009	64.28 ± 0.007	351.91 ± 0.003	239.06 ± 0.009
Phase fraction (%) RR	91.10	6.26	2.64	78.80	13.52	7.68	66.80	22.30	10.90	41.63	31.91	26.46
Phase fraction (%) $I_{(B/L)}/I_T$	94	6.5		86	14		77	23		57	43	
ρ_{est} (g cm^{-3})	6.01 ± 0.009	6.31 ± 0.002	7.18 ± 0.005	6.02 ± 0.002	6.32 ± 0.003	7.21 ± 0.008	6.01 ± 0.009	6.30 ± 0.009	7.17 ± 0.008	6.02 ± 0.004	6.30	7.15 ± 0.009
R_{wp}	15.2	15.2	15.2	15.6	15.6	15.6	15.2	15.2	15.2	16.6	16.6	16.6
R_{exp}	11.54	11.54	11.54	11.46	11.46	11.46	11.72	11.72	11.72	11.65	11.65	11.65
χ^2	1.73	1.73	1.73	1.86	1.86	1.86	1.68	1.68	1.68	2.02	2.02	2.02
R_B	10.9	15.0	19.9	5.38	6.74	11.2	3.33	6.51	9.61	6.14	8.52	9.64

Note: SC stands for sample code, PQ stands for physical quantity, RR stands for Rietveld refinement, $I_{(B/L)}/I_T$ is the intensity ratio of titanate or manganite to the total intensity.

other, particularly at a surface-terminated regions of the structure.

To discuss the major phases of the composite, the tetragonal $BaTiO_3$ continues to persist with the attributes of the parent BL0. In tetragonally distorted $BaTiO_3$ the c/a ratio defines the extent of tetragonality. The first reported single crystal of $BaTiO_3$[35,71] had a c/a ratio of 1.0101 ± 0.002. In the present investigation, across the entire series, the c/a ratio is found to be 1.01 ± 0.009. This indicates that lattice expansion or deviation in tetragonality is negligible. However, the c/a ratio is found to increase from BL10 to BL100 in the rhombohedral phase. The crystal volume is found to sharply increase towards BL10 from BL100 in both rhombohedral and monoclinic phases. This finding is slightly unusual, considering no further substitution of foreign atoms during composite formation. It is observed, and has been already established, that at reduced PO_2 and low sintering temperatures, the product phase is La-deficient, and vacancies on both La and O sublattices are dominant. If so, the vacant sites that are available for Mn^{3+} diffusion are most likely the La vacancies and become one of the possible migration paths. Furthermore, the average valence of Mn decreases with decreasing PO_2.[64] Bond valence sum calculation for the monoclinic phase indicate that the average valency of the Mn site is less than 3. This indicates that there is a significant population of Mn^{2+} along with Mn^{3+} and Mn^{4+}, diffusing through the vacancies. During such diffusion, there is a high likelihood of Mn antisite defects to occur on the La sublattice. If one considers ionic size, the presence of Mn on the La site is favoured for a lower valence of manganese (Mn^{2+}), as ionic size increases with decreasing valence (Mn^{2+}: 1.13 Å). Furthermore, in a study by Hundley *et al.*[72] a charge disproportionation model was proposed for deficient manganites, according to which it is stated that in octahedrally coordinated systems, the Mn^{2+}–Mn^{4+} pair is found to be a more stable pair than Mn^{3+}–Mn^{3+}. Consequently, a portion of the manganese ions form Mn_3O_4 as a secondary phase, and the other portion occupies the A-site as Mn^{2+} along with La^{3+} and alkali/alkaline-earth metal ions. In this context of deficiency, an unusual behaviour of heavily self-doped $La_{1-x}MnO_3$ was identified by Orgiani *et al.* The heavily deficient composition, namely $La_{0.66}MnO_{3-\Delta}$, grown as a film on a $SrTiO_3$ substrate, showed full generation of Mn^{4+}. Surprisingly, this composition showed the high metallicity in place of an antiferromagnetic insulating ground state. The study clearly established that this unusual behaviour was a consequence of a multiple double-exchange mechanism mediated by Mn^{2+} present at the A-site of the crystal lattice.[73] It has already discussed that the occurrence of Mn^{2+} at the A-site is promoted by cationic and anionic vacancies at the A-site. Though an increase in unit cell volume cannot be explained on the basis of the existence of Mn^{2+} at the A-site, the mere origin of it (A-site cationic and anionic vacancies) explains the observation. The increase in cell parameters and unit cell volume from BL100 to BL10 is related to the decreasing concentration of oxygen due to the formation of anionic vacancies and the increase in radius of La and Na sites due to vacancies. The only way to compensate for the oxygen vacancies is through a reduction in the average valence of manganese ions. This is why some of Mn^{4+} are reduced to Mn^{3+}, and Mn^{3+} to Mn^{2+}. This progressive increase in ionic radius increases the average ionic radius and, in turn, the unit cell volume. Moreover, anion vacancies at oxygen sites reduce the electrostatic bonding forces, which also leads to an increase in unit cell volume. Furthermore, it is observed that cationic vacancies have a higher ionic radius than their corresponding cations. Systems with alkali/alkaline-earth metal deficiencies always show an increase in volume compared to their parent compositions.[47,74,75] Thus, it is believed that the presence of Mn antisite defects (Mn^{2+}) on the La^{3+} sublattice, along with A-site cationic vacancies and anionic vacancies, is responsible

for the observed increase in the crystal volume of the major manganite phase. To validate these assertions, detailed studies on the surface morphology, elemental composition and electronic structure were carried out by analysing FESEM micrographs, energy-dispersive elemental spectra and X-ray photoelectron spectra.

Fig. 4 shows FESEM micrographs of all the specimens at the same magnification. Apparently, there is a clear visual distinction between the grain size of BL0 and BL100, as well as their porosity. BL0 shows minimal closed porosity, whereas BL100 shows vivid open porosity. Grain sizes were estimated using ImageJ software, and the corresponding distributions are shown in Fig. 4. The grain sizes follow a lognormal distribution, with mean grain sizes of 4.34 μm^2 and 0.47 μm^2 for BL0 and BL100, respectively. Porosity exhibits the opposite trend, which is 1.53% of the given area for BL0 and 10.28% of the given area for BL100. Interestingly, a wide spread of grain size distribution is observed for BL100, whereas BL0 has very similar grain sizes. The lognormality has its origin (SI) in dwell time, and based on this time, various parameters such as the rate of change of product volume and the drift and diffusion of constituents will be decided. Suppose the dwell time is fixed, ion mobility, grain boundary energy, and overall grain growth are mainly decided by the soaking temperature. In other words, the rate constant for solid-state diffusion kinetics is temperature-dependent and follows an Arrhenius-type relationship, given by $K = K_0 \exp\left(\frac{-Q}{RT}\right)$, where k_0 is a constant, Q is the activation energy for grain boundary migration, R is the universal gas constant and T is the temperature. Furthermore, in the context of diffusion, the ion diffusion coefficient, which is a function of temperature, shows Arrhenius-type behaviour, and it can be expressed as $\eta = \eta_0 \exp\left(-\frac{\beta}{RT}\right)$, where η_0, R and β are constants and T is the sintering temperature.[76] Thus, knowing the dynamics of grain growth, it can be concluded that the high sintering temperature and low activation energy in BL0 enable steady grain growth and lead to homogeneous distribution of large grains. In contrast, for BL100, the low sintering temperature and high activation energy hinder steady grain growth and favor the nucleation of smaller grains. Here, the mobility and activation energy of the constituents are not sufficient to achieve sufficient grain boundary migration and volume expansion. As a result, BL100 shows evident open porosity with a wide distribution of small grains. The composites show broken BL0 particles surrounded by BL100 particles. The major cause of this is the size of the initial constituents. The very dissimilar size of BL0 and BL100 and low sintering temperature seem to be insufficient to achieve uniform connectivity between the two dissimilar particles.

Fig. 5 shows the area analysis and point analysis performed using EDS for the identification of elemental composition. Panels A and B correspond to BL0 and BL100, respectively, and stand as testimony of the expected elemental compositions: Ba, Ti, and O (a) for BL0, and La, Na, Mn and O (b) for BL100. Apparently, in the 50 : 50 composite, point analyses at two different locations show Ba, Ti, and O (c) and La, Na, Mn, and O (d). This precisely verifies the immiscibility of the two phases and their independent existence within the composites. Stoichiometric calculations demand atomic percentage of 20 : 20 : 60 for $BaTiO_3$ to be an ABO_3 perovskite, whereas in $La_{0.835}Na_{0.165}MnO_3$, it is 16.7 : 3.3 : 20 : 60. The atomic percentages obtained from the EDS spectra of BL0 are 19.9 : 18.0 : 62.1 (excluding carbon concentration). Though the Ba concentration is close to the nominal one, the Ti concentration shows a deficiency. This is typical for Ba-excess solid solutions in $BaTiO_3$. As the solubility limit of Ba-excess is lower than that of Ti-excess in $BaTiO_3$ phase formation, the evolution of secondary phases such as Ba_2TiO_4 alongside unreacted or atmosphere-adsorbed $BaCO_3$, is inevitable. The elemental composition of BL100 is deviates from the nominal one (7.5 : 1.0 : 6.6 : 85), which states that there is a large surface termination of the perovskite structure with oxygen-rich impurities.

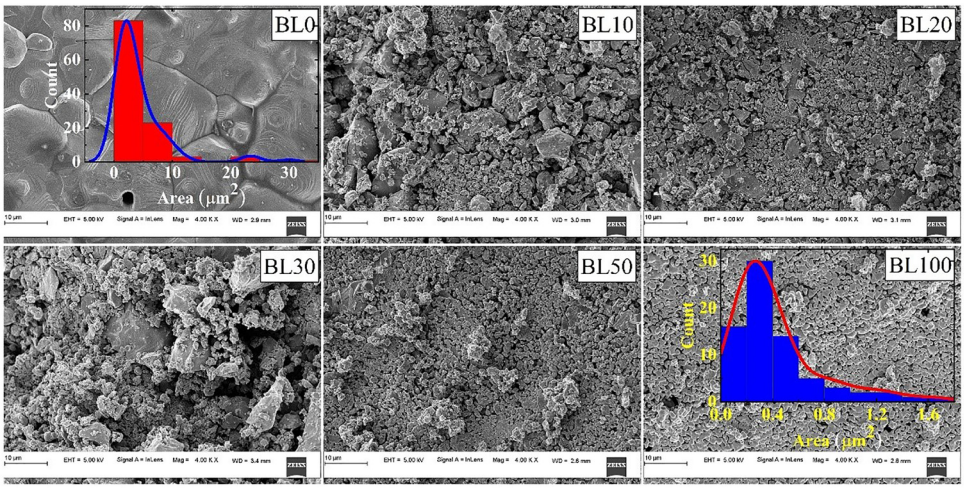

Fig. 4 FESEM micrographs of (1 − x)BTO:x(LNMO), x = 0, 10, 20, 30, 50 and 100, recorded at 4.00k× magnification. The histograms show the grain size distribution of BL0 and BL100 under lognormal distribution. The columns represent counts per scale; the overlaid curve is the kernel-smoothed representation of the respective distribution.

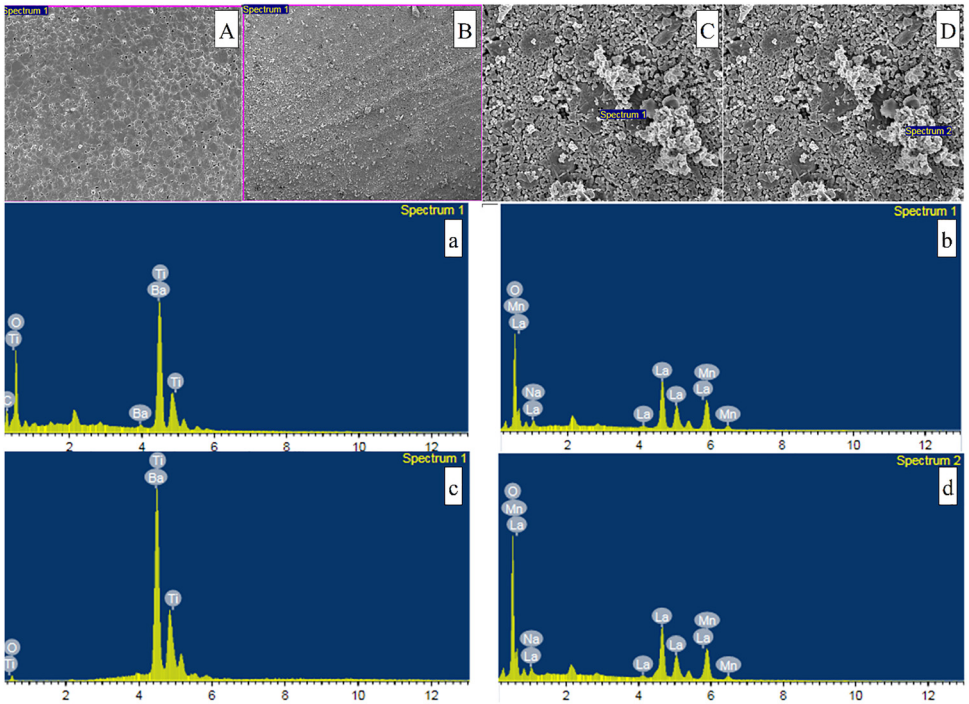

Fig. 5 EDS spectra obtained from area analysis and point analysis. (A) and (B) are area analysis of BL0 and BL100, respectively. (C) and (D) are point analysis on BL50, (C) showing BL0 grain in BL50 specimen and (D) showing clusters of BL100 grains. (a)–(d) are corresponding EDS spectra, showing the binding energy map of elements present in the analysis.

Fig. 6 shows the XPS survey spectra of BL0 and BL100, chosen for surface analysis based on structural implications (mixed valence in $BaTiO_3$ and $La_{0.835}Na_{0.165}MnO_3$, as well as cationic and anionic vacancies). It should be noted that the chemical state and valence states of elements in the bulk of the composites are expected to be similar to those of their parent compounds and largely remain unaltered due to the low sintering temperature employed during their synthesis. Considering the C 1s core line as a reference, the spectrum of BL0 was corrected for its binding energy (B.E) to account for the shift due to charging (2 eV); meanwhile, there was no charging observed in BL100. All the features observed in the survey spectra are testimony of desired elements. Strong signals at 779.8 eV, 459.5 eV, 833.4 eV, 1071 eV, 641.6 eV, 528.6 eV and 528.9 eV correspond to Ba 3d, Ti 2p, La 3d, Na 1s, Mn 2p and O 1s core-level binding energies, respectively.[77] Additionally, reference signals are observed at 286.6 eV and 284.4 eV for BL0 and BL100 eV, respectively, corresponding to adventitious carbon. This is a ubiquitous hydrocarbon contamination that accumulates on the surface of the specimen during handling and storage. However, favourably, it plays a role of reference for charging correction to all other elements during the scan. Having known the B.E positions and separations using first- and second-derivative methods, deconvolution was carried out using CasaXPS peak fitting software to assign each of these features and to investigate different types of chemical bonding and valence states involved in the structure formation. The resulting B.E positions, assignments, and spin–orbit splitting (SOS) values are tabulated in Table 3.

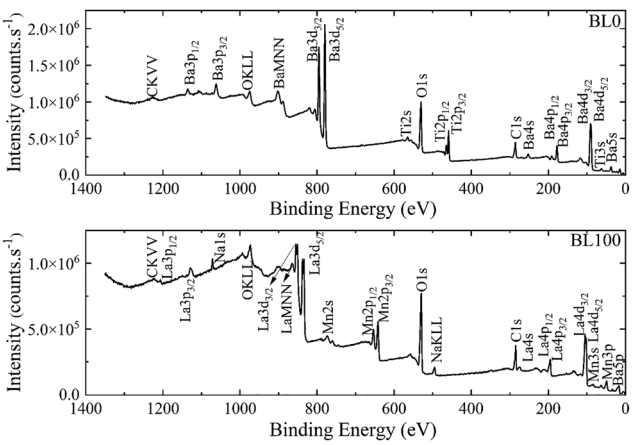

Fig. 6 X-ray photoelectron survey spectra of BL0 and BL100, recorded using an Al K-α source.

The deconvolution of the core-level spectra for $BaTiO_3$ and $La_{0.835}Na_{0.165}MnO_3$, along with the respective C 1s core spectra, is shown in Fig. 7. The Ba 3d core spectrum shows the characteristic doublet structure, with each peak further resolved into two distinct components (Ba_I and Ba_{II}). The B.E separation of Ba_I and Ba_{II} with respect to their higher-energy doublet is 15.32 eV, and the area ratios are 1.43 and 1.51, respectively. This confirms that the doublet arises from spin–orbit splitting of Ba 3d electrons. The coupling splits the 3d subshell into two levels with different total angular momentum

Table 3 Binding energy positions, binding energy separations, FWHM of core lines, area ratios and assignments for each component of the core-level spectra obtained from deconvolution

Sample code	Element code	Core level	Peak name	Species	Peak position	BE separation	FWHM	Area	% Area	Area ratio
BL0	Ba_I	3d	$3d_{5/2}$	Ba^{2+}	779.64	15.32	1.43	501 807.8	27.04	1.43
			$3d_{3/2}$		794.96		1.44	349 284.8	18.82	
	Ba_{II}	3d	$3d_{5/2}$	Ba^{2+}	781.13	15.32	1.75	533 530.5	28.75	1.51
			$3d_{3/2}$		796.45		1.69	352 405.0	18.99	
	Ti^{3+}	2p	$3d_{3/2}$	Ti^{3+}	458.00		1.75	10 947.9	4.55	
	Ti^{4+}	2p	$3d_{3/2}$	Ti^{4+}	459.47	5.77	1.12	152 711.4	63.33	1.99
			$3d_{1/2}$		465.24		2.03	76 718/93	30.64	
	O_I	1s	1s	O^{2-}	528.59	1.99, 4.46	1.34	233 133.2	57.23	
	O_{II}			Ov	530.58		2.14	165 024.7	40.51	
	O_{III}			OH	533.05		2.13	9238.2	2.27	
	C_I	1s	1s	C–C	284.61	1.63, 3.51	1.61	81 659.3	72.58	
	C_{II}			C–O	286.24		1.01	6227.4	5.54	
	C_{III}			O–C═O	288.12		2.19	24 620.7	21.88	
BL100	La_I	3d	$3d_{5/2}$	cf^0	833.30	4.5	1.52	105 933.9	17.80	
	La_{II}			cf^1L AB	834.60	3.2	3.45	266 887.6	44.84	
	La_{III}			cf^1L B	837.80		2.40	222 393.5	37.36	
	Na_I	1s	1s		1070.63		1.27	19 790.7	40.45	
	Na_{II}				1071.58		1.53	21 022.1	50.64	
	Na_{III}				1072.89		1.60	3696.6	8.91	
	Mn_{II}	2p	$2p_{3/2}$	Mn^{2+}	640.81		2.00	25 150.2	14.11	
	Mn_{III}			Mn^{3+}	641.06		3.07	89 259.7	50.08	
	Mn_{IV}			Mn^{4+}	642.43		2.40	43 423.7	24.36	
	$Mn^{3+}mp$			Mn^{3+}	644.17		1.97	14 495.9	8.13	
	$Mn^{2+}mp$			Mn^{2+}	645.73		2.07	5902.90	3.31	
	O_I	1s	1s	O^{2-}	528.85	0.98, 2.04, 3.96	1.14	163 556.5	43.09	
	O_{II}			O^{2-}	529.83		1.10	25 725.5	6.78	
	O_{III}			Ov	530.89		2.00	120 386.7	31.72	
	O_{IV}			OH	532.81		2.80	69 910.1	18.42	
	C_I	1s	1s	C–C	284.45	1.28, 3.55	1.31	46 132.1	55.65	
	C_{II}			C–O	285.73		2.09	17 433.2	21.03	
	C_{III}			O–C═O	288.00		2.51	19 327.0	23.32	

$\left(j = \frac{3}{2} \text{ and } \frac{5}{2}\right)$. The lower-energy $3d_{5/2}$ components are located at 779.64 eV and 781.13 eV, and the higher-energy $3d_{3/2}$ components are located at 794.96 eV and 796.45 eV. These B.E positions (particularly for Ba_I) are negatively shifted relative to metallic Ba, which is typical of Ba^{2+} in a perovskite/oxide lattice.[39] Broad humps 10–11 eV above the $3d_{5/2}$ and $3d_{3/2}$ core lines correspond to inelastic loss features. The point of interest in the Ba 3d core spectrum is the existence of two different components with similar FWHMs within a single core line ($3d_{5/2}$ and $3d_{3/2}$), which indicates that Ba exists in two different chemical environments but with the same oxidation state. No doubt that Ba_I is in a perovskite environment, but there are several attributions to the Ba_{II} component, such as $BaCO_3$ and $Ba(OH)_2$. This speculation is based on the B.E positions at 781.13 eV and 796.45 eV for the Ba_{II} component. However, the C 1s (panel 8) and O 1s (panel 3) core-level spectra, which sensitively reflect the surface contamination, do not show any such signature to confirm the existence of $BaCO_3$ and $Ba(OH)_2$. The C 1s photoelectron spectrum of BL0 exhibits a prominent peak at 284.6 eV, belonging to adventitious carbon of the type C–C/C_xH_y. Additional components at 286.24 eV and 288.12 eV, whose intensity is significantly lower than that of adventitious carbon, are attributable to other carbonaceous species, perhaps C–O and O–C═O. It should be noted that the B.E position in the C 1s core line spectra for carbonates (*e.g.*, $BaCO_3$) exists in the range 289–290.4 eV; however, no such component is observed in the in the C 1s core spectrum of BL0. Further observation of carbonate in XPS spectra is difficult because it forms discrete particles rather than a continuous surface layer. The O 1s core spectrum is composed of three components: O_I, O_{II} and O_{III} situated at 528.59 eV, 530.58 eV and 533.05 eV, respectively. The first component, O_I, belongs to lattice oxygen in the $BaTiO_3$ perovskite framework. The second component, O_{II}, belongs to oxygen vacancies, and the third component, O_{III}, belongs to adsorbed oxygen species such as H_2O. However, the presence of $Ba(OH)_2$ cannot be confirmed, as it is highly reactive with CO_2 and forms $BaCO_3$ immediately. There are also studies that attribute Ba_{II} to a near-surface phase related to relaxation of residual strain. However, more evidential and physically significant attributions are as follows: (1) Ba_{II} is not a result of surface contamination but of perovskite origin, attributable to Ba^{2+} in the $BaTiO_3$ lattice having domains with their *c*-axis aligned along the surface normal, whereas Ba_I corresponds to Ba^{2+} in the $BaTiO_3$ lattice having domains with their *a*-axis aligned along the surface normal.[78] (2) Ba^{2+} in Ba_2O, which is a result of the reduction of BaO to Ba_2O at high temperatures due to the displacement of O atoms that are trapped in the vicinity of BaO.[79] In both spectra, common attributes are the O_{II} band, corresponding to oxygen vacancies, and the appearance of a minor Ti^{3+} band in the Ti 2p core spectra as a consequence of partial reduction of Ti^{4+} to Ti^{3+} to compensate for charge

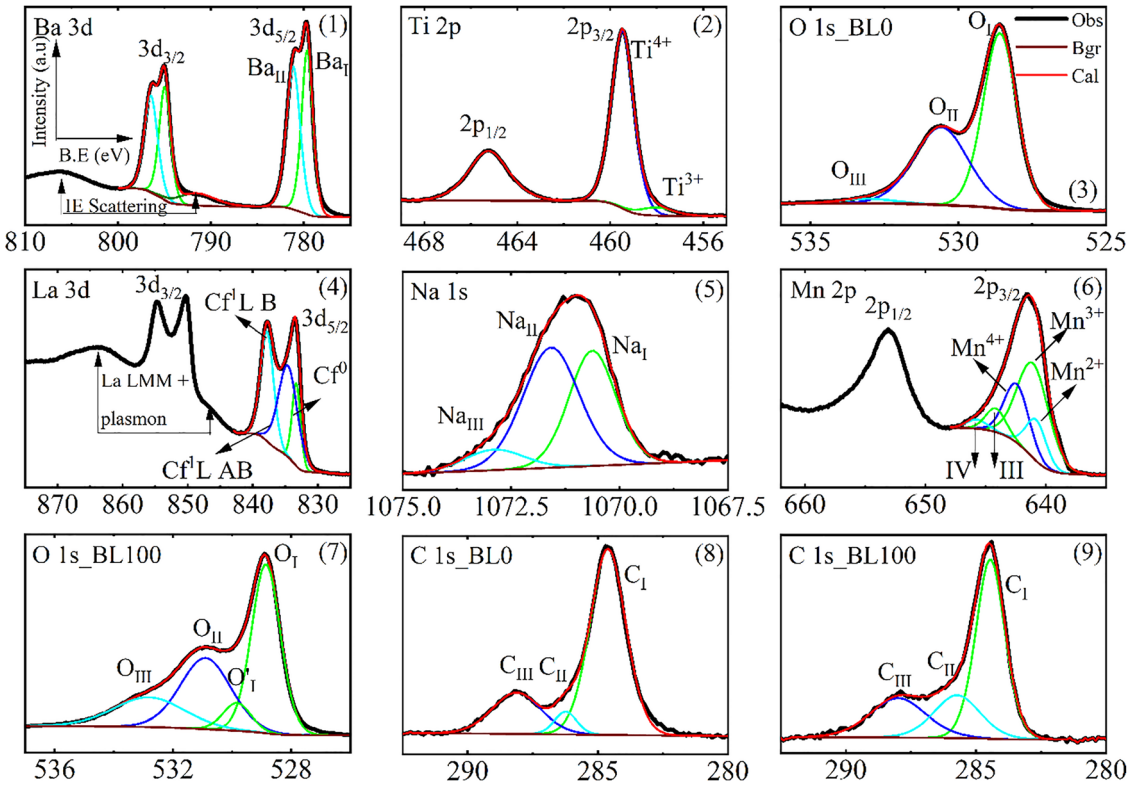

Fig. 7 Deconvoluted XPS core-level spectra of each element in BL0 and BL100.

imbalance caused by oxygen vacancies. The deconvoluted Ti 2p core spectrum is shown in panel 2. A mere visual of the spectrum indicates that there exists a doublet of symmetric nature, but careful inspection revels that there is significant tailing on the lower B.E side of the major component of the doublet. Deconvolution identifies the major component of the doublet at 459.47 eV and its moiety at 463.24 eV, having a B.E separation of 5.77 eV and an intensity ratio of 1.99. The intensity of higher-energy component is significantly lower than that of the main peak, and its FWHM is unusually larger (two times) than that of the major peak. These features of the observed spectra are ascribed to the typical spin–orbit coupling character of Ti^{4+} ions in a perovskite environment, such as $SrTiO_3$, $BaTiO_3$ and oxide lattices such as TiO_2.[80] Spin–orbit coupling splits the Ti 2p core line into two components, the lower-energy $2p_{3/2}$ band and a higher-energy $2p_{1/2}$ band, with a separation of approximately 5.6–5.8 eV and an intensity ratio of 2 : 1. Partial reduction of Ti^{4+} at high temperatures creates Ti^{3+} in quantities less than the detection limit of the instrument, but deconvolution without the Ti^{3+} component did not result in a good fit with a low residual standard deviation. Therefore, the lower-energy feature at 458.00 eV is attributable to Ti^{3+} ions, and it is not visible in the Ti $2p_{1/2}$ band because its intensity is substantially lower compared to the main peak.

The deconvolution of the La 3d core spectra is shown in panel 4. If monochromatic Al Kα radiation is used for photoionization, the strongest signal of La, which is La 3d core line, appears with an intense hostile La Auger signal ($LaM_{4,5}N_{4,5}N_{4,5}$: La MNN) whose interference is usually observed in the energy range of approximately 840 eV to 870 eV. This region is above the La $3d_{5/2}$ SOS component; thus, only the La $3d_{5/2}$ core line was considered for deconvolution. The deconvolution was carried out considering three peaks: cf^0, cf^1L AB and cf^1L B. In perovskites, La is expected to exist in the +3 ground state ($3d^{10}4f^0$). Upon interaction with X-rays, photoelectrons are ejected, resulting in final states described as $cf^0(3d^{10}4f^0 + h\nu \rightarrow 3d^94f^0 + e)$ and $cf^1L(3d^{10}4f^0 + h\nu \rightarrow 3d^94f^1L + e)$, which are also called as unscreened and screened core-level photoemissions, respectively. Here, *c* represents the La core hole, 0 and 1 represent the absence or presence of an f electron, e is the photoelectron and L is a hole in the ligand valence band.[39] The screened core-level peak is further divided into bonding (B) and antibonding (AB) contributions, where in most of the compounds, the cf^1L antibonding and cf^0 overlap. It should be noted that the intensity and separation between the main peaks and satellites are subtle and depends solely on the ligand atom involved in bonding. Having said this, rare-earth compounds are hygroscopic under ambient conditions, and they spontaneously react with moisture to form $La(OH)_3$, not only on the surface but also within the bulk of the sample. La, having formal 3+ oxidation state in La-based perovskites, La_2O_3 and $La(OH)_3$, makes it difficult to identify its local environment; however, the work of M.F. Sunding *et al.*[81] provides a clear pathway to deconvolute and differentiate La-based compounds and to rule out possible hydroxylation. Accordingly, the B.E separation of 4.9 eV between La 3d cf^0 and cf^1L B component, 3.7 eV between cf^1L B and cf^1L

AB component and the intensity ratio of 90 : 10 for $\frac{cf^1L}{cf^0}$ are generic to La_2O_3 and La-based perovskites. In contrast, for $La(OH)_3$, they are 3.9 eV, 2.0 eV and 57 : 43, respectively. In the present investigation, the observed values are 4.5 eV, 3.2 eV and 82.2 : 17.8. This indicates that the local environment of La is essentially La_2O_3 or perovskite-type, with the possibility of partial hydroxylation. The Na 1s core-level deconvolution is shown in panel 5, where the 1s core line appears to be asymmetric towards higher binding energy with sufficient tailing. Consequently, the Na 1s photoelectron spectrum was deconvoluted into three components: Na_I, Na_{II} and Na_{III}, which are situated at 1070.63 eV, 1071.58 eV and 1072.89 eV, respectively. The first two components of highest intensity may be related to sodium in different crystallographic positions,[82] and the third component belongs to Na_2O and/or ionic Na species bound to the surrounding support through –O–Na bonds (in general NaO_x).[83] The formation of sodium carbonate or hydroxides would give rise to a Na 1s peak at sufficiently lower B.E, around Na_I and Na_{II}, and it appears as a shoulder to the main peak. However, this possibility is ruled out, as there is no carbonate peak observed in the C 1s core spectrum (289–290.4 eV) of BL100. The deconvoluted Mn 2p spectrum is shown in panel 6. Transition metals usually possess different valence states, with core lines separated by marginal B.E. differences and severe overlap. This makes deconvolution a challenging. Alongside the multiple valence states of the transition metals in mixed-valent oxides, each transition metal ion, due to its high-spin state, exhibits a broad distribution of multiplets (5 for Mn) with B.E separations on the order of 1 eV.[84,85] Due to these challenges, deconvolution of Mn core spectra in mixed-valent oxides is usually not preferred; however, knowledge of B.E separation between the SOS and the separation from the main peak to oxygen core line are appropriate criteria to infer the chemical state and environment of Mn in each compound. Detailed descriptions of this can be found in some of the notable works.[84–87] In the present case, the large FWHM of Mn $2p_{3/2}$ and Mn $2p_{1/2}$ validates the coexistence of different valence state of Mn, essentially Mn^{3+} and Mn^{4+}, in the sample under investigation (BL100). Furthermore, the shoulder at lower B.E indicates the possibility of the Mn^{2+} oxidation state to be present. Thus, the major peak corresponding to Mn $2p_{3/2}$ was deconvoluted into three major contributions, belonging to Mn^{2+}, Mn^{3+} and Mn^{4+}, from lower to higher B.E. values. The III and IV contributions are assigned to Mn^{3+} and Mn^{2+} multiplets, respectively.[84] The estimated area ratios are 17.42 : 58.21 : 24.36 for Mn^{2+}, Mn^{3+} and Mn^{4+}. The O 1s core spectrum of BL100 is composed of four components: O_I, O_I', O_{II} and O_{III} situated at 528.85 eV, 529.83 eV, 530.89 eV and 532.81 eV, respectively. The first two components, O_I and O_I', belong to lattice oxygen in the $La_{0.835}Na_{0.165}MnO_3$ perovskite framework. The second component, O_{II}, belongs to oxygen vacancies, and the third component, O_{III}, belongs to oxide ions with low electron density in very low coordination states. Such oxygen can be associated with cation vacancies in the oxide structure. The C 1s spectrum of BL100 is very similar to that of BL0, containing three components. A prominent peak at 284.45 eV corresponds to adventitious carbon of the type C–C/C_xH_y. Additional components at 285.73 eV and 288.00 eV, whose intensities are significantly lower than that of the adventitious carbon, are attributable to other carbonaceous species, perhaps C–O and O–C=O. These findings clearly establish mixed valency in BL0 (Ti^{4+} and Ti^{3+}) and BL100 (Mn^{2+}, Mn^{3+} and Mn^{4+}), and cationic and anionic vacancies in them. These chemical and physical attributes are expected to have vivid reflections in the optical, magnetic and ferroelectric properties of these materials.

3.2 Optical studies

To investigate the optical absorption of $BaTiO_3$ and its composites with $La_{0.835}Na_{0.165}MnO_3$ (LNMO) and to estimate their optical bandgap, DRS was employed, and the corresponding room-temperature DRS spectra for each composition are shown in Fig. 8. The basic principle of DRS is provided in the SI.

The spectrum of BL0 can be divided into three distinct regions. Region I corresponds to approximately $\lambda < 200$ nm, at which a large, diffused reflectance is shown by the specimen. Post 200 nm, an abrupt inflection appears, which corresponds to absorption of electromagnetic radiation. This region is regarded as region II, which is typically a strong absorption region extending to 400 nm. Beyond 400 nm, nearly 80% of the incident intensity is diffusively reflected. This marks region III of the observed optical behavior. The observed characteristics of DRS highlight that BL0 is an excellent UV absorber, hinting at its use as an absorber or filter in various applications such as photovoltaics, photocatalysis and cosmetics.[88,89] Upon compositing with 10% LNMO (BL10), the characteristic region III nearly disappears, having just 20% reflected intensity. This signature continues till BL30, with a continued enhancement in absorption. Beyond BL30, the entire spectrum of EM radiation above 200 nm, extending up to infrared, is strongly absorbed. In other words, the act of compositing two perovskites, $BaTiO_3$ and $La_{0.835}Na_{0.165}MnO_3$, successfully transforms the composites into UV-visible absorbers. This development is crucial in the field of optoelectronics, photovoltaics and photocatalysis.[90]

At this point, it is essential to comment on material-specific characteristics of the specimen. The absorption coefficient, $\alpha(\lambda)$, describes how strongly a substance absorbs light at a given wavelength per unit distance.[91] This physical property is of primary importance while discussing the spectroscopic attributes of the material. As the Kubelka–Munk function (KMF), $F(R)$, is directly proportional to absorption coefficient, the variation of $F(R)$ as a function of energy (E) is plotted and shown in Fig. 9.

Evidently, the variation of $F(R)$ a function E shows significant slope changes at definite energies due to the absorption of corresponding photons in the UV and visible region of the EM spectra. In BL0, the absorption maximum is found at 3.66 eV or 343.5 nm, and for BL100, it is found at 1.94 eV or 652.6 nm. Furthermore, a characteristic higher-energy absorption is observed in the UVC region at 5.70 eV and 5.01 eV for BL0 and BL100, respectively. Theoretical calculations emphasize that, in $BaTiO_3$, the VB exist from −4 eV to 0 eV comprising majorly O 2p (p_x, p_y, and p_z) orbitals, and the CB is located approximately from 3 eV to 12 eV, majorly consisting Ti 3d (d_{xy}, d_{yz}, d_{xz}, d_{x^2} and $d_{x^2-y^2}$) orbitals at lower energies. The superposition of O 2p and Ti 3d

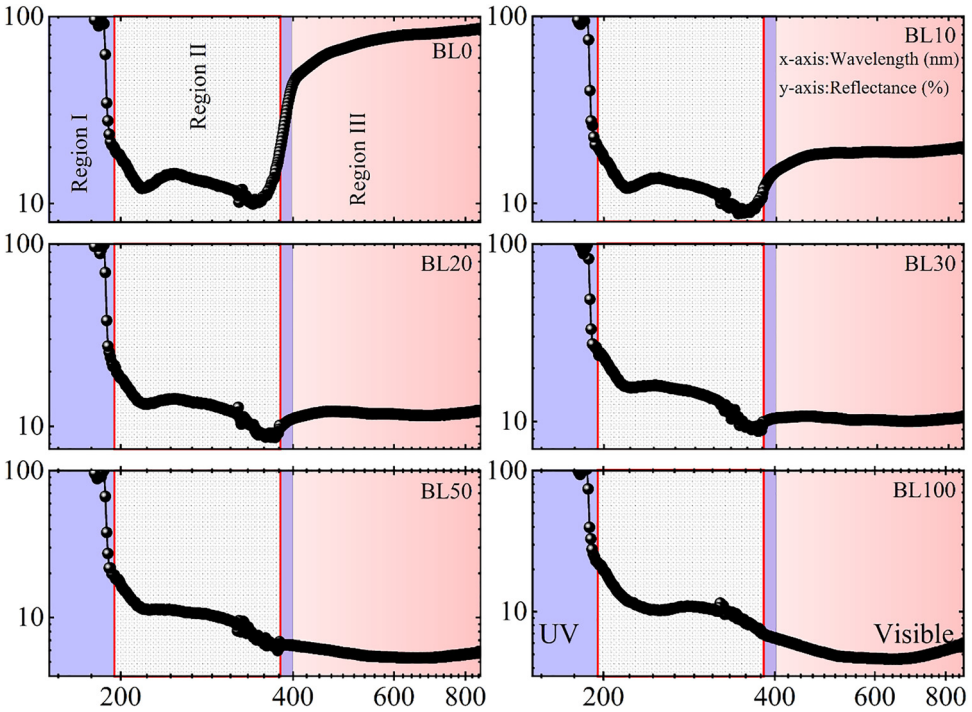

Fig. 8 Room-temperature relative reflectance (R%) as a function of wavelength for $(1-x)BaTiO_3$:$(x)La_{0.835}Na_{0.165}MnO_3$ (x = 0, 10, 20, 30, 50, and 100).

orbitals in the VB and CB leads to strong hybridization, and such hybridization is observed around −4 eV to 0 eV and nearly 3 eV to 10 eV. This results in Ti–O covalent bonds in the TiO_6 environment, whereas Ba–O bonding is ionic in nature.[92–94] Knowing the band structure and the energy separation between absorption doublets (*e.g.*, 3.61–4.51 = 0.85 eV), all absorptions observed in the spectra of BL0 shall correspond to transitions between O 2p levels and the various levels in the conduction band.[95,96] The absorption maxima at 3.61 eV and 3.86 eV shall correspond to the strongest absorptions above the indirect absorption edge (located at around 3.2 eV).[97,98] The absorption edge (cannot be distinctly observed in the spectra) traces its origin to excitation of electrons from O 2p orbitals in the VB to the partially filled Ti 3d t_{2g} orbitals in the CB (R → Γ). However, some early reports consider these absorptions to correspond to indirect Γ → X or direct $\Gamma_{15} \rightarrow \Gamma_{25'}$ and $\Gamma_{15} \rightarrow \Gamma_{15}$ transitions, representing 2p to Ti 3d t_{2g} and 2p to Ti 3d e_g electron excitations, respectively.[99–102] Keeping the 3.61 eV–3.86 eV range (direct Γ transitions) as the central absorption energy, a small hump observed in the lower energy range from 2.66 eV to 3.00 eV corresponds to electronic transitions related to off-stochiometric phase of $BaTiO_3$ having oxygen and/or cationic vacancies, which validates the structural and XPS findings.[103] The vacancies or defects establish new levels between the highest occupied molecular orbitals (HOMO) and the lowest unoccupied molecular orbitals (LUMO). The absorptions observed at higher energies essentially at the UV regime, 4.51 eV (X transitions: $X_{5'} \rightarrow X_5$), 5.70 eV (direct M transitions) and 6.42 eV (Γ transitions and/or X transitions: $X_{5'} \rightarrow X_1$), correspond to higher-order ligand-to-metal charge-transfer (LMCT) transitions, essentially from O 2p to Ti 3d e_g orbitals in the CB.[95,104–107] Note that the Γ, X, M, and R are the usual high symmetry points in the Brillouin zone of the crystal lattice. In fact, the transition at 4.5 eV is a generic transition of $BaTiO_3$, $SrTiO_3$ and $PbTiO_3$ perovskites. This further confirms that the majority phase in BL0 is perovskite $BaTiO_3$. LMCT transitions to Ba 5p orbitals from O 2p is ruled out, as the energy range (3.2 eV–7.5 eV) corresponds majorly to transition between Ti 3d and O 2p-derived states.[98,108,109] Thus, the optical studies support the structural findings that BL0 majorly contains $BaTiO_3$, but it is essentially off-stoichiometric in nature.

Similar to $BaTiO_3$, $LaMnO_3$ has a perovskite structure, meaning the Mn ion is in octahedral coordination with oxygen. The electronic configuration of Mn in octahedral coordination of parent manganites (*e.g.*, $LaMnO_3$ and $CaMnO_3$) is such that it has 4 or 3 electrons in the d orbital. The electrostatic crystal field (cf) is established due to O^{2-} in the surrounding, which splits the d levels into two sub-bands (cf splitting energy, Δ_{cf} = 10 Dq = 1.5 eV): the low-energy t_{2g} orbitals (d_{xy}, d_{yz}, and d_{xz},) and the high-energy e_g orbitals (d_{x^2} and $d_{x^2-y^2}$). It is important to note that the Jahn–Teller effect further splits these bands in the case of perovskites having Mn^{3+} at the B-site, as it has only one electron in the e_g band containing degenerate orbitals. In the case of $LaMnO_3$ or in general in rare-earth manganites, the Fermi level (E_F) lies between these split bands. Thus, the band structure is such that partially filled Mn 3d t_{2g} orbitals, O 2p orbitals, and low-lying partially filled or empty Mn 3d e_g orbitals majorly form the VB, and the Mn 3d e_g orbitals form the HOMO (there are, however, speculations on the position of t_{2g} orbitals whether they are above or below the O 2p orbitals). The empty Mn 3d e_g band appears as the LUMO.[110] Thus, if the external energy (photon energy) exceeds 1 eV, the optical spectra can be satisfactorily interpreted in terms of electronic

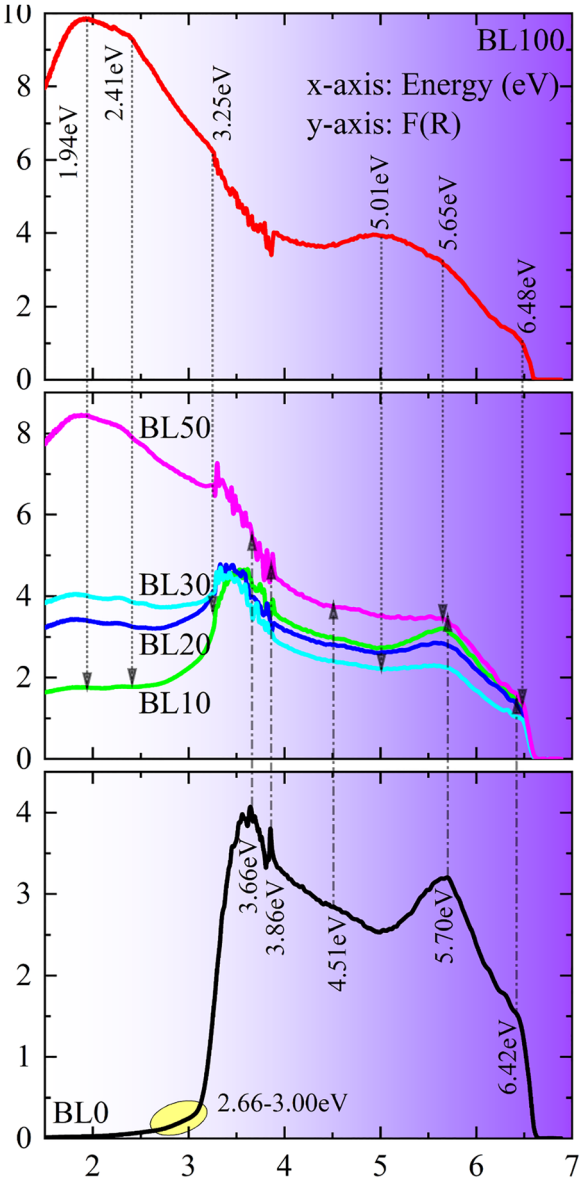

Fig. 9 Variation in $F(R)$ plotted as a function of E in the energy range of 1.5 eV to 7 eV for $(1-x)BaTiO_3$:$(x)La_{0.835}Na_{0.165}MnO_3$ (x = 0, 10, 20, 30, 50, and 100).

transitions between energy levels of the MnO_6 complex or between levels of two neighbouring Mn ions and between the O 2p orbitals and Mn 3d e_g levels.[111] It should be noted that the O 2p orbitals strongly hybridize with the lower-energy Mn 3d e_g band (partially filled or empty), raising the speculation on the HOMO levels, whether they are of Mn or O. Apparently, this band structure results in parent manganites having a very narrow band gap of 0.4 eV to 1.5 eV, which is susceptible to temperature variations. Hole doping and/or oxygen off-stoichiometry shall reduce the band gap or may even close it due to the formation of hole states above the E_F and the tailing of the CB towards the E_F, respectively.[55,112–114]

It has been proven that in hole-doped manganites, the band gap, if exists at all, increases as temperature increases, accounting for the FM-to-PM transition, and there is a finite, nonzero gap in the PM region even in metallic manganites.[111] It is established in various studies that a broad absorption band around 2 eV above the absorption edge (centered at 1.94 eV in the present case) corresponds to multiple overlapping electronic transitions of different origins. It contains forbidden or weakly dipole-allowed 2p–3d CT transitions and dipole-forbidden, spin-allowed intra-Mn or also called intersite low-energy high-spin d–d CT transitions. They are denoted as $t_{2g}(\pi) \rightarrow e_g$ (1.3 eV–1.9 eV), $t_{2u}(\pi) \rightarrow e_g$ (2.3 eV–2.7 eV) and $d(e_g)$–$d(e_g)$ (2 eV–2.2 eV).[115–118] The spectral features around 3 eV–3.8 eV originate from weakly dipole-allowed 2p–3d CT $t_{1u}(\pi) \rightarrow e_g$ transitions of π–σ nature, and the feature from 5 eV to 5.3 eV belongs to strongly dipole-allowed 2p–3d CT $t_{1u}(\pi) \rightarrow e_g$ transitions of σ–σ nature. Perhaps, there even exist weak signatures of weak low-spin d–d CT transitions in this region, ranging from 4.7 eV to 5.3 eV. As the specimen under discussion is mixed-valent, some researchers assign the d–d CT transition to $^5E_g \rightarrow {}^5T_{2g}$ ($d(e_g)$–$d(t_{2g})$) for Mn^{3+} and $^4A_{2g} \rightarrow {}^4T_{2g}$ ($d(t_{2g})$–$d(t_{2g})$) for Mn^{4+}.[119] The shoulder observed at 3.2 eV (3.25 eV in the present case) may correspond to the dipole-allowed 2p–3d CT transition $t_{1u}(\pi) \rightarrow e_g$ of Mn^{3+} (ref. 114) and/or 2p–3d CT transition $t_{1g}(\pi) \rightarrow t_{2g}$ of Mn^{4+} (also denoted as $^4A_{2g} \rightarrow {}^4T_{1g}$).[120–123] Due to the complexity of band structure of manganites, one may assign the observed absorbance to different origins based on the respective scenario. Nevertheless, at lower energies, the absorption is without any doubt majorly d–d transitions involving e_g states, and at higher energies, it is majorly due to p–d transitions involving O 2p and Mn 3d e_g states. A very interesting part of the absorption spectrum of BL100 is the first high-energy shoulder of the maximum, *i.e.* at 2.41 eV. This feature is typical to ferromagnetic hole-doped semiconducting manganites (metallic to be precise). It is not seen in magnetic insulators such as $Pr_{0.8}Sr_{0.2}MnO_3$. This means that the spectral feature is an identifier of the type of electrical ground state of the specimen and appears only when the band structure is changed such that the contribution of free charge carriers becomes predominant, or to state it differently, this feature arises from optimal mixed valency (Mn^{3+}/Mn^{4+}), giving rise to metallicity in the sample. Undoubtably, this feature is associated with $d(t_{2g})$–$d(e_g)$) transitions or Mn^{4+} $t_{2g} \rightarrow$ O 2p $\rightarrow Mn^{4+}$ e_g interband transitions.[120,124] Meanwhile, the broad absorption maximum observed at 5 eV is attributable to U_{pd} interactions, which correspond to the energy cost of transferring an O 2p electron to a neighbouring d ion to create a p^5d^{n+1} charge excitation from the p^6d^n state.[55] The slope change at energies higher than 5 eV perhaps corresponds to O 2p $\rightarrow e_g\downarrow$ and $t_{2g}\downarrow$ transitions, as they appear at relatively higher energies in the conduction band (5 to 6 eV).[112] For instance, the low-intensity shoulder at 6.48 eV perhaps corresponds to charge-transfer transition from O 2p to Mn^{4+}, essentially $1t_{1g} \rightarrow 7a_{1g}$, $6t_{1u} \rightarrow 7a_{1g}$ and $1t_{1g} \rightarrow 2t_{2g}$.[125] There are no signatures of O 2p $\rightarrow$ La 5d transitions, as La 5d orbitals appear at significantly higher energies (nearly 9 eV),[112,113] and there is no possibility of any optical transitions corresponding to Na, as the states related to Na^+ (s and p orbitals) are located well below the Fermi level. However, the presence of Na^+ certainly improves the covalency

between Mn 3d and O 2p or in other words, the hybridization between the Mn 3d and O 2p orbitals.[126] Based on the occurrence of strong absorption features at low energy (<2 eV) and high energy (4.5 eV to 5.5 eV), BL100 can be regarded as a metal with no band gap or a semiconductor with an extremely narrow band gap. To sum up, unlike $BaTiO_3$, where the observed spectral features correspond only to p–d CT transition across the entire spectral range, there is a vivid bifurcation in manganites where the features below 3 eV majorly originate from d–d CT transitions, and transitions above 3 eV correspond majorly to p–d CT transitions.[123] Thus, the variation of $F(R)$ as a function of E clearly establishes the fact that BL0 is a charge-transfer insulator, and BL100 is a metal at RT.

The composites show optical signatures of the end members of the series, with competing absorption maxima depending on the concentration of either of the end members. Interestingly, the slope changes observed at lower energies show broadening and a red shift with respect to the BL100 end member of the series. The characteristic 2p–3d strongest absorption typical of $BaTiO_3$ exists in the energy range between the maxima of BL100 and BL0, undoubtably showing softening and a red shift with respect to BL0. The broad secondary maxima observed at 5 eV in BL100 disappears in the composites, whereas the rest of the high-energy slope changes resemble those of BL0. This indicates that at low energies, the composites inherit the manganite nature, and at high energies, they behave like $BaTiO_3$. They are both Mott–Hubbard insulators and CT insulators. This confirms the true composite nature of the specimens, where the electronic structures of the parent specimens distinctly exists in the corresponding composites without a significant tradeoff at the cost of others. However, the red shift and softening of absorption signatures at low energies indicate changes in the band structure or reduction in corresponding gap perhaps due to the addition of intermediary levels. These intermediary levels come from defect states introduced into the sample. It is worth noting that the persistence of absorption features that resemble mixed-valent manganites in the range of 2.2–2.5 eV (in this case at 2.3 eV) in the composites indicates appreciable amount of free charge carriers in the composites. This feature is enhanced with an increase in the amount of $La_{0.835}Na_{0.165}MnO_3$. This feature exists even in BL10, ascertaining that it shall have conducting ferromagnetic nature, unlike $BaTiO_3$, which is an insulating diamagnet.

Using an analogy with Tauc's law $\left(\alpha h\nu = B\left(h\nu - E_g\right)^{\frac{1}{m}}\right)$, the KMF enables one to estimate the optical band gap. By replacing α by $F(R)$ in Tauc's law, it becomes $F(R)h\nu = B\left(h\nu - E_g\right)^{\frac{1}{m}}$. The physical quantity $(F(R)h\nu)^m$ is plotted against the photon energy $h\nu$. Here, B is an independent parameter of photon energy that characterizes the degree of disorder in the polycrystalline material under investigation. Here, m = 2 corresponds to a direct allowed optical transition, and m = 1/2 corresponds to an indirect allowed optical transition. The x-intercept of the plot, extrapolated from the linear region of $(F(R)h\nu)^m$ *versus* $h\nu$, gives the optical band gap E_g of the specimen.[127]

Fig. 10 depicts the variation of $(F(R)h\nu)^2$ *versus* $h\nu$ and of $(F(R)h\nu)^{\frac{1}{2}}$ *versus* $h\nu$, enabling the estimation of direct allowed and indirect allowed band gap of BL0 and BL100. The estimated E_g of BL0 for direct and indirect allowed transitions are 3.23 eV[128] and 3.01 eV, respectively (Table 4). It should be noted that the absorption edge in case of BL100 is not observed. However, based on prior knowledge of the band gap of La-based manganites, and assuming that there exists an

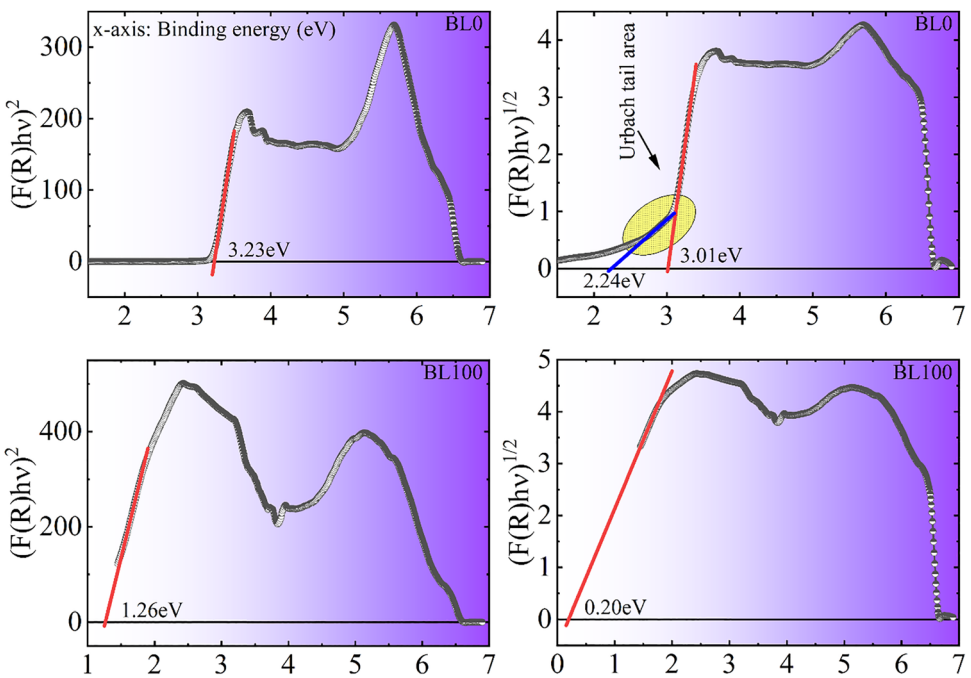

Fig. 10 Tauc plot of $(F(R)h\nu)^m$ *versus* $h\nu$ for m = 2 and m = 1/2 to estimate the direct allowed and indirect allowed band gap of BL0 to BL100.

Table 4 Comparison of the direct allowed band gap (E_g^{Dir}), indirect allowed band gap (E_g^{Indir}), charge transfer gap (E_{CT}^{Dir}) and Urbach energy (E_U) for relative analysis

Concentration (%)	E_g^{Dir} eV	E_g^{Indir} eV	E_{CT}^{Dir} eV	E_0 eV	E_U meV	S
0	3.23	3.01	4.36	3.18	93.83	0.276
10	3.13	2.64	4.26	3.26	217.28	0.119
20	2.99	2.26	3.55	3.27	597.78	0.0433
30	2.95	1.95	3.40	3.28	136.28	0.190
50	2.38/ 1.06	−0.31/ −0.45	0.85	—	—	—
100	1.26	0.2	3.58	—	—	—

absorption edge, E_g for BL100 is estimated to be 1.26 eV and 0.20 eV for direct and indirect allowed transitions, respectively. A rough estimate of E_g can also be obtained from the first-order derivative of $F(R)$ with respect to E.[127] The obtained values of band gaps for BL0 and BL100 are consistent with earlier reports;[96,98,100,118,129–133] however, there are discrepancies in the literature on the nature of the allowed optical transition for $BaTiO_3$, whether it is direct or indirect. It has been reported that both tetragonal and cubic phases of $BaTiO_3$ exhibit an indirect band gap ($R \rightarrow \Gamma$) very close in energy to the direct band gap ($\Gamma \rightarrow \Gamma$), making it difficult to discriminate between the two by experimental techniques.[102,134,135] The natural logarithm applied to Tauc's law indicates that $\ln(F(R)h\nu)$ plotted against $\ln(h\nu - E_g)$ should yield a linear relationship with slope $1/m$, which is the constant of optical transition. The proximity of $1/m$ to the ideal values 1/2 and 2 validates the possible optical transition. The value of $1/m$ estimated for BL0 are 0.50 and 2.06. This states that BL0 has a likelihood to be both direct and indirect band gap material and validates the anomaly of nature of allowed optical transitions reported. The value of $1/m$ estimated for BL100 are 0.50 and 1.96. This indicates that BL100 has a direct band gap, which is in accordance with many optical studies on manganites with similar value of E_g.[118,126,136–138] Nevertheless, this study emphasize that may it be direct or indirect gap, BL100 has a large population of free charge carriers. The band structure is such that, due to hole doping (33%) and oxygen off-stoichiometry, the LUMO levels are significantly shifted towards the E_F. The band gap becomes extremely narrow, or it has disappeared, giving metallic nature to BL100 at RT (below T_C). Furthermore, other than the prominent low-energy linear region enabling the estimation of optical band gap, the Tauc plot consists of another linear region at the higher energy side, which corresponds to perhaps multiple higher-order charge-transfer transitions, essentially from the O 2p valence band to the Ti 3d conduction band (e_g orbital).[101] This feature is also seen in BL100, which shall correspond to multiple p–d CT and d–d transition between t_{2g} and e_g (Mn 3d) orbitals. Generally, $BaTiO_3$ is unlikely to show the said characteristic unless otherwise there exist mixed valency in the system. In the present case, mixed valency can arise from oxygen off-stoichiometry or cationic vacancies in the system. The existence of mixed valency in BL0 has already been established through magnetic and XPS analysis. To addon, the profound linearity found in the low-energy region (Fig. 10) indicates that the prepared sample not only contains the

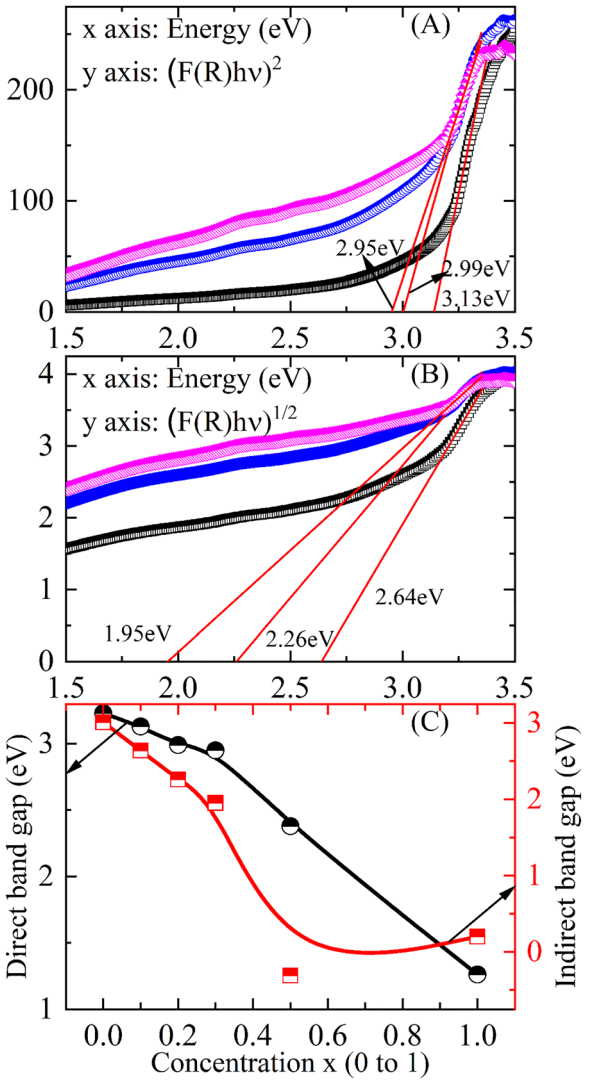

Fig. 11 Tauc's plots of BL10, BL20 and BL30, estimating the direct allowed and indirect allowed band gaps (A) and (B) and the variation in E_g across the series.

$BaTiO_3$ phase with a wide band gap but also a nonstoichiometric phase with a narrow band gap (2.24 eV), which extends absorption to the visible region of the EM spectra.[103] This stand as further evidence to mixed valency in BL0. The estimated CT gap (E_{CT}^{Dir}) is found to be 4.36 eV, which is similar to the reported value elsewhere.[139] The CT gap of BL100 is 3.58 eV.

Fig. 11A and B show the Tauc's plots of BL10, BL20 and BL30; the Tauc plot of BL50 is not shown here. BL50 is found to have two vivid linear regions at lower energies (1.5 eV–2 eV and 3.2 eV–3.33 eV), corresponding separately to the band gap energies of BL100 and BL0, respectively. The variation of E_g relative to BL0 is shown in Fig. 11C. The variation shows a relatively linear fall up to BL30, being abrupt thereafter. The E_{CT}^{Dir} also shows a similar variation, which is not shown here. It should be noted that each of these Tauc's plots contains two distinct linear regions in the first absorption regime: one at the lower-energy part and the other at the higher-energy range of

the inclination (3.00 eV–3.3 eV and 3.3 eV–3.50 eV). This means that the overall absorption is not abrupt, but rather gradual upon compositing. As per standard analysis for band gap estimation, the immediate linear region next to the exponential growth is considered in the present investigation for estimation of E_g. Before one attempt to explain the reduction in E_g, it is essential to consider the overall softening of inclination of $\alpha(\lambda)$ in the strong absorption regime and the significant tailing of absorption below the absorption edge. Both findings, especially the tailing (Urbach tail), are a direct indication of high defect densities or disorders in the system.[92,107,140,141] Absorption coefficient has exponential growth with respect to energy in the tail region. The relationship is given by $\alpha(E,T) = \alpha_0 \exp\left(\frac{E-E_0}{E_U}\right)$, where α_0 and E_0 are constants called Urbach focus (E_0, α_0) or convergence point. The α_0 (scaling parameter) and E_U (rate parameter) decide the exponential growth. E_0 is frequently referred to as the absorption edge energy, and it is roughly equal to the energy of the lowest free exciton at zero lattice temperature, or, in other words, the energy of the band edge in an ideal or unperturbed structural environment. The expression is widely known as the Urbach rule or Martienssen–Urbach (MU) rule.[94,139,142] The MU rule enables the estimation of E_U by taking the natural logarithm of $F(R)$, where it shows exponential growth (only the tail part) near the absorption edge. The resulting variation as a function of energy E or $(E - E_0)$ is then fitted to a straight line, and the inverse of slope represents E_U. However, in the present investigation, the differential analysis and deconvolution proposed by Canul *et al.*[143] is used to estimate E_0 and E_U. The advantage of this method over the conventional method is that it enables the estimation of E_0 and E_U even in materials with nonlinear band edges and complex fine structure. To illustrate the estimation E_0 and E_U, the plots depicting the calculation for BL0 are shown in Fig. 12.

The E_U of BL0 is close to the reported value for tetragonal polycrystalline bulk $BaTiO_3$, which is 84–86 meV. As E_U a measure of total disorder, it is expected to increase with structural disorders and defects at the micro- to nano-scale. For instance, nanocrystalline $BaTiO_3$ films have an E_U of 260 meV. The slightly higher value of E_U for BL0, *i.e.*, 97 meV, asserts the existence of defects in $BaTiO_3$. Prior to the estimation of E_U, the gradual increase of $\alpha(E,T)$ in the tail region itself is a visual proof for resident disorders in the system, which gives rise to weak absorptions due to electronic transitions between extended bands and localized states (Urbach-band-tail states) in the forbidden gap. The disorder in this case is likely produced by impurities or defects, such as O and Ti vacancies.[144] Another parameter that indicates the inclination and width of straight-line near the absorption edge is the steepness parameter, S, given by $S = \frac{k_B T}{E_U}$. This parameter is a measure of the strength of electron–phonon interactions. A reduction in S indicates enhanced electron–phonon interaction in the composites.

Finally, the task of compositing BTO with LNMO results in composites with a high density of defect states, effectively extending the absorption into the visible region of the EM spectra, or to state it differently, the act of compositing BTO and LNMO results in a systematic reduction in E_g. This development can effectively translate into applications in photodetection, photovoltaics and high-temperature optoelectronics. Furthermore, the visible band gap, high Urbach energy and induced magnetism are perfect combinations of characteristics needed for water splitting and photocatalysis for degradation of pollutants such as dyes.

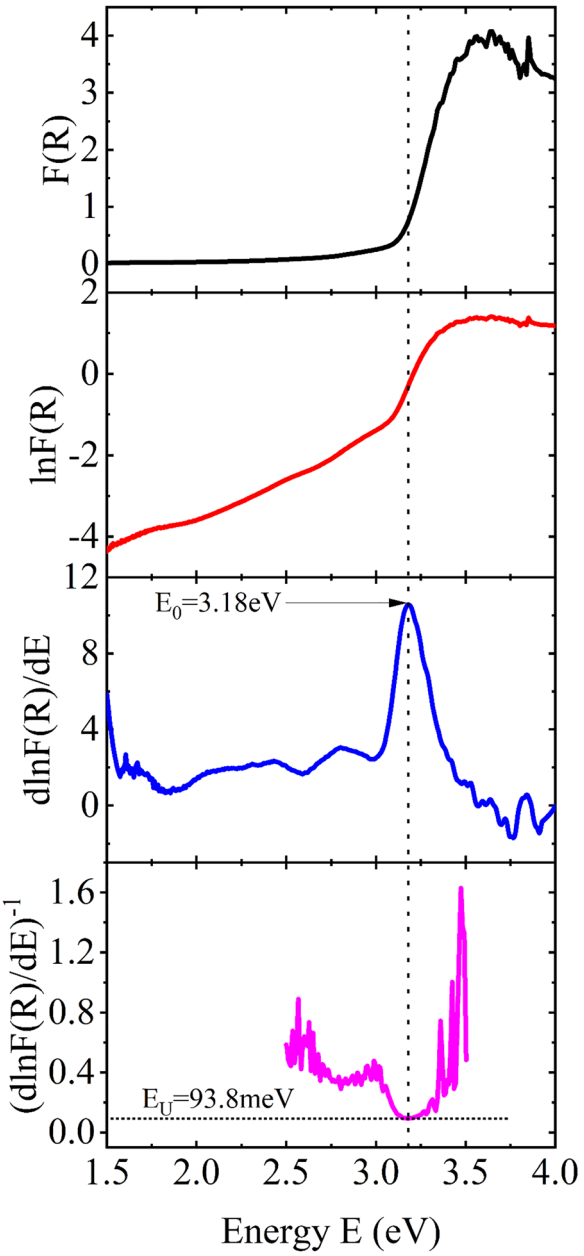

Fig. 12 Plots of $F(R)$, $\ln F(R)$, the first-order derivative of $\ln F(R)$ with respect to energy, and the inverse of this derivative for the estimation of the Urbach focus and Urbach energy, E_0 and E_U.

3.3 Magnetic characteristics

The temperature dependence of magnetic susceptibility, $\chi(T)$, in zero field–cooled (ZFC) and field-cooled (FC) modes, along

with the first order derivative, $d\chi/dT$, and the inverse susceptibility, $\chi^{-1}(T)$, for BL0 and BL100 are shown in Fig. 13 (panels A, D, B, E, C and F, respectively). The $BaTiO_3$ in its stochiometric form is a ferroelectric insulator. A perfect $BaTiO_3$ lattice is diamagnetic due to null value of free electron spin (S = 0) in each ionic species that are involved in the formation of $BaTiO_3$.[145] However instead of showing diamagnetism, BL0 shows $\chi(T)$ variations that change between small positive values, showing inflections at two points as T reduces from 400 K. The first abrupt shift in FC susceptibility to a higher positive value occurs at 127 K, followed by a second at 16.5 K. The increase is almost semi-saturated (constant slope) till 16.5 K and then there is sudden escalation to continuously growing susceptibility. The nature of ZFC susceptibility is contrasting in the case of both $\chi(T)$ and $\chi^{-1}(T)$. Interestingly, the ZFC χ shows an intermediate transition at 118 K, and the magnitude of ZFC susceptibility shows a maximum (cusp) at 125 K, before it decreases to a magnitude less than its high-temperature value (below 118 K). The $\chi^{-1}(T)_{ZFC}$ shows a dip at 125 K, then escalates to a significantly larger value and falls off again below 16.5 K. The FC and ZFC curves show a significant bifurcation below 127 K; however, the bifurcation starts far above (230 K) the transition temperature. The difference between FC and ZFC susceptibilities, $\Delta\chi$, is nonzero from ~230 K, and it is equal to 2.85×10^{-6} emu g^{-1} Oe^{-1} at the lowest measured temperature. This implies a very high magnetic anisotropy in the system. Here, all transitions are identified using $d\chi/dT$. The minimum (#) observed in $d\chi/dT$ (127 K) indicates a weakly ferro/ferrimagnetic (FM/FEM) transition, and the maximum (@) at 118 K indicates spin frustration. The overall behavior below 230 K, particularly below 127 K, suggests a cluster glass (CG) or a spin glass (SpG)–like state.[146] It is assumed that a random distribution of clusters of nonmagnetic, stochiometric $BaTiO_3$ containing Ti^{4+} and ferromagnetic non-stoichiometric $BaTiO_3$ and its nonequilibrium phases (containing mixed valency as a consequence of B-site deficiencies and oxygen vacancies) of different sizes is responsible for magnetic frustrations at low temperatures. Density functional calculations by Raeliarijaona *et al.*[147] revealed the underlying mechanism that establishes FM in ferroelectric $BaTiO_3$ by considering the native vacancies. The possible vacancy states that can induce FM in $BaTiO_3$ are V_{O1}^0, V_{O2}^0, V_{Ti}^{3-}, V_{Ti}^{2-}, V_{Ti}^{1-}, V_{Ti}^0 and V_{Ba}^0, depending on processing conditions. Here, V_q^X denotes a vacancy of species X carrying a charge of q. Under O-rich conditions, cationic vacancies are most favourable and *vice versa*. Generally, the most considered vacancies are V_{Ti}^{3-} and V_{O1}^0 due to their extended stability under two extreme PO_2 conditions. Amongst all, FM induced by V_{Ti}^{3-} is very stable and has a large magnetic moment compared to other vacancy species, whereas the moments associated with V_{O1}^0 and V_{O2}^0 are minimal. Furthermore, based on these calculations, the AFM state is not possible in $BaTiO_3$, as there is no species of vacancy that contains a null magnetic moment and possesses the negative energy difference essential for AFM ordering. The origin of FM induced by cationic vacancies lies in spin polarization of itinerant holes at O 2p orbitals, whereas the magnetism from oxygen vacancies originates from the spin polarization of

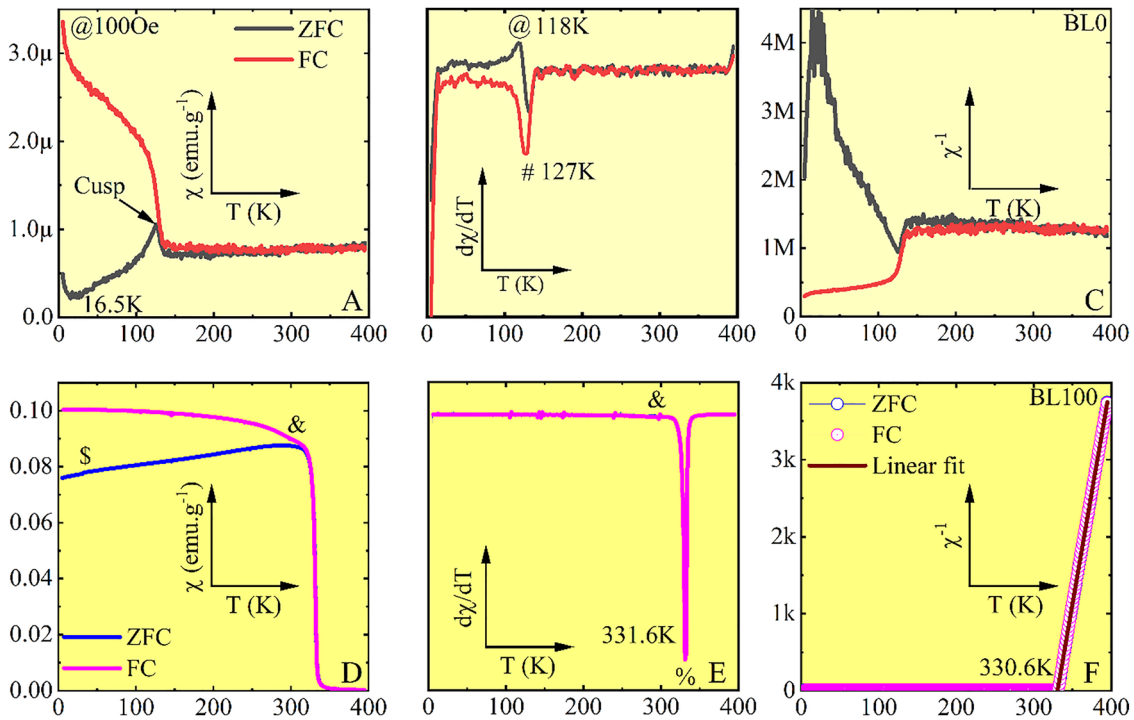

Fig. 13 Temperature dependence of the magnetic susceptibility of BL0 (A) and BL100 (D) measured in zero-field cooled and field-cooled mode at a magnetization intensity of 100 Oe. The $d\chi/dT$ (BL0:B and BL100:E) indicates the different inflection points in the susceptibility curve. The inverse susceptibility (BL0:C and BL100:F) is used to depict the typical magnetic nature of the specimens.

itinerant electrons at Ti t_{2g} orbitals.[148] Finally, this induced magnetism due to cationic and anionic vacancies shows a significant temperature dependence. It is interesting to note that the net magnetic moment of V_{O1}^{0} becomes virtually null beyond 120 K, but the FM from V_{Ti}^{3-} can survive even at very high temperatures ($\sim$1300 K). It has also been identified that V_{O1}^{0} vacancies are more susceptible to forming due to their low formation energy.[148] Therefore, an oxygen vacancy at the surface can effectively create mixed valency for Ti (Ti^{3+}/Ti^{2+}), which directly contributes to the FM in $BaTiO_3$.[149] These findings from the literature enable the assertion that perhaps both V_{O1}^{0} and V_{Ti}^{3-} are possible vacancies that exist in BL0 under a given normal PO_2 and short sintering durations. The magnetic transition observed at 127 K is in agreement with the FM transition induced by oxygen vacancies. It is believed here that there exists a random distribution of FM clusters of different sizes in BL0. Upon ZFC, these clusters freeze into random orientations dictated by a local anisotropy field. When field-cooled, the clusters align, and they lead to the onset of a large FM-type magnetization, unlike in cases of competing FM and AFM interactions, where the FC curve saturates. The failure to fit the Curie–Weiss law at temperatures above the transition temperature or freezing temperature T_f is because of the significant diamagnetic background in the paramagnetic susceptibility. The observed RT FM in BL0 with a robust SpG state at low temperature is attention-worthy for a wide range of multiferroicity in the so-called prototype ferroelectric $BaTiO_3$.

Reported studies on $La_{0.835}Na_{0.165}MnO_3$ reveal that it is a second-order soft ferromagnetic semiconductor with a Curie temperature T_C in the range of 321–343 K.[37,150] In the present case, BL100 shows a sharp PM to FM transition with a decrease in temperature. The transition temperature, T_C, is 331.6 K (marked as %). This value does not match any previously reported value, perhaps due to the nonstoichiometry observed in BL100 compared to nominal $La_{0.835}Na_{0.165}MnO_3$. The large magnetic sensitivity, nearly -1.6 emu g^{-1} K^{-1}, indicates the abruptness of the magnetic transition and reflects a significant response of magnetic moments to a small change in the applied magnetic field (100 Oe). Furthermore, a small hump in the FC curve is observed around 296 K (marked as &), which is interesting as the monoclinic manganite secondary phase is concerned. Such a hump is a consequence of a PM to FM transition in a $La_{0.9}MnO_3$-like phase.[151–153] Generally, $La_{1-x}MnO_3$ has a limiting value of the self-doping range. Any composition $x > 0.125$ exhibits saturation with respect to physical properties such as the extent of rhombohedrality (constant rhombohedral angle α) saturate, leading to the precipitation of parasitic Mn_3O_4 impurity phase and a constant T_C (250–260 K).[44,151,153–155] However, the unusually high transition temperature of 296 K can be due to multiple double-exchange interactions facilitated by the incorporation of Mn^{2+} at the A-site of the crystal lattice.[73] The occurrence of two different T_C values, essentially for rhombohedral and monoclinic manganites, can be understood by considering the static coherent Jahn–Teller (JT) distortion. Ferromagnetism in manganites occurs due to the simultaneous hopping of e_g electrons between B-site cations (Mn^{3+} and Mn^{4+}) *via* a bonding ligand. The strength of this hopping depends on the extent of mixed valency, the average bond length ($\langle$Mn–O$\rangle$) and the average bond angle ($\langle$Mn–O–Mn$\rangle$). Structural distortions and mismatches in the orbital overlap between ligands and cations play a crucial role in deciding the transfer integral for double-exchange hopping. This dictates the correlation between ferromagnetism and JT distortion mediated by spin-charge-lattice coupling. The coherent distortion parameter, σ_{JT}, is defined as $\sigma_{JT} = \sqrt{\frac{1}{3}\sum_i \left[(\mathrm{Mn-O})_i - \langle \mathrm{Mn-O}\rangle\right]^2}$. Here, $(\mathrm{Mn–O})_i$ are the three independent Mn–O bond lengths, and $\langle$Mn–O$\rangle$ is the average Mn–O bond length.[156] In the rhombohedral $R\bar{3}c$ SG, all three Mn–O distances are equal. Thus, the coherent JT distortion parameter is zero. The static coherent JT distortion of the MnO_6 octahedra provides an additional carrier localization in distorted perovskites. Therefore, the absence of static coherent JT distortion is favourable for the hopping of e_g electrons and leads to an enhanced DE interaction, which gives rise to a high Curie temperature T_C for rhombohedral manganites. In contrast, σ_{JT} calculated for the monoclinic phase is nonzero but has a value of 0.050. This accounts for the lower T_C observed for the monoclinic phase and thus two transitions observed in the $\chi(T)$ variation of BL100. In this context, the bandwidth of conduction electrons indicates whether an electron is itinerant or localized, thus deciding the exchange interactions between magnetic ions, Mn^{3+} and Mn^{4+}. The bandwidth W is defined as $W \propto \frac{\cos(w)}{d_{\mathrm{Mn-O}}{}^{3.5}}$, where $w = \frac{\pi - \langle \mathrm{Mn-O-Mn}\rangle}{2}$, and $d_{Mn–O}$ is $\langle$Mn–O$\rangle$. The estimated bandwidths for the rhombohedral and monoclinic phases are 0.095 and 0.093, respectively. Clearly, the smaller bandwidth of the monoclinic phase reduces orbital overlap between ligands and cations involved in the hopping mechanism. The bandwidth estimated for BL0 is found to be 0.086, which justifies the insulating nature of BL0 amidst weak ferromagnetism that it displays and the low T_C of 127 K. The ZFC of BL100 shows a small cusp at 42 K, indicative of a ferrimagnetic transition of Mn_3O_4.

The temperature dependence of $\chi(T)$ in ZFC and FC modes, the $\chi^{-1}(T)$ and temperature dependence of $d\chi/dT$ for BL10, BL20, BL30 and BL50 are shown in Fig. 14. Each composite displays a vivid PM to FM transition similar to that of BL100, except for the fact that an unusual thermal hysteresis is observed between the ZFC and FC curves in the temperature range from 290 K to 330 K, where they finally merge to show PM nature. Here, the ZFC curve appears above the FC curve, which is a mere consequence of loosely held titanate and manganite particles/gains at the microscopic level (the poor compactness and large porosity are discussed in the microstructural analysis of composites). A similar feature has been reported in Fe^{3+}-doped CdS nanoparticles, where the said feature observed in powders disappears after proper pelleting.[157] The susceptibility increases as the BL100 concentration increases, indicating the inclusion of magnetic material into the nonmagnetic matrix. Interestingly, the small jumps observed at 296 K and 42 K in the FC curves, as well as the cusp at 42 K observed in the ZFC curve

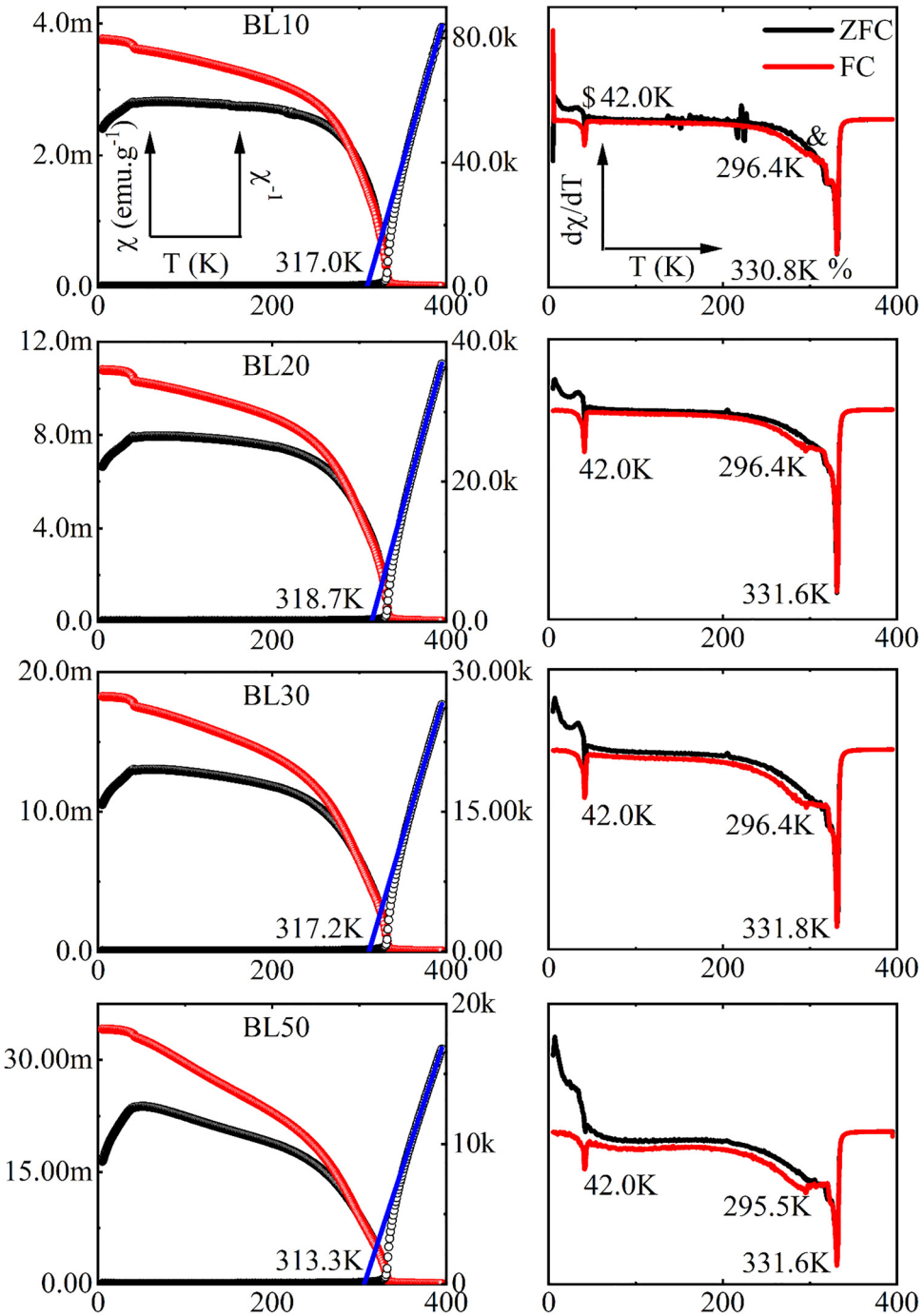

Fig. 14 Temperature-dependent variation of dc susceptibility (left *y*-axis of left panel), temperature-dependent variation of inverse susceptibility (right *y*-axis of left panel) and the first-order derivative of susceptibility (right panel) for all the composite compositions.

of BL100, become very prominent in the temperature-dependent variation of $\chi(T)$ and $d\chi/dT$ (marked as & and $ in Fig. 11, respectively,). The consistency of the T_C (~331 K) across the composite composition indicates minimal or no structural intercalation between the manganite and titanate phase.

At this point, to confirm the FM nature of the samples and to estimate the effective paramagnetic moment, the high-temperature susceptibility was fitted to the Curie–Wiess law. The Curie–Weiss (CW) law for composite system containing diamagnetic components is given by $\chi = \chi_0 + \frac{C}{T-\theta_p}$. Here, $C = \frac{N_A \mu_{eff}{}^2}{3k_B}$ is the Curie constant (N_A is the Avogadro's number, k_B is the Boltzmann constant, and μ_{eff} is the effective magnetic moment), θ_p is the Weiss constant, and χ_0 is the temperature-independent term of the susceptibility. The term χ_0 is a sum of the negative (diamagnetic) Larmor core susceptibility, the positive Pauli paramagnetic spin susceptibility of conduction electrons, the negative Landau susceptibility due to the orbital circulation of

conduction electrons in the magnetic field, and the positive Van Vleck paramagnetic susceptibility, where all four contributions are of the same order of magnitude. The experimental determination of χ_0 was performed by plotting χ *versus* $\frac{1}{T}$, and χ_0 is estimated by extrapolating to the high-temperature limit $\left(\frac{1}{T} \rightarrow 0\right)$, where the contribution of $\frac{C}{T-\theta_p}$ becomes negligible.[158,159] Alternatively, a nonlinear fit of the high-temperature susceptibility data to the CW law can yield the parameters χ_0, C and θ_p. Furthermore, $\frac{1}{\chi-\chi_0}$ *versus* T is plotted to determine C and θ_p, resulting in a linear fit. Conventional CW analysis is adopted for BL100, as it is soft ferromagnet and temperature-independent contributions to the χ are negligible. BL0 was not fitted due to a strong diamagnetic signal above T_f. The Curie constant obtained from the linear fit of ${\chi-\chi_0}^{-1}$ or from nonlinear curve fitting, where χ in the units of emu mol^{-1} would give μ_{eff}^{exp} through $\sqrt{8\times C}\mu_B$. The theoretical value of μ_{eff} (μ_{eff}^{th}) is obtained using the expression $\mu_{eff}^{th}=\sqrt{0.67\times(\mu_{eff}{}^2)_{Mn^{3+}}+0.33\times(\mu_{eff}{}^2)_{Mn^{4+}}}$, where $\mu_{eff}(Mn^{3+})$ = $4.9\mu_B$ and $\mu_{eff}(Mn^{3+})$ = $3.87\mu_B$. In this investigation, for a charge ratio of 67 : 33, μ_{eff}^{th} = $4.59\mu_B$. The values of χ_0, C, θ_p and μ_{eff} obtained from the fit alongside the T_C and μ_{eff}^{th} are tabulated in Table 5.

In the present case, the positive value of χ_0 perhaps indicates Van Vleck paramagnetic susceptibility, possibly due to the low-lying excited states of Mn^{3+}. It is found to increase with an increase in BL100 component, indicating its dependence on the population of Mn3+.[160] The positive value of θ_P indicates the existence of FM interactions in the samples, which confirms a PM to FM second-order phase transition. The higher value of μ_{eff}^{exp} compared to μ_{eff}^{th} in BL100 indicates that the sample does not have the expected 67 : 33 charge ratio; rather, there is a larger population of higher-moment species of Mn. This higher magnetic moment can come from an unexpectedly larger population of Mn^{3+} and Mn^{2+}. In the high spin state, the spin-only magnetic moment of Mn ions increases with decreasing oxidation state, *i.e.* $\mu_{Mn^{2+}} > \mu_{Mn^{3+}} > \mu_{Mn^{4+}}$, which are $5.92\mu_B$, $4.9\mu_B$, and $3.87\mu_B$, respectively. Studies on $La_{1-x}Sr_xMnO_3$ through electron spin resonance and magnetic measurements have shown that perovskite manganites are inhomogeneous ferromagnet, which means FM clusters are found even above T_C.[161,162] As a result, it leads to a larger value of μ_{eff}^{exp} compared to μ_{eff}^{th}. However, in BL100, $\theta_p = T_C$, which means it perfectly follows the classical CW law and hence is a homogenous ferromagnet. Spinal Mn_3O_4 also contains Mn^{2+} at tetrahedral sites (and two Mn^{3+} at octahedral sites); however, the percentage of detectable Mn_3O_4 is too low to consider it to be a source of excess Mn^{2+} and Mn^{3+}. This means that the only possibility of having higher μ_{eff}^{exp} compared to μ_{eff}^{th} is the presence higher concentration of Mn^{3+} and Mn^{2+} in the perovskite lattice. Structural investigations have already been suggested the presence of Mn^{2+} in BL100, in both rhombohedral and monoclinic phases. Here, the CW analysis confirms the presence of Mn^{2+} in BL100 and supports the existence of multiple double-exchange mechanisms due to the presence of Mn antisite defects, where Mn^{2+} occupies La and Na sites in the perovskite lattice. Suppose that one considers the magnetic contribution in the composites comes only from the manganite phase, the magnetic phase fraction can be estimated from the computed magnetic moment. The phase fraction was found to be 22%, 34%, 40% and 50% for BL10, BL20, BL30 and BL50, respectively. One can notice that in BL50, the magnetic phase fraction is exactly nominal, but the structural phase fraction is found to be 10% less than the nominal phase fraction. It is quite interesting to note that the structural phase fraction is almost nominal in BL10, BL20 and BL30, but the magnetic phase fraction exceeds 10%. This confirms the magnetic nature of BL0, and in the composite, the contribution to the magnetic moment not only comes from the manganite phase but also from the titanate phase. To support the claim, magnetic isotherms were recorded for all the samples at 5 K and at 300 K.

Fig. 15 depicts the magnetic isotherms of BL0 recorded at 5 K and 300 K. Both hysteresis loops show a negative linear slope in the evolution of M for the positive field increment and *vice versa*. This occurs at very high fields (40 kOe) for the 5 K isotherm and just at 1 kOe in the case of 300 K isotherm. However, at low fields, the M variation is abrupt, showing a sudden positive increase with a change in H. This behaviour is evidence of FM spin clusters embedded in a diamagnetic background. To extract the FM magnetization from the diamagnetic response, a linear fit ($M = \chi H$, $\chi < 0$) was applied to the high-field M–H data at 5 K (shaded region, A). The diamagnetic susceptibility was found to be -1.24×10^{-7} emu g^{-1} Oe^{-1} for the 5 K isotherm. Using this value, the corrected M was obtained by subtracting e $\chi_{dia}H$ form M_{obs}. The calculated values of M_s, M_r and H_c are 0.017 emu g^{-1}, 3.30×10^{-4} emu g^{-1} and 100.97 Oe, respectively. Quite differently, the experimental data of 300 K was fitted using

Table 5 Temperature-independent susceptibility χ_0, Curie constant C, Wiess constant θ_p, effective paramagnetic moment μ_{eff}, estimated both experimentally and theoretically, and the Curie temperature T_C

	Nonlinear curve fitting, $\chi=\chi_0+\frac{C}{T-\theta_p}$				Linear fit to ${\chi-\chi_0}^{-1}$				
Sample code	$\chi_0 \times 10^{-6}$ emu g^{-1} Oe^{-1}	C (emu mol^{-1} K)	θ_p (K)	μ_{eff}^{exp} (μ_B)	C (emu mol^{-1} K)	θ_p (K)	μ_{eff}^{exp} (μ_B)	T_C (K)	μ_{eff}^{th} (μ_B)
BL10	1.57	0.187	317.0	1.22	0.187	316.9	1.22	330.8	4.59
BL20	2.12	0.439	318.7	1.87	0.439	381.8	1.87	331.6	4.59
BL30	3.78	0.607	317.2	2.20	0.606	317.3	2.20	331.8	4.59
BL50	7.66	0.964	313.3	2.78	0.965	313.3	2.78	331.6	4.59
BL100	—	—	—	—	3.85	330.2	5.55	331.6	4.59

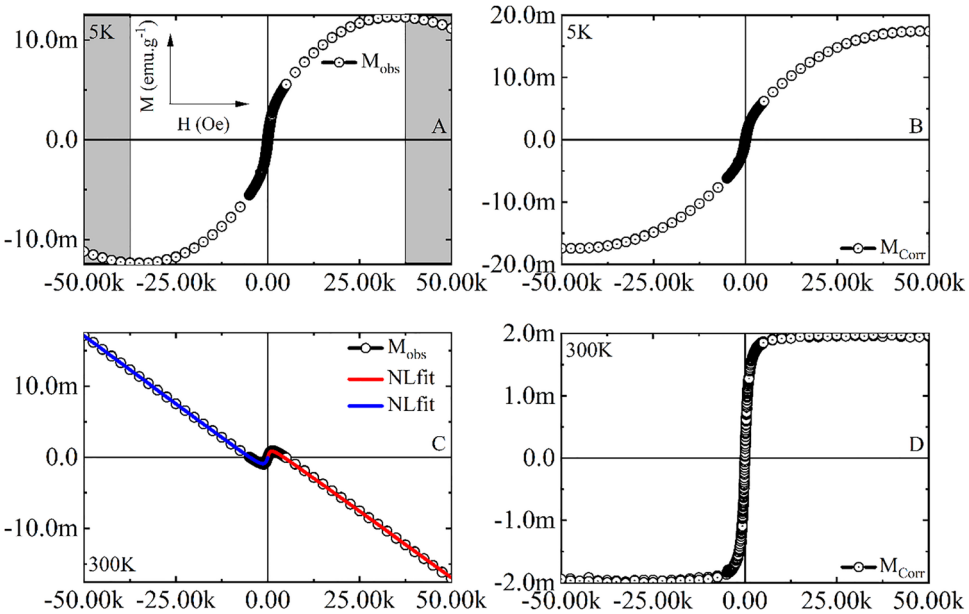

Fig. 15 Hysteresis loops of magnetization *versus* applied field intensity of BL0 record at 5 K (A) and 300 K (C) for a field cycle of 0 ± 50 kOe. Each isotherm is corrected for high-field diamagnetic contributions ((B) and (D), respectively) using linear and nonlinear fitting.

the equation $\frac{2}{\pi}M_s \tan^{-1}\left[\frac{(H \pm H_c)}{H_c} \times \tan\left(\frac{\pi}{2}\frac{M_r}{M_s}\right)\right] + \chi H$.[163,164] Here, M_s stands for the saturation magnetization, H_c is the intrinsic coercivity, and M_r is the remanent magnetization. The first term in the equation represents the usual function for ferromagnetic hysteresis curve, and χH stands for the linear diamagnetic or paramagnetic contribution to the M–H loops. The obtained values of M_s, M_r, H_c and χ_{dia} are 0.002 emu g^{-1}, 2.33 × 10^{-5} emu g^{-1}, 11.61 Oe, −3.73 × 10^{-7} emu g^{-1} Oe^{-1}, respectively. Considering the χ_{dia}, the M was corrected and is shown in Fig. 15D. One can notice here that the hysteresis loop at 5 K is S-shaped with finite remanence and coercivity, whereas the hysteresis loop at 300 K shows soft ferromagnetic nature with complete saturation and squeezing toward the $H = 0$, indicating a bi-magnetic nature. The M_s at 5 K is an order of magnitude higher than at 300 K. Such an S-shaped loop, which is only observed at low temperatures (below T_f), is characteristic of both metallic and non-metallic spin glasses and indicates the presence of short-range magnetic correlation in the system at low temperatures.[165–167] This observation supports the claim of a CG/SpG nature in BL0 at temperatures below 127 K. It is interesting to see that BL0 displays room-temperature ferromagnetism. As discussed in the previous section, FM at RT is generally induced by Ti vacancies; however, a Cu-doped TiO_2 shows FM at room temperature due to oxygen vacancies near the impurity, such as Cu.[163] Therefore, it is believed that FM in insulating oxide perovskite can be realized by cationic vacancies and anionic vacancies, which results from spin polarization of itinerant holes at ligand orbitals and spin polarization of itinerant electrons at B-site cationic orbitals, as discussed earlier.

Fig. 16 shows the M–H hysteresis loops of BL100 recorded at 5 K (A) and 300 K (B). Before one would analyse the magnetic field dependence of magnetization, it is essential to account for the demagnetization effect in randomly shaped magnetic specimens subjected to an external magnetic field (H_{ext}). Due to the random dimensionality, the internal field experience by the specimen (H_{int}) is quite different from that of H_{ext}. The demagnetization correction is expected to reveal the intrinsic field experienced by the ferromagnetic material due to the dimensional variations. Once the demagnetization corrections are applied, the magnetic field axis can be defined as $H_{int} = H_{ext} - N_d M$, where N_d is the demagnetizing factor, and M is the corresponding magnetization.[168] For a multidomain grain system, N_d can be obtained from the initial knowledge of H_c and M_r, the initial susceptibility χ or the initial inverse slope of the M–H curve. The approximate value of N_d is given by $N_d \approx \frac{H_c}{M_r} = \frac{1}{\chi_{ini}} = \left(\frac{dM}{dH}\right)_{ini}^{-1}$.[169] Furthermore, the values of H_c, M_r and M_s shed light on the nature of FM in the sample. A rough estimate of the saturation magnetization, M_s, can be obtained from Arrott plots, where extrapolation of the linear portion of the M^2 *versus* $\frac{H}{M}$ curve to the M^2 axis at higher $\frac{H}{M}$ values yields M_s.[170] The obtained values of M_s, H_c and M_r are summarized in Table 6. The sudden increase in M at low H, the small magnitude H_c and M_r, the saturation of M at high H and the positive slope of Arrott plots (not shown here) signify a second-order phase transition (SOPT) and the soft ferromagnetic nature of all the samples below the Curie point (except for BL0).[171] It is interesting to note that M_r, H_c and M_s in the composite are found to slightly increase with increasing ferromagnetic BL100 content (however, H_c in BL0 is the highest among all samples, 101 Oe).

The M_s value observed in BL50 is the highest of all composites (36.4 emu g^{-1}), which is 39% of BL100. Conversely, the coercivity of the composites and BL0 is higher than that of

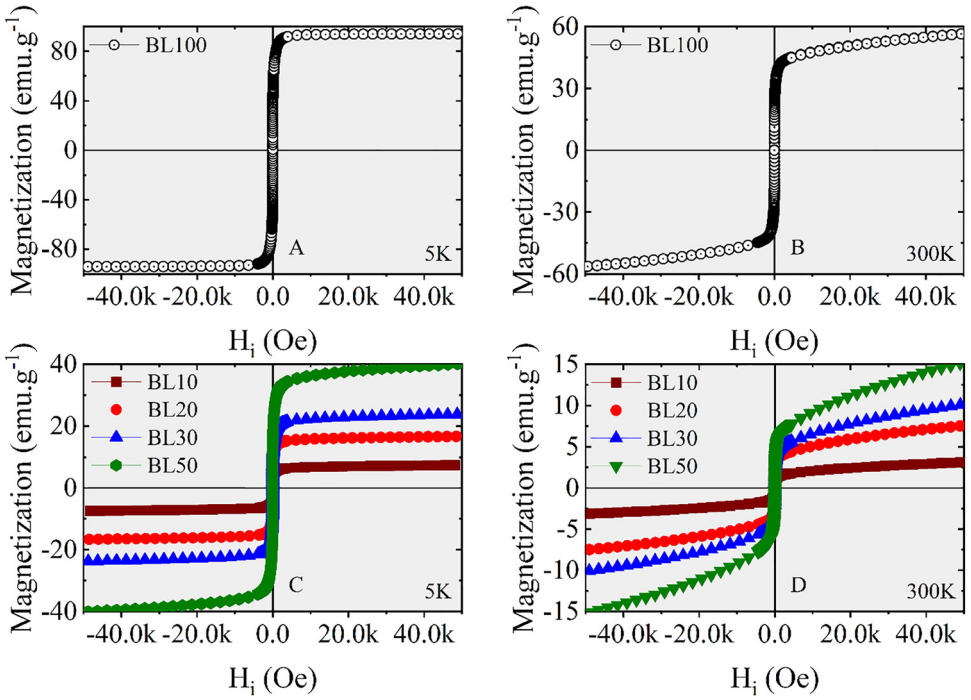

Fig. 16 Hysteresis loops of magnetization *versus* internal field intensity of BL100 record at 5 K (A) and 300 K (B) for a field cycle of 0 ± 50 kOe. (C) and (D) Magnetic isotherms of the composites under similar conditions as BL100. Each isotherm has been corrected for demagnetization effects.

Table 6 Retentivity (M_r), coercivity (H_c), demagnetization factor (N_d), saturation magnetization (M_S), magnetocrystalline anisotropy constant (K_1), and anisotropy field (H_a) obtained from hysteresis loop analysis, Arrott plots and LAS

			N_d			M_s emu g^{-1}				
Specimen	M_r emu g^{-1}	H_c Oe	$\frac{H_c}{M_r}$	$\frac{1}{\chi_{ini}}$	$\left(\frac{dH}{dM}\right)_{ini}$	M^2 *vs.* $\frac{H}{M}$	LAS	$K_1 \times 10^3$ erg g^{-1}	H_a Oe	$\frac{M_r}{M_s}$
BL0	0.00033	101.0	—	—	—	0.02	—	—		—
BL10	0.2	35.8	215.7	250.0	238.6	6.8	7.1	3.5	977.3	0.03
BL20	0.4	31.0	76.2	100.0	89.0	15.9	16.5	12.0	1451.1	0.03
BL30	0.7	31.6	44.8	62.5	53.3	22.4	23.3	18.4	1573.7	0.03
BL50	2.0	47.7	23.6	35.7	30.2	36.4	38.3	18.7	976.7	0.05
BL100	1.3	14.2	10.8	11.9	11.5	93.7	96.4	89.3	1851.6	0.01

BL100, and the retentivity of BL50 is higher than that of BL100. This clearly indicates that a robust FM network is established in the composite with obvious broken FM network leading to dilution. The higher H_c in the composites indicates the anisotropy in the sample. To understand the effect of magnetic anisotropy, all 5 K *M*–*H* curves in the first quadrant of the hysteresis loop were fitted using the law of approach to ferromagnetic saturation (LAS) to extract the magnetocrystalline anisotropy (MCA, K_1), anisotropy field (H_a) and M_s.

There are several forms of the LAS,[172] depending on the type of FM material, composition and particle size. Its efficacy is proven mainly in single-domain, noninteracting particle systems. In the case of magnetic materials with a multi-domain structure, the process of magnetization varies across different regions of the magnetization curve. The lower-field region, below saturation, consists of a mixture of domain wall motion and domain rotation. As *M* approaches saturation, the magnetization process is mainly dominated by domain rotation. If the high-field region is carefully selected, LAS can still be applied to multidomain structures to extract M_s, (K_1) and (H_a). The fit is shown in Fig. 17. The region where domain rotation is dominant is approximately above $4\pi M_s$ of *H*; therefore, the fit is applied to this region of the *M*–*H* curve or sufficiently above the Rayleigh region. Some authors report that the LAS works only if the following conditions are met: $H \gg H_c$ and $T \ll \frac{T_C}{2}$.[173] In the present case, the LAS is defined as $M = M_s\left(1 - \frac{a}{\sqrt{H}} - \frac{b}{H^2}\right) + \chi_{hf}H$.[174,175] Here, the parameter *a* is attributable to various structural defects and intrinsic fluctuations; hence, $\frac{a}{\sqrt{H}}$ represents the contribution from random anisotropy. The parameter $b = \frac{8}{105}\left(\frac{K_1}{M_s}\right)^2 = \frac{H_a^2}{15}$ is related to the uniaxial magnetocrystalline anisotropy constant,

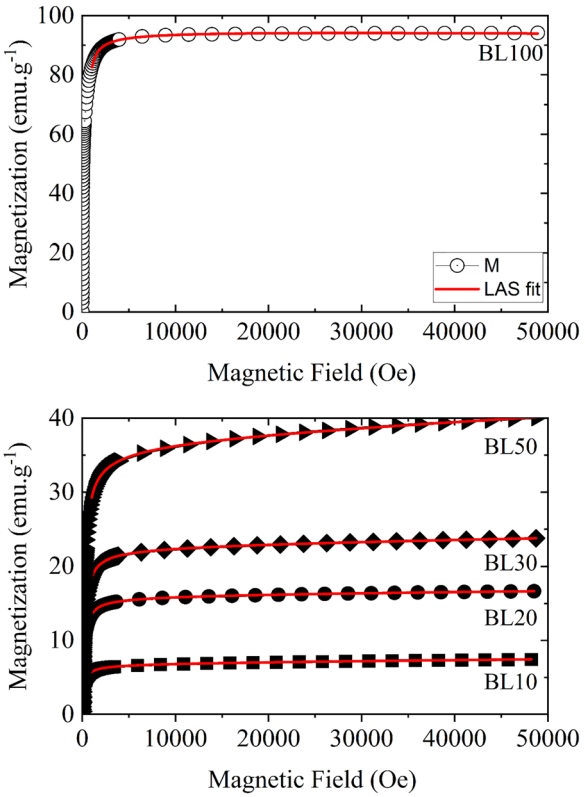

Fig. 17 5 K magnetization data in the first quadrant of the hysteresis loop under the governance of law of approach to ferromagnetic saturation.

K_1, and anisotropy field, H_a. χ_{hf}, corresponds to the high-field susceptibility. The fit is applied only to the 5 K *M–H* curve in the first quadrant, as the 300 K *M–H* curves lack approach to saturation. The obtained values of M_s, K_1 and H_a are tabulated in Table 6. The close agreement between the M_s values obtained from the two different approaches indicate the validity of the fitting model. The K_1 values are significantly lower in the composites compared to BL100. Interestingly, H_a shows a local minimum at BL50, hinting a correlation between the structural and magnetic phase fractions discussed earlier. In other words, the magnetism in the composites strictly follows the magnetic phase fraction, *i.e.* the percentage of $La_{0.835}Na_{0.165}MnO_3$. M_s increases with BL100 content and so is the M_r. The squareness ratio, defineas $\frac{M_r}{M_s}$, is less than 0.5, which indicates that the samples possess a multidomain structure and that BL100 particles are randomly distributed in the composites, free from grain interaction effects.[176] Furthermore, M_s is correlated to the Bohr magneton (μB per f.u.), and it can be determined using the following equation: $\mu_B \text{ f.u.}^{-1} = \frac{\text{moelecular weight} \times M_s}{5585}$.[177] The value changes from 0.3μB per f.u. for BL0 to 3.7μB per f.u. for BL100. The continuous increase in M_s is obviously due to the incorporation of soft ferromagnetic $La_{0.835}Na_{0.165}MnO_3$. However, the sudden increase and saturation behaviour of K_1 and H_a require attention. K_1 is a measure of energy per unit volume required to move the magnetization vector from the easy axis to the hard axis. As a result, the small fraction of BL100 in BL10 weakens magnetic interactions. This means the energy required to move the *M* vector per unit volume is low. The saturation behaviour of K_1 in BL30 and BL50 reflects a similar magnetic concentration in the composites due to non-stochiometric substitution. In manganites, Mn^{3+} is a source of MCA, which means a smaller fraction of Mn^{3+} in the composites is responsible for the lower values of K_1. To put it in other words, the dilution of $La_{0.835}Na_{0.165}MnO_3$ in a nonmagnetic matrix results in the averaging of magnetic anisotropies. Finally, magnetic materials with strong MCA offer superior properties for applications in magnetoresistive random-access memories (MRAMs) and multifunctional spintronic devices.[178]

3.4 Ferroelectric characters

Reported temperature-dependent dielectric measurements on $BaTiO_3$ showed that below 120 °C, cubic $BaTiO_3$ spontaneously changes to tetragonal crystals and becomes polarized along the tetrad axis or cube face direction [001] ($P_s \approx$ 14–16 μC cm^{-2}). Interestingly, it further shows orthorhombic and rhombohedral phase transitions at −5 °C and −90 °C, respectively, having slightly lower polarization values (∼12 μC cm^{-2} to 8 μC cm^{-2}) along the cube-edge direction [110] and the cube-diagonal direction [111]. Ferroelectricity in $BaTiO_3$ is a consequence of masking of short-range Coulombic repulsion between Ti^{4+} and O^{2-}. Ferroelectricity occurs when the long-range force due to dipole–dipole interactions overcomes the short-range Coulombic repulsion. This allows nearly permanent movement of Ti^{4+} from the centrosymmetric position and O^{2-} from the face centre position such that some of the Ti–O bonds can be shorter than the others, and the effective charges on Ti and O can significantly deviate from 4+ and 2−. The covalent hybridization between Ti and the O ions helps weakens the short-range Coulombic repulsion.[179] Knowing the origin of FE in $BaTiO_3$ to understand the possible FE in the composites, BL10 is selected for recording the *P–E* hysteresis loop.

Fig. 18(1) depicts the RT polarization (*P*) *versus* electric field (*E*) hysteresis loops (*P–E* loops) of BL10 under E_0 magnitude of 250 V (1.63 kV cm^{-1}), 500 V (3.27 kV cm^{-1}) and 1000 V (6.54 kV cm^{-1}). Note that it was possible to obtain *P–E* loops only up to 1000 V, post which there was a dielectric breakdown. The measurements were carried out under unpoled conditions. At first glance, one can see that loops lack saturation polarization. Many reports call such behaviour necessarily as lossy or leaky ferroelectricity, but not sufficiently, because in a real scenario, such behaviour results from the combined effect of a linear capacitor and a parallel resistor. Here, the hysteresis features shall appear with increasing conductivity, but neither saturated polarization nor switching current can be observed.[180] Thus, BL10 is lossy or leaky but not ferroelectric. To confirm the said assertion, the influence of the electric field on the *P–E* loop area (*A*) and leakage current density (*J*) was considered for evidential analysis. When comparing *P–E* loops at different AC field amplitudes (E_0), the area under the loop is a key parameter. The hysteresis area is strongly associated with the nucleation and growth of the domain, domain wall motion and domain

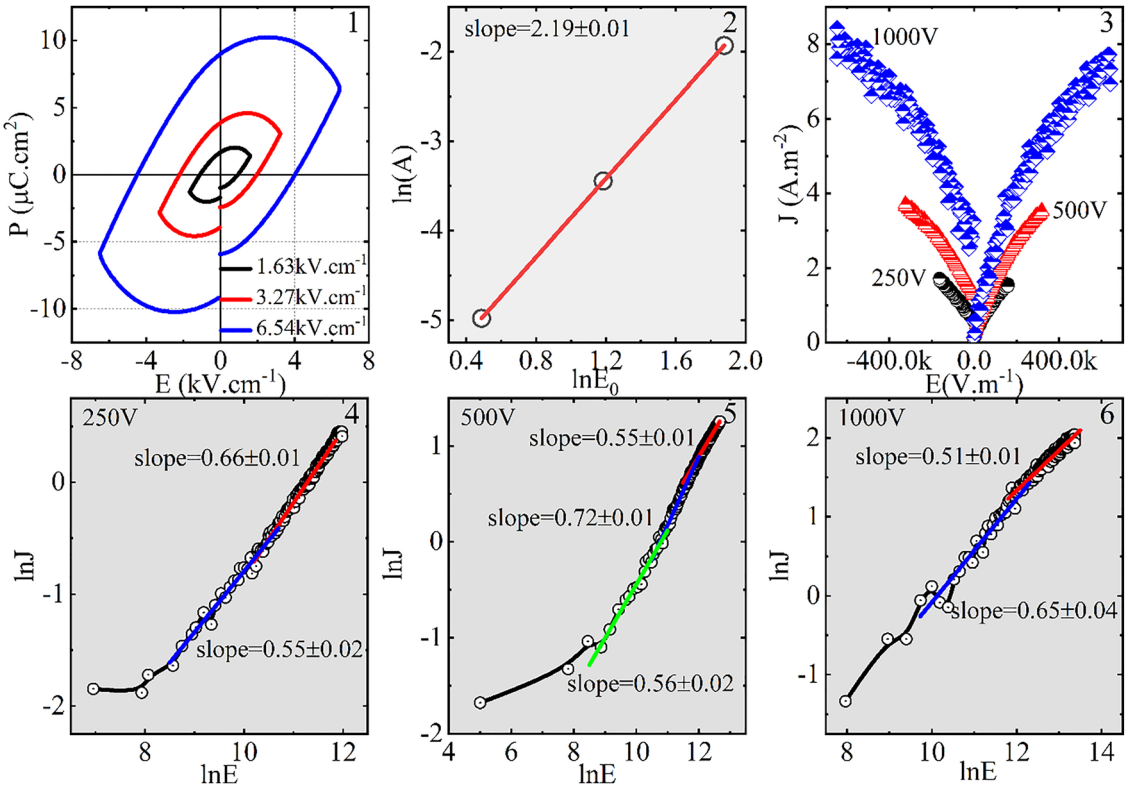

Fig. 18 (1) Plot of electric polarization *versus* electric field under the bias voltages of 250 V (1.63 kV cm^{-1}), 500 V (3.27 kV cm^{-1}) and 1000 V (6.54 kV cm^{-1}). (2) Log–log plot of the area under the loop *versus* E_0. (3). Variation in current density with applied potential. (4)–(6) Log–log plots of current density *versus* *E* to understand the various conduction mechanisms that drive current in the BL10 specimen.

switching.[181] The areas under the loops were obtained by integration, and to investigate the dependence of A on E_0, the graph of the $\ln A$ *versus* $\ln E_0$ was plotted (Fig. 18(2)). The variation follows a linear trend and can be modelled as $\ln A = \beta \ln E_0 + b$. Here, β is the slope of the straight line. The β for BL10 is 2.19 ± 0.01. If BL10 was to be a ferroelectric, it would show three distinct regions in the $\ln A$ *versus* $\ln E_0$ plot. The first linear region signifies the domain wall motion. The slope in the first region would be high, indicating that domains easily follow the external electric field. The second region would be a nonlinear region, which is associated with abrupt changes in the polarization value at a given E_0. Here, the domain switching mechanism leads to a sudden enhancement in the values of current and polarization. The third region would again a linear region, which denotes the complete saturation, and almost all the dipoles here are orientated along the direction of the applied electric field. This region typically exhibits a smaller slope compared to the first region. The case of BL10 reflects only the first linear region due to its stability only at low amplitudes of the AC field. The earlier reports state that even in leaky ferroelectrics, the β of the first linear region is not less than 3. The low β value in BL10 indicates that domain wall motion is restricted. This restriction does not allow nucleation and growth necessary for eventual saturation. This finding demands attention towards the microstructure of BL10 compared to the parent BL0. An ideal ferroelectric material is, by default, insulating in nature. The lossy nature in any ferroelectric is then directly related to the increase in its conductivity. Studying the variation of J in a leaky ferroelectric becomes apparent because it enables one to understand the interfacial and internal variation of currents (displacement, leakage and capacitive). Fig. 18(3) shows leakage current density *versus* electric field curves (J–E curves) of BL10 under various E_0 magnitudes. The curves are symmetric with respect to positive and negative field sweeps. The J is found to be 1.72 A m^{-2} at E_0 of 1.63 kV cm^{-1} and grows to 8.42 A m^{-2} at 6.54 kV cm^{-1}. These values of current density are typically large compared to $BaTiO_3$ films, in which the corresponding values are found to be 0.005 A m^{-2} even at a field intensity of 100 kV cm^{-1}.[182–184] The variation of J is such that there exists a gradual change when going from low AC field to a higher, with a tendency to saturate at high fields. The change in J with an increase in the electric field prompts the presence of a specific conduction mechanism in the specimen. There is an array of mechanisms that decide the variation of J with respect to E in oxides. The notable ones are Ohmic conduction, space-charge-limited conduction (SCLC), Poole–Frenkle emission (PFE) and field-assisted hopping (FAH) conduction.[185–188] Ohmic conduction is an interface-limited conduction mechanism, whereas SCLC, PFE and FAH are bulk-limited conduction mechanisms. The existence of interface-limited conduction mechanisms arises from the difference in Fermi levels between the metal (electrode) and the insulator or

semiconductor (BL10). This energy difference creates a potential barrier between the metal and the insulator, which charges must overcome. Essentially, this barrier is Schottky in nature, thus, the current density at low fields takes the form $J = A^* T^2 \exp\left(\frac{\Delta\phi - \phi_B}{k_B T}\right)$. Here, $\Delta\phi = \sqrt{\frac{qE}{4\pi\varepsilon_0\varepsilon_r}}$ is the field-dependent term, A^* is the effective Richardson constant, T is the temperature, ϕ_B is the Schottky barrier height, k_B is the Boltzmann constant, q is the electron charge, E is the applied electric field, ε_0 is the permittivity of free space, and ε_r is the relative dielectric constant of the ferroelectric material. Suppose the energy different between the electrode and the FE medium is low, the interface may behave ohmically, and the current density may take the form $J = e\mu n_e E$, where e is the electronic charge, μ is the carrier mobility, n_e is the carrier concentration, and E is the applied electric field. Bulk-limited SCLC arises from a current-blocking space charge. The existence of SC in an insulator under an electric field is a salient feature of FEs. It happens when charges are injected into the insulator from the electrode at a rate faster than they can travel through it. The current density in such case is given by $J = \frac{9\mu\varepsilon_0\varepsilon_r V^2}{8t^3}$. Here, t is the thickness of the specimen. PFE essentially dominates the high-field regime of the J–E characteristics, where conduction involves consecutive hopping of charges between defect trap centres. The release of trapped charges can happen thermally as well as through the influence of a high field. The expression for current density is given by $J = C^* E \exp\left(\frac{\Delta\phi - \phi_t}{k_B T}\right)$, where $\Delta\phi = \sqrt{\frac{qE}{\pi\varepsilon_0\varepsilon_r}}$, and C and ϕ_t are a constant and the barrier height, respectively. On the other hand, according to FAH conduction mechanism, if the thermal energy is insufficient, charge carriers trapped in defect states become incapable of overcoming the barrier height between trap sites. As a result, if the field is essentially large, charge migration between trap centres primarily occurs by the process of tunnelling. It should be noted at this point that the ohmic conduction and SCLC mechanisms follow a power-law behaviour such that $J \propto E^n$, where n is the power-law exponent obtained from the slope of a log–log plot of J *versus* E. If $n \sim 1$, the underlying conduction is ohmic and if $n \sim 2$, the conduction mechanism is SCLC. On the other hand, Schottky, PFE and FAH conduction mechanisms follow semi-log nature $\log_e(J)$ *versus* $E^{1/2}$, $\log_e(J/E)$ *versus* $E^{1/2}$ and $\log_e(J)$ *versus* E, respectively. Fig. 18(4)–(6) shows the log–log plots of J–E curves for positive field sweeps up to E_0. Essentially, the slope is near unity in the range 0.55 to 0.72, indicating that ohmic conduction dominates in BL10. An interesting observation in the log–log plots is the trend of the slope. First and foremost, there is no single linear region in the entire logarithmic J–E variation, but multiple linear regions exist. Second, the slope increases with increasing AC field at a 250 V amplitude, whereas the trend is reversed in 1000 V amplitude. Necessarily, it prompts further investigation into the possible Schottky nature of conduction in the material. Consequently, $\log_e(J)$ *versus* $E^{1/2}$ was plotted and found that the plot for 250 V field amplitude indeed shows linear behaviour, indicating the Schottky nature of the electrode–sample interface. This means that the specimen at low polarizing fields is insulating in nature; however, at high polarizing fields, conductive channels are activated, which turns the sample to ohmic conductor rather than an insulating ferroelectric. The overall conduction mechanism in BL10 can be considered as grain boundary-limited conduction (GBLC). GBLC is identified by ohmic conduction, and s slope less than 1 indicates band bending with increasing field. Thus, the deviation from typical ferroelectric behaviour, including the decline of P_r and P_s, lossy loops and high leakage current density, collectively indicate a degradation in ferroelectric properties in the composites. These changes are a consequence of the presence of a non-ferroelectric phase, which restricts ferroelectric domain wall motion. The closer examination of the microstructural properties of BL10 clarifies this behavior. FESEM micrographs of BL10 show a scattered distribution of $BaTiO_3$ grains surrounded by fine manganite grains. LNMO manganite is a metallic ferromagnet at RT. In a broader sense, even though there is no continuous grain–grain boundary assembly, LNMO can be considered as a conducting medium around the $BaTiO_3$ grains at the boundaries. Thus, if the amplitude of the AC field is low, the electrode–$BaTiO_3$ and LNMO–$BaTiO_3$ interfaces can be considered as Schottky or depletion junctions, which is why band bending happens. However, as the amplitude of the electric field increases, the breakdown of leakage current occurs before it could enter SCLC, turning the mechanism into ohmic conduction. Thereby, even though FE polarization is not achieved, the leaky FE behaviour at low E_0 is essentially an attractive character in theses marginally substituted composites. It can be exploited in spintronics, non-volatile memory, neuromorphic computing and artificial synapses, low-energy nanoelectronics and logic devices, and magnetoelectric sensors.

4. Conclusion

In conclusion, the synthesis of multiferroic $(1 - x)BaTiO_3$:(x)-$La_{0.835}Na_{0.165}MnO_3$ composite system (x = 0, 0.1, 0.2, 0.3, 0.5 and 1) was attempted using the conventional solid-state reaction method at a low sintering temperature (950 °C) and short soaking duration (4 h). The result is nonstoichiometric Ti-deficient $BaTiO_{3-\Delta}$ and A-site cation-deficient $La_{0.835}Na_{0.165}MnO_{3-\Delta}$. Such nonequilibrium states are the result of the termination of solubility of precursors under the given A-site/B-site cationic ratio, oxygen partial pressure and annealing temperature. The nonequilibrium $BaTiO_3$ phases are Ba_2TiO_4, $BaTi_4O_9$ and $BaCO_3$, whereas for $La_{0.835}Na_{0.165}MnO_3$, they are $La_{0.9}MnO_3$-like phase, La_2O_3 and Mn_3O_4. These impurities, once formed, are stable throughout the composite composition, giving them vivid optical, magnetic and electric characteristics. The microstructures of the prepared $BaTiO_3$ and $La_{0.835}Na_{0.165}MnO_3$ are dramatically different due to their initial processing conditions. $BaTiO_3$ has large grains due to elevated sintering temperature (1300 °C), whereas $La_{0.835}Na_{0.165}MnO_3$ grains are significantly small with loosely bound grain distribution. The combination of the distinct optical characteristics of two different perovskite materials, one being the UV absorber ($BaTiO_3$) and the other being the UV-visible absorber,

has created excellent visible photoactive materials (x = 10, 20, and 30) with a band gap tunable from 3.23 eV to 2.95 eV at x = 30. The samples possess high Urbach energy due to a large population of defect states established in the forbidden gap of the parent $BaTiO_3$. The composites can thus be exploited for water splitting and the degradation of water pollutants, employing a large light-harvesting window. An interesting outcome of the exercise is the induction of ferromagnetism in insulating, nonmagnetic $BaTiO_3$ at room temperature. Ti deficiency renders ferromagnetism in $BaTiO_3$ through spin polarization of itinerant holes at O 2p orbitals and spin polarization of itinerant electrons in Ti t_{2g} orbitals. The random distribution of clusters of nonmagnetic stochiometric $BaTiO_3$ containing Ti^{4+} and weakly ferromagnetic, nonstoichiometric $BaTiO_3$ and its nonequilibrium phases containing Ti^{3+} of different sizes brings out magnetic frustration, perhaps displaying a cluster glass ground state. However, a deeper analysis is needed to understand the dynamics at low temperatures. The A-site cationic-deficient $La_{0.835}Na_{0.165}MnO_3$, along with the $La_{0.9}MnO_3$, displays excellent magnetic sensitivity. The composites possess a prominent ferromagnetic ground state with significant magnetocrystalline anisotropy. The intention of inducing ferromagnetism in ferroelectric $BaTiO_3$ through composites is fulfilled; however, failure in establishing multiferroicity is faced due to the generation of large free carriers in the insulating ferroelectric $BaTiO_3$ matrix. The composites are no longer ferroelectric insulators, but they have translated into an ohmic conductor.

Author contributions

LDM: conceptualization, data curation, formal analysis, investigation, methodology, visualization, writing – original draft. EKH: investigation, validation, writing – review & editing. MDD: funding acquisition, project administration, supervision.

Conflicts of interest

The authors declare that there are no competing interests to declare.

Data availability

Supplementary information (SI) is available. See DOI: https://doi.org/10.1039/d5ma01177a.

Due to the large amount of raw data and related calculation in this paper, it is not possible to upload all the data to the public network, so we will disclose the raw data and relevant calculation involved in the research process on request.

Acknowledgements

The Manipal Academy of Higher Education and UGC DAE Consortium for scientific research (UDCSR/MUM/CD/CRS-M-240/2017/1008) are acknowledged for their support in carrying out the present research. The authors are thankful to Dr Mukul Gupta (UGC DAE CSR, Indore) for XRD measurements, Dr Sujay Chakravarty (UGC DAE CSR, Kalpakkam Node) for magnetization measurements. Mendonca L. D. is thankful to Patricia Mendonca, Leslie David Mendonca and Stella Ronny Lewis for their invaluable cooperation throughout the work and during the preparation of the manuscript. Pramod R. Nadig, Vignesh K. R. Kavya D. M. and Srujana B. S. are acknowledged for fruitful discussions on structuring the entire manuscript over the course of time.

References

1 M. Fiebig, T. Lottermoser, D. Meier and M. Trassin, The Evolution of Multiferroics, *Nat. Rev. Mater.*, 2016, **1**(8), 16046, DOI: 10.1038/natrevmats.2016.46.
2 Y. Cheng, B. Peng, Z. Hu, Z. Zhou and M. Liu, Recent Development and Status of Magnetoelectric Materials and Devices, *Phys. Lett. A*, 2018, **382**(41), 3018–3025, DOI: 10.1016/j.physleta.2018.07.014.
3 J. Shen, J. Cong, Y. Chai, D. Shang, S. Shen, K. Zhai, Y. Tian and Y. Sun, Nonvolatile Memory Based on Nonlinear Magnetoelectric Effects, *Phys. Rev. Appl.*, 2016, **6**(2), 1–5, DOI: 10.1103/PhysRevApplied.6.021001.
4 Ü. Özgür, Y. Alivov and H. Morkoç, *Microwave Ferrites, Part 2: Passive Components and Electrical Tuning*, 2009, vol. 20, DOI: 10.1007/s10854-009-9924-1.
5 K. F. Wang, J. M. Liu and Z. F. Ren, Multiferroicity: The Coupling between Magnetic and Polarization Orders, *Adv. Phys.*, 2009, **58**(4), 321–448, DOI: 10.1080/00018730902920554.
6 Y. Wang, J. Hu, Y. Lin and C. W. Nan, Multiferroic Magnetoelectric Composite Nanostructures, *NPG Asia Mater.*, 2010, **2**(2), 61–68, DOI: 10.1038/asiamat.2010.32.
7 C. Nayek, K. K. Sahoo and P. Murugavel, Magnetoelectric Effect in La0.7Sr0.3MnO 3-BaTiO3 Core-Shell Nanocomposite, *Mater. Res. Bull.*, 2013, **48**(3), 1308–1311, DOI: 10.1016/j.materresbull.2012.12.043.
8 R. Gao, X. Qin, Q. Zhang, Z. Xu, Z. Wang, C. Fu, G. Chen, X. Deng and W. Cai, Enhancement of Magnetoelectric Properties of (1-x)Mn0.5Zn0.5Fe2O4-XBa0.85Sr0.15Ti0.9Hf0.1O3 Composite Ceramics, *J. Alloys Compd.*, 2019, **795**, 501–512, DOI: 10.1016/j.jallcom.2019.05.013.
9 R. Rianyoi, R. Potong, N. Jaitanong, R. Yimnirun and A. Chaipanich, Dielectric, Ferroelectric and Piezoelectric Properties of 0-3 Barium Titanate-Portland Cement Composites, *Appl. Phys. A: Mater. Sci. Process.*, 2011, **104**(2), 661–666, DOI: 10.1007/s00339-011-6307-2.
10 S. K. Ray, J. Cho and J. Hur, A Critical Review on Strategies for Improving Efficiency of BaTiO3-Based Photocatalysts for Wastewater Treatment, *J. Environ. Manage.*, 2021, **290**, 112679, DOI: 10.1016/j.jenvman.2021.112679.
11 S. Zhang, D. Chen, Z. Liu, M. Ruan and Z. Guo, Novel Strategy for Efficient Water Splitting through Pyro-Electric and Pyro-Photo-Electric Catalysis of BaTiO3 by Using Thermal Resource and Solar Energy, *Appl. Catal., B*, 2021, **284**, 119686, DOI: 10.1016/j.apcatb.2020.119686.
12 Y. Zhang, H. Khanbareh, S. Dunn, C. R. Bowen, H. Gong, N. P. H. Duy and P. T. T. Phuong, High Efficiency Water

Splitting Using Ultrasound Coupled Toa BaTiO3 Nanofluid, *Adv. Sci.*, 2022, **9**(9), 2105248, DOI: 10.1002/advs.202105248.
13 S. Kappadan, T. W. Gebreab, S. Thomas and N. Kalarikkal, Tetragonal BaTiO3 Nanoparticles: An Efficient Photocatalyst for the Degradation of Organic Pollutants, *Mater. Sci. Semicond. Process.*, 2016, **51**, 42–47, DOI: 10.1016/j.mssp.2016.04.019.
14 S. Shankar, O. P. Thakur and M. Jayasimhadri, Strong Enhancement in Structural, Dielectric, Impedance and Magnetoelectric Properties of NdMnO3–BaTiO3 Multiferroic Composites, *Mater. Chem. Phys.*, 2021, **270**, 124856, DOI: 10.1016/j.matchemphys.2021.124856.
15 L. Zhou, Q. Fu, D. Zhou, F. Xue, Y. Tian and L. Hao, Magneto-Electric Coupling Study in Multiferroic La0.7Ba0.3MnO3-BaTiO3 Composite Ceramic at Room Temperature, *Ceram. Int.*, 2015, **41**(2), 2367–2372, DOI: 10.1016/j.ceramint.2014.10.049.
16 S. Baryshnikov, E. Stukova and E. Koroleva, Dielectric Properties of the Ferroelectric Composite (NaNO 2)0.9/(BaTiO3)0.1, *Composites, Part B*, 2014, **66**, 190–193, DOI: 10.1016/j.compositesb.2014.05.005.
17 M. A. Dar, M. W. Sheikh, M. S. Malla and D. Varshney, Rietveld Refined Structural and Room Temperature Vibrational Properties of BaTiO3 Doped La0.67Ba0.33MnO3 Composites, *AIP Conf. Proc.*, 2016, **1731**, 10–13, DOI: 10.1063/1.4948175.
18 P. P. Khirade, S. D. Birajdar, A. V. Raut and K. M. Jadhav, Multiferroic Iron Doped BaTiO3 Nanoceramics Synthesized by Sol-Gel Auto Combustion: Influence of Iron on Physical Properties, *Ceram. Int.*, 2016, **42**(10), 12441–12451, DOI: 10.1016/j.ceramint.2016.05.021.
19 E. L. Nagaev, Colossal-Magnetoresistance Materials: Manganites and Conventional Ferromagnetic Semiconductors, *Phys. Rep.*, 2001, **346**(6), 387–531, DOI: 10.1016/S0370-1573(00)00111-3.
20 A. M. Bolarín-Miró, C. A. Taboada-Moreno, C. A. Cortés-Escobedo, O. Rosales-González, G. Torres-Villaseñor and F. Sánchez-De Jesús, Effect of High-Energy Ball Milling on the Magnetocaloric Properties of La0.7Ca0.2Sr0.1MnO3, *Appl. Phys. A:Mater. Sci. Process.*, 2020, **126**(5), 1–10, DOI: 10.1007/s00339-020-03555-w.
21 L. S. Lakshmi, K. Dörr, K. Nenkov, V. S. Sastry and K. H. Müller, Charge State Modification in Mn Site Substituted CMR Manganites: Strong Deleterious Influence on the Ferromagnetic-Metallic State, *J. Phys.: Condens. Matter*, 2007, **19**(23), 0–22, DOI: 10.1088/0953-8984/19/23/236207.
22 L. P. Gor'kov and V. Z. Kresin, Mixed-Valence Manganites: Fundamentals and Main Properties, *Phys. Rep.*, 2004, **400**(3), 149–208, DOI: 10.1016/j.physrep.2004.08.003.
23 H. Boricha, K. Gadani, K. N. Rathod, V. G. Shrimali, S. Solanki, K. Sagapariya, A. Zankat, D. Dhruv, A. D. Joshi, D. D. Pandya, S. Mukherjee, P. S. Solanki and N. A. Shah, Resistive and Magnetoresistance Behaviors of BiFeO3 Incorporated La0.7Ca0.3MnO3 Composites, *Mater. Chem. Phys.*, 2021, **267**, 124605, DOI: 10.1016/j.matchemphys.2021.124605.
24 A. P. Ramirez, Colossal Magnetoresistance, *J. Phys.:Condens. Matter*, 1997, **9**(39), 8171–8199, DOI: 10.1088/0953-8984/9/39/005.
25 H. Boricha, B. Udeshi, S. Mukherjee, P. S. Solanki and N. A. Shah, Resistivity and Magnetoresistance Behaviors of La0.7Sr0.3MnO3-BiFeO3 Matrix-Particles Composites, *Chem. Phys.*, 2021, **549**, 111277, DOI: 10.1016/j.chemphys.2021.111277.
26 H. Boricha, K. Gadani, K. N. Rathod, V. G. Shrimali, S. Solanki, K. Sagapariya, A. Zankat, D. Dhruv, A. D. Joshi, D. D. Pandya, S. Mukherjee, P. S. Solanki and N. A. Shah, Resistive and Magnetoresistance Behaviors of BiFeO3 Incorporated La0.7Ca0.3MnO3 Composites, *Mater. Chem. Phys.*, 2021, **267**, 124605, DOI: 10.1016/j.matchemphys.2021.124605.
27 S. Das and T. K. Dey, Structural and Magnetocaloric Properties of La1-YNa YMnO3 Compounds Prepared by Microwave Processing, *J. Phys. D: Appl. Phys.*, 2007, **40**(7), 1855–1863, DOI: 10.1088/0022-3727/40/7/003.
28 J. H. Lohr, C. A. López, M. E. Saleta and R. D. Sánchez, Ferromagnetic and Multiferroic Interfaces in Granular Perovskite Composite XLa0.5Sr0.5CoO3-(1-x)BiFeO3, *J. Appl. Phys.*, 2016, **120**(7), 0–9, DOI: 10.1063/1.4960697.
29 S. Bharadwaj, A. Tirupathi, N. Pavan Kumar, S. Pola and Y. Kalyana Lakshmi, Study of Magnetic and Magnetoresistance Behaviour of La0.67Sr0.33MnO3-CoFe2O4 Composites, *J. Magn. Magn. Mater.*, 2020, **513**, 167058, DOI: 10.1016/j.jmmm.2020.167058.
30 I. G. Deac and I. Balasz, Electroresistance, Magnetocapacitance and Magnetotransport Properties of La 0.55Ca 0.45MnO 3/BaTiO 3 Composite, *Mater. Chem. Phys.*, 2012, **136**(2–3), 850–857, DOI: 10.1016/j.matchemphys.2012.08.009.
31 D. Varshney and M. A. Dar, Structural and Magneto-Transport Properties of $(1-x)$La0.67Sr0.33MnO3(LSMO) + (x)BaTiO3(BTO) Composites, *J. Alloys Compd.*, 2015, **619**, 122–130, DOI: 10.1016/j.jallcom.2014.08.219.
32 G. M. Ren, S. L. Yuan, H. G. Guan, X. Xiao, G. Q. Yu, J. H. Miao, Y. Q. Wang and S. Y. Yin, Electrical Transport and Magnetoresistance in La0.67Ca0.33MnO3/BaTiO3 Composites, *Mater. Lett.*, 2007, **61**(3), 767–769, DOI: 10.1016/j.matlet.2006.05.057.
33 P. T. Phong, D. H. Manh, N. V. Dang, L. V. Hong and I. J. Lee, Enhanced Low-Field-Magnetoresistance and Electro-Magnetic Behavior of La 0.7Sr 0.3MnO 3/BaTiO 3 Composites, *Phys. B*, 2012, **407**(18), 3774–3780, DOI: 10.1016/j.physb.2012.05.060.
34 R. S. Devan, S. B. Deshpande and B. K. Chougule, Ferroelectric and Ferromagnetic Properties of (x)BaTiO3+ $(1-x)$Ni0.94Co0.01Cu0.05 Fe2 Composite, *J. Phys. D: Appl. Phys.*, 2007, **40**(7), 1864–1868, DOI: 10.1088/0022-3727/40/7/004.
35 H. D. Megaw, Crystal Structure of Barium Titanate, *Nature*, 1945, **155**(3938), 484–485, DOI: 10.1038/155484b0.
36 R. A. Evarestov and A. V. Bandura, First-Principles Calculations on the Four Phases of BaTiO3, *J. Comput. Chem.*, 2012, **33**(11), 1123–1130, DOI: 10.1002/jcc.22942.
37 W. Zhong, W. Chen, W. Ding, N. Zhang, Y. Du and Q. Yan, Magnetocaloric Properties of Na-Substituted Perovskite-Type Manganese Oxides, *Solid State Commun.*, 1998, **106**(1), 55–58, DOI: 10.1016/S0038-1098(97)10239-3.

38 A. Le Bail, Whole Powder Pattern Decomposition Methods and Applications: A Retrospection, *Powder Diffr.*, 2005, **20**(4), 316–326, DOI: 10.1154/1.2135315.

39 L. D. Mendonca, E. K. Hlil, M. S. Murari and M. D. Daivajna, Rhombohedral-to-Cubic Structural Phase Transition in (LaBi)0.7Ba0.3MnO3 Manganites: An Investigation on the ''Cause and Effect'' and Magneto Caloric Response, *J. Mater. Chem. C*, 2025, **13**(29), 15013–15040, DOI: 10.1039/D5TC00829H.

40 F. A. Khan, M. Arshad, M. Abushad, S. Naseem, H. Ahmed, A. Ansari, V. K. Chakradhary, S. Husain and W. Khan, Polaron Hopping Conduction Mechanism and Magnetic Properties of Pb-Doped LaMnO3, *J. Am. Ceram. Soc.*, 2022, **105**(1), 348–361, DOI: 10.1111/jace.18061.

41 G. Dhir, P. Uniyal and N. K. Verma, Tactics of Particle Size for Enhanced Multiferroic Properties in Nanoscale Ca-Doped BiFeO3, *Phys. Status Solidi C*, 2017, **14**(5), 1600253, DOI: 10.1002/pssc.201600253.

42 M. W. Shaikh and D. Varshney, Structural Properties and Electrical Resistivity Behaviour of La 1-x K XMnO 3 (x = 0.1, 0.125 and 0.15) Manganites, *Mater. Chem. Phys.*, 2012, **134**(2–3), 886–898, DOI: 10.1016/j.matchemphys.2012.03.086.

43 J. M. Córdoba, M. Ponce and M. J. Sayagués, Structure Evolution in the LaMn1 − XFexO3 + δ System by Rietveld Analysis, *Solid State Ionics*, 2017, **303**, 132–137, DOI: 10.1016/j.ssi.2017.02.020.

44 A. Maignan, C. Michel, M. Hervieu and B. Raveau, A Monoclinic Manganite, La0.9MnO3−δ, with Colossal Magnetoresistance Properties near Room Temperature, *Solid State Commun.*, 1997, **101**(4), 277–281, DOI: 10.1016/S0038-1098(96)00533-9.

45 S. Zouari, A. Cheikh-Rouhou, P. Strobel, M. Pernet and J. Pierre, Structural and Magnetic Properties of Alkali-Substituted Praseodymium Manganites Pr1−xAxMnO3 (A = Na, K), *J. Alloys Compd.*, 2002, **333**(1–2), 21–27, DOI: 10.1016/S0925-8388(01)01704-2.

46 Z. El-Fadli, E. Coret, F. Sapiña, E. Martinez, A. Beltrán, D. Beltrán and F. Lloret, Low Temperature Synthesis, Structure and Magnetic Properties of La0.85(Na1−xKx)0.15MnO3 Perovskites: The Role of A Cation Size Disparity in the Electronic Properties of Mixed-Valence Manganates, *J. Mater. Chem.*, 1999, **9**(8), 1793–1800, DOI: 10.1039/a901904i.

47 L. D. Mendonca, M. S. Murari and M. D. Daivajna, The Room Temperature Inflection of Magnetism and Anomalous Thermoelectric Power in Lacunar of La0.85 xBixK0.15MnO3, *Phys. Chem. Chem. Phys.*, 2020, **22**(35), 19888–19902, DOI: 10.1039/D0CP03074K.

48 Ramyashri, M. S. Murari and M. D. Daivajna, Expounding the Structural Behaviour of Nd0.5-XNaxSr0.5MnO3 (X = 0, 0.05, 0.10) Manganites, *J. Alloys Compd.*, 2025, 1010, DOI: 10.1016/j.jallcom.2024.177789.

49 O. Z. Yanchevskii, A. I. Tovstolytkin, O. I. V'yunov and A. G. Belous, Structural, Electrical, and Magnetic Properties of La0.7Ca0.3 − x Na x MnO3 ± γ Solid Solutions, *Inorg. Mater.*, 2008, **44**(2), 181–188, DOI: 10.1134/s0020168508020180.

50 G. H. Rao, J. R. Sun, K. Bärner and N. Hamad, Crystal Structure and Magnetoresistance of Na-Doped LaMnO3, *J. Phys.: Condens. Matter*, 1999, **11**(6), 1523–1528, DOI: 10.1088/0953-8984/11/6/016.

51 S. Lee, C. A. Randall and Z. Liu, Modified Phase Diagram for the Barium Oxide–Titanium Dioxide System for the Ferroelectric Barium Titanate, *J. Am. Ceram. Soc.*, 2007, **90**(8), 2589–2594, DOI: 10.1111/j.1551-2916.2007.01794.x.

52 S. Lee, C. A. Randall and Z. Liu, Factors Limiting Equilibrium in Fabricating a Simple Ferroelectric Oxide: BaTiO3, *J. Am. Ceram. Soc.*, 2009, **92**(1), 222–228, DOI: 10.1111/j.1551-2916.2008.02859.x.

53 S. Moharana; T. Badapanda; S. K. Satpathy; R. N. Mahaling and R. Kumar, in *Perovskite Metal Oxides: Synthesis, Properties, and Applications*, ed. G. Korotcenkov, S. Moharana, T. Badapanda, S. K. Satpathy, R. N. Mahaling and R. Kumar, Elsevier, Amsterdam, Netherlands, 2023, vol. 81.

54 J. A. M. van Roosmalen, P. van Vlaanderen, E. H. P. Cordfunke, W. L. IJdo and D. J. W. IJdo, Phases in the Perovskite-Type LaMnO3 + δ Solid Solution and the La2O3-Mn2O3 Phase Diagram, *J. Solid State Chem.*, 1995, **114**(2), 516–523, DOI: 10.1006/jssc.1995.1078.

55 J. M. D. Coey, M. Viret and S. von Molnár, Mixed-Valence Manganites, *Adv. Phys.*, 1999, **48**(2), 167–293, DOI: 10.1080/000187399243455.

56 M. S. Islam, M. Cherry and L. J. Winch, Defect Chemistry of LaBO3(B = Al, Mn or Co) Perovskite-Type Oxides. Relevance to Catalytic and Transport Behaviour, *J. Chem. Soc., Faraday Trans.*, 1996, **92**(3), 479, DOI: 10.1039/ft9969200479.

57 S. L. Ye, W. H. Song, J. M. Dai, K. Y. Wang, S. G. Wang, C. L. Zhang, J. J. Du, Y. P. Sun and J. Fang, Effect of Ag Substitution on the Transport Property and Magnetoresistance of LaMnO3, *J. Magn. Magn. Mater.*, 2002, **248**(1), 26–33, DOI: 10.1016/S0304-8853(02)00017-3.

58 P. R. Nadig, O. Toulemonde, P. Alagarsamy, M. S. Murari and M. D. Daivajna, Multifaceted Roles of Ag+ Ions within and Outside La–Ca–MnO3 Perovskite Manganites: Unveiling the Room Temperature Magnetocaloric Effect, *J. Phys. Chem. C*, 2024, **128**(30), 12686–12703, DOI: 10.1021/acs.jpcc.4c03215.

59 S. Jin, S. Zhang, H. Li, K. Chu, X. Yu, X. Guan, X. Pu and X. Liu, A-Site Na-Doping to Enhance Room-Temperature TCR of La1-Na MnO3 Polycrystalline Ceramics, *Mater. Today Commun.*, 2021, **28**, 102496, DOI: 10.1016/j.mtcomm.2021.102496.

60 R. N. Singh, C. Shivakumara, N. Y. Vasanthacharya, S. Subramanian, M. S. Hegde, H. Rajagopal and A. Sequeira, Synthesis, Structure, and Properties of Sodium or Potassium-Doped Lanthanum Orthomanganites from NaCl or KCl Flux, *J. Solid State Chem.*, 1998, **137**(1), 19–27, DOI: 10.1006/jssc.1997.7653.

61 R. Majumder, M. A. R. Sarker, M. M. Hossain, M. E. Hossain, D. Shen, A. K. M. S. Reza and M. H. Kabir, Investigation of Sodium Doped Lanthanum Manganite in Optical, Dielectric and Capacitive Perspective Prepared by Flux Method, *J. Sci. Res.*, 2019, **11**(2), 195–207, DOI: 10.3329/jsr.v11i2.39351.

62 S. Jin, S. Zhang, H. Li, K. Chu, X. Yu, X. Guan, X. Pu and X. Liu, A-Site Na-Doping to Enhance Room-Temperature TCR of La1-Na MnO3 Polycrystalline Ceramics, *Mater. Today Commun.*, 2021, **28**, 102496, DOI: 10.1016/j.mtcomm.2021.102496.

63 G. Chen, L. Jiang, C. Li, Y. Wei, G. Hu, Y. Yue, X. Wang and J. He, Structural, Magnetic, and Electrical Properties of LaMnO3 Doped with Na by Microwave-Assisted Synthesis Method, *J. Phys.: Conf. Ser.*, 2024, **2842**(1), 012095, DOI: 10.1088/1742-6596/2842/1/012095.

64 M. Palcut, K. Wiik and T. Grande, Cation Self-Diffusion and Nonstoichiometry of Lanthanum Manganite Studied by Diffusion Couple Measurements, *J. Phys. Chem. C*, 2007, **111**(2), 813–822, DOI: 10.1021/jp0642746.

65 E. T. Maguire, A. M. Coats, J. M. S. Skakle and A. R. West, Stoichiometry and Defect Structure of 'NdMnO3', *J. Mater. Chem.*, 1999, **9**(6), 1337–1346, DOI: 10.1039/a900734b.

66 S. Kansara, D. D. Pandya, B. Nimavat, C. M. Thakar, P. S. Solanki, S. Rayprol, M. R. Gonal, N. A. Shah and D. G. Kuberkar, Structure – Transport Correlations in Mono-Valent Na+ Doped La1-XNaxMnO3 Manganites, *Adv. Mater. Res.*, 2013, **665**, 1–7, DOI: 10.4028/www.scientific.net/AMR.665.1.

67 N. V. Dang, T.-L. Phan, T. D. Thanh, V. D. Lam and L. V. Hong, Structural Phase Separation and Optical and Magnetic Properties of BaTi1−xMnxO3 Multiferroics, *J. Appl. Phys.*, 2012, **111**(11), 113913, DOI: 10.1063/1.4725195.

68 N. V. Dang, N. T. Dang, T. A. Ho, N. Tran and T. L. Phan, Electronic Structure and Magnetic Properties of BaTi 1-x Mn x O 3, *Curr. Appl. Phys.*, 2018, **18**(2), 150–154, DOI: 10.1016/j.cap.2017.11.020.

69 J. Akimoto, Y. Gotoh and Y. Oosawa, Refinement of Hexagonal BaTiO3, *Acta Crystallogr., Sect. C:Cryst. Struct. Commun.*, 1994, **50**(2), 160–161, DOI: 10.1107/S0108270193008637.

70 D. C. Sinclair, J. M. S. Skakle, F. D. Morrison, R. I. Smith and T. P. Beales, Structure and Electrical Properties of Oxygen-Deficient Hexagonal BaTiO3, *J. Mater. Chem.*, 1999, **9**(6), 1327–1331, DOI: 10.1039/a900957d.

71 H. D. Megaw, Origin of Ferroelectricity in Barium Titanate and Other Perovskite-Type Crystals, *Acta Crystallogr.*, 1952, **5**(6), 739–749, DOI: 10.1107/S0365110X52002069.

72 M. F. Hundley and J. J. Neumeier, *Phys. Rev. B:Condens. Matter Mater. Phys.*, 1997, **55**, 11511, DOI: 10.1103/PhysRevB.55.11511.

73 P. Orgiani, A. Galdi, C. Aruta, V. Cataudella, G. De Filippis, C. A. Perroni, V. Marigliano Ramaglia, R. Ciancio, N. B. Brookes, M. Moretti Sala, G. Ghiringhelli and L. Maritato, Multiple Double-Exchange Mechanism by Mn2+ Doping in Manganite Compounds, *Phys. Rev. B:Condens. Matter Mater. Phys.*, 2010, **82**(20), 205122, DOI: 10.1103/PhysRevB.82.205122.

74 B. Arun, V. R. Akshay and M. Vasundhara, Observation of Enhanced Magnetic Entropy Change near Room Temperature in Sr-Site Deficient.67Sr0.33MnO3 Manganite, *RSC Adv.*, 2019, **9**(41), 23598–23606, DOI: 10.1039/C9RA04973H.

75 B. Sudakshina, K. K. Supin and M. Vasundhara, Effects of Nd-Deficiency in Nd0.67Ba0.33MnO3 Manganites on Structural, Magnetic and Electrical Transport Properties, *J. Magn. Magn. Mater.*, 2022, **542**, 168595, DOI: 10.1016/j.jmmm.2021.168595.

76 C. Liu, Z. Lan, X. Jiang, Z. Yu, K. Sun, L. Li and P. Liu, Effects of Sintering Temperature and Bi2O3 Content on Microstructure and Magnetic Properties of LiZn Ferrites, *J. Magn. Magn. Mater.*, 2008, **320**(7), 1335–1339, DOI: 10.1016/j.jmmm.2007.10.016.

77 J. F. Moulder; W. F. Stickle; E. Sobal Peter and K. D. Bomben in *Handbook of X-Ray Photoelectron Spectroscopy*, ed. J. Chastain and R. C. King Jr, Perkin-Elmer Corporation, Minnesota, USA, 1992, vol. 40, p. 221. , DOI: 10.1002/0470014229.ch22.

78 S. Kumar, V. S. Raju and T. R. N. Kutty, Investigations on the Chemical States of Sintered Barium Titanate by X-Ray Photoelectron Spectroscopy, *Appl. Surf. Sci.*, 2003, **206**(1–4), 250–261, DOI: 10.1016/S0169-4332(02)01223-0.

79 K. Siemek, A. Olejniczak, L. N. Korotkov, P. Konieczny and A. V. Belushkin, Investigation of Surface Defects in BaTiO3 Nanopowders Studied by XPS and Positron Annihilation Lifetime Spectroscopy, *Appl. Surf. Sci.*, 2022, **578**, 151807, DOI: 10.1016/j.apsusc.2021.151807.

80 P. S. Bagus, C. J. Nelin, C. R. Brundle and S. A. Chambers, A New Mechanism For XPS Line Broadening: The 2p-XPS of Ti(IV, *J. Phys. Chem. C*, 2019, **123**(13), 7705–7716, DOI: 10.1021/acs.jpcc.8b05576.

81 M. F. Sunding, K. Hadidi, S. Diplas, O. M. Løvvik, T. E. Norby and A. E. Gunnæs, XPS Characterisation of in Situ Treated Lanthanum Oxide and Hydroxide Using Tailored Charge Referencing and Peak Fitting Procedures, *J. Electron Spectrosc. Relat. Phenom.*, 2011, **184**(7), 399–409, DOI: 10.1016/j.elspec.2011.04.002.

82 E. Ksepko, E. Talik, A. Ratuszna, A. Molak, Z. Ujma and I. Gruszka, XPS Examination of Newly Obtained (Na0.5Pb0.5)(Mn0.5Nb0.5)O3 Ceramics, *J. Alloys Compd.*, 2005, **386**(1–2), 35–42, DOI: 10.1016/j.jallcom.2004.05.023.

83 D. Salusso, C. Scarfiello, A. Efimenko, D. Pham Minh, P. Serp, K. Soulantica and S. Zafeiratos, Direct Evidence of Dynamic Metal Support Interactions in Co/TiO2 Catalysts by Near-Ambient Pressure X-Ray Photoelectron Spectroscopy, *Nanomaterials*, 2023, **13**(19), 2672, DOI: 10.3390/nano13192672.

84 H. W. Nesbitt and D. Banerjee, Interpretation of XPS Mn(2p) Spectra of Mn Oxyhydroxides and Constraints on the Mechanism of MnO2, *Am. Mineral.*, 1998, **83**(3–4), 305–315, DOI: 10.2138/am-1998-3-414.

85 M. C. Biesinger, B. P. Payne, A. P. Grosvenor, L. W. M. Lau, A. R. Gerson and R. S. C. Smart, Resolving Surface Chemical States in XPS Analysis of First Row Transition Metals, Oxides and Hydroxides: Cr, Mn, Fe, Co and Ni, *Appl. Surf. Sci.*, 2011, **257**(7), 2717–2730, DOI: 10.1016/j.apsusc.2010.10.051.

86 R. P. Gupta and S. K. Sen, Calculation of Multiplet Structure of Core P-Vacancy Levels. II, *Phys. Rev. B*, 1975, **12**(1), 15–19, DOI: 10.1103/PhysRevB.12.15.

87 R. P. Gupta and S. K. Sen, Calculation of Multiplet Structure of Core P-Vacancy Levels, *Phys. Rev. B*, 1974, **10**(1), 71–77, DOI: 10.1103/PhysRevB.10.71.

88 M. G. Elmahgary, A. M. Mahran, M. Ganoub and S. O. Abdellatif, Optical Investigation and Computational Modelling of BaTiO3 for Optoelectronic Devices Applications, *Sci. Rep.*, 2023, **13**(1), 4761, DOI: 10.1038/s41598-023-31652-2.

89 Y. Cui, *Ferroelectric Barium Titanate For Semiconductor Photocatalytic Application*, Queen Mary University of London, 2015. https://qmro.qmul.ac.uk/xmlui/handle/123456789/9530 (accessed 2025-03-29).

90 M. Nageri and V. Kumar, Manganese-Doped BaTiO 3 Nanotube Arrays for Enhanced Visible Light Photocatalytic Applications, *Mater. Chem. Phys.*, 2018, **213**, 400–405, DOI: 10.1016/j.matchemphys.2018.04.003.

91 N. E. Mokhefi, M. Sahnoun, R. Larbi and N. Chelil, Computational Analysis of Hybrid Double Perovskite Materials and Their Potential in Photovoltaic and Thermoelectric Applications, *Phys. Scr.*, 2023, **98**(10), 105965, DOI: 10.1088/1402-4896/acf963.

92 W. D. Mesquita, M. C. de Oliveira, M. Assis, R. A. P. Ribeiro, A. C. Eduardo, M. D. Teodoro, G. E. Marques, M. G. Júnior, E. Longo and M. Fernanda do Carmo Gurgel, Unraveling the Relationship between Bulk Structure and Exposed Surfaces and Its Effect on the Electronic Structure and Photoluminescent Properties of Ba0.5Sr0.5TiO3: A Joint Experimental and Theoretical Approach, *Mater. Res. Bull.*, 2021, **143**, 111442, DOI: 10.1016/j.materresbull.2021.111442.

93 E. Orhan, J. A. Varela, A. Zenatti, M. F. C. Gurgel, F. M. Pontes, E. R. Leite, E. Longo, P. S. Pizani, A. Beltràn and J. Andrès, Room-Temperature Photoluminescence of BaTiO3: Joint Experimental and Theoretical Study, *Phys. Rev. B:Condens. Matter Mater. Phys.*, 2005, **71**(8), 085113, DOI: 10.1103/PhysRevB.71.085113.

94 V. Mishra, A. Sagdeo, V. Kumar, M. K. Warshi, H. M. Rai, S. K. Saxena, D. R. Roy, V. Mishra, R. Kumar and P. R. Sagdeo, Electronic and Optical Properties of BaTiO3 across Tetragonal to Cubic Phase Transition: An Experimental and Theoretical Investigation, *J. Appl. Phys.*, 2017, **122**(6), 065105, DOI: 10.1063/1.4997939.

95 M. Cardona, Optical Properties and Band Structure of SrTiO3 and BaTiO3, *Phys. Rev.*, 1965, **140**(2A), A651–A655, DOI: 10.1103/PhysRev.140.A651.

96 S. Pal, S. Muthukrishnan, B. Sadhukhan, S. NV, D. Murali and P. Murugavel, Bulk Photovoltaic Effect in BaTiO3-Based Ferroelectric Oxides: An Experimental and Theoretical Study, *J. Appl. Phys.*, 2021, **129**(8), 084106, DOI: 10.1063/5.0036488.

97 J. Xu; D. P. Durisin and G. W. Auner, Optical Properties of Pulsed-Laser Deposited BaTiO 3 Thin Films, in *Photon Processing in Microelectronics and Photonics IV*, ed. J. Fieret, P. R. Herman, T. Okada, C. B. Arnold, F. G. Bachmann, W. Hoving, K. Washio, Y. Lu, D. B. Geohegan, F. Trager and J. J. Dubowski, SPIE, 2005, vol. 5713, p. 305. , DOI: 10.1117/12.584639.

98 S. W. Robey; L. T. Hudson; C. Eylem and B. Eichorn, Substitution-Induced Midgap States in the Mixed Oxides R x Ba 1 − x TiO 3 − δ with R = Y, La, and Nd, **vol. 48**. , DOI: 10.1103/PhysRevB.48.562.

99 H. Basantakumar Sharma, Structural and optical properties of sol-gel derived barium titanate thin film, *Int. J. Mod. Phys. B*, 2007, **21**(11), 1837–1849, DOI: 10.1142/S0217979207037028.

100 S. Ramakanth and K. C. James Raju, Band Gap Narrowing in BaTiO3 Nanoparticles Facilitated by Multiple Mechanisms, *J. Appl. Phys.*, 2014, **115**, 173507, DOI: 10.1063/1.4871776.

101 S. Saha, T. P. Sinha and A. Mookerjee, Electronic Structure, Chemical Bonding, and Optical Properties of Paraelectric BaTiO3, *Phys. Rev. B:Condens. Matter Mater. Phys.*, 2000, **62**(13), 8828–8834, DOI: 10.1103/PhysRevB.62.8828.

102 F. M. Michel-Calendini and G. Mesnard, Band Structure and Optical Properties of Tetragonal BaTiO3, *J. Phys. C:Solid State Phys.*, 1973, **6**(10), 1709–1722, DOI: 10.1088/0022-3719/6/10/007.

103 A. A. Valeeva, E. A. Kozlova, A. S. Vokhmintsev, R. V. Kamalov, I. B. Dorosheva, A. A. Saraev, I. A. Weinstein and A. A. Rempel, Nonstoichiometric Titanium Dioxide Nanotubes with Enhanced Catalytical Activity under Visible Light, *Sci. Rep.*, 2018, **8**(1), 9607, DOI: 10.1038/s41598-018-28045-1.

104 J. Hwang, T. Kolodiazhnyi, J. Yang and M. Couillard, Doping and Temperature-Dependent Optical Properties of Oxygen-Reduced BaTiO 3 − δ, *Phys. Rev. B:Condens. Matter Mater. Phys.*, 2010, **82**(21), 214109, DOI: 10.1103/PhysRevB.82.214109.

105 S. Saha, T. P. Sinha and A. Mookerjee, Electronic Structure, Chemical Bonding, and Optical Properties of Paraelectric BaTiO3, *Phys. Rev. B:Condens. Matter Mater. Phys.*, 2000, **62**(13), 8828–8834, DOI: 10.1103/PhysRevB.62.8828.

106 S. W. Robey; L. T. Hudson; C. Eylem and B. Eichorn, Substitution-Induced Midgap States in the Mixed Oxides R Ba & Ti03 8 with R = Y, La, and Nd, **vol. 48**. , DOI: 10.1103/PhysRevB.48.562.

107 P. K. Gogoi and D. Schmidt, Temperature-Dependent Dielectric Function of Bulk SrTiO3: Urbach Tail, Band Edges, and Excitonic Effects, *Phys. Rev. B*, 2016, **93**(7), 075204, DOI: 10.1103/PhysRevB.93.075204.

108 G. Panchal, R. J. Choudhary, S. Yadav and D. M. Phase, Probing the Effect of Ferroelectric to Paraelectric Phase Transition on the Ti-3 d and O-2 p Hybridization in BaTiO3, *J. Appl. Phys.*, 2019, **125**, 214102, DOI: 10.1063/1.5089731.

109 L. Sponza, V. Véniard, F. Sottile, C. Giorgetti and L. Reining, Role of Localized Electrons in Electron-Hole Interaction: The Case of SrTiO3, *Phys. Rev. B:Condens. Matter Mater. Phys.*, 2013, **87**(23), 235102, DOI: 10.1103/PhysRevB.87.235102.

110 X. Huang, T. R. Paudel, S. Dong and E. Y. Tsymbal, Hexagonal Rare-Earth Manganites as Promising Photovoltaics and Light Polarizers, *Phys. Rev. B:Condens. Matter Mater. Phys.*, 2015, **92**(12), 125201, DOI: 10.1103/PhysRevB.92.125201.

111 N. G. Bebenin, N. N. Loshkareva, A. A. Makhnev, E. V. Mostovshchikova, L. V. Nomerovannaya, E. A. Gan'shina, A. N. Vinogradov and Y. M. Mukovskii, Optical and Magneto-Optical Properties of Ferromagnetic La1 − XBaxMnO3 Single Crystals, *J. Phys.: Condens. Matter*, 2010, **22**(9), 096003, DOI: 10.1088/0953-8984/22/9/096003.

112 J. H. Jung, K. H. Kim, D. J. Eom, T. W. Noh, E. J. Choi, J. Yu, Y. S. Kwon and Y. Chung, Determination of Electronic Band Structures of CaMnO 3 and LaMnO 3 Using Optical-Conductivity Analyses, *Phys. Rev. B:Condens. Matter Mater. Phys.*, 1997, **55**(23), 15489–15493, DOI: 10.1103/PhysRevB.55.15489.

113 J. H. Jung; K. H. Kim; H. J. Lee; T. W. Noh; E. J. Choi and Y. Chung, Determination of the LaMnO 3 Band Structure Based on Optical Studies of La 1−x Ca x MnO 3, 1997, **vol. 31**.

114 P. Fumagalli, C. Spaeth, G. Guntherodt, R. von Helmolt and J. Wecker, Magneto-Optic Spectroscopy of Perovskite-Type La1-x(Ba, Sr)x,Mn03, *IEEE Trans. Magn.*, 1995, **31**(6), 3277–3279, DOI: 10.1109/20.490359.

115 A. S. Moskvin and R. V. Pisarev, Optical Spectroscopy of Charge Transfer Transitions in Multiferroic Manganites, Ferrites, and Related Insulators, *Low Temp. Phys.*, 2010, **36**(6), 489–510, DOI: 10.1063/1.3455721.

116 C. Roy and R. C. Budhani, Raman, Infrared and x-Ray Diffraction Study of Phase Stability in La1−xBaxMnO3 Doped Manganites, *J. Appl. Phys.*, 1999, **85**(6), 3124–3131, DOI: 10.1063/1.369651.

117 M. Quijada, J. Černe, J. R. Simpson, H. D. Drew, K. H. Ahn, A. J. Millis, R. Shreekala, R. Ramesh, M. Rajeswari and T. Venkatesan, Optical Conductivity of Manganites: Crossover from Jahn-Teller Small Polaron to Coherent Transport in the Ferromagnetic State, *Phys. Rev. B:Condens. Matter Mater. Phys.*, 1998, **58**(24), 16093–16102, DOI: 10.1103/PhysRevB.58.16093.

118 J. H. Lee, X. Ke, R. Misra, J. F. Ihlefeld, X. S. Xu, Z. G. Mei, T. Heeg, M. Roeckerath, J. Schubert, Z. K. Liu, J. L. Musfeldt, P. Schiffer and D. G. Schlom, Adsorption-Controlled Growth of BiMnO3 Films by Molecular-Beam Epitaxy, *Appl. Phys. Lett.*, 2010, **96**, 262905, DOI: 10.1063/1.3457786.

119 W. Xia, K. Leng, Q. Tang, L. Yang, Y. Xie, Z. Wu and X. Zhu, Comparative Studies on the Structural, Magnetic, and Optical Properties of Perovskite Ln0.67Ca0.33MnO3 (Ln = La, Pr, Nd, and Sm) Manganite Nanoparticles Synthesized by Sol–Gel Method, *AIP Adv.*, 2021, **11**, 035007, DOI: 10.1063/5.0036723.

120 Yu. E. Samoshkina, I. S. Edelman, M. V. Rautskii and M. S. Molokeev, Correlation between Magneto-Optical and Transport Properties of Sr Doped Manganite Films, *J. Alloys Compd.*, 2019, **782**, 334–342, DOI: 10.1016/j.jallcom.2018.12.158.

121 T. D. Rao, T. Karthik and S. Asthana, Investigation of Structural, Magnetic and Optical Properties of Rare Earth Substituted Bismuth Ferrite, *J. Rare Earths*, 2013, **31**(4), 370–375, DOI: 10.1016/S1002-0721(12)60288-9.

122 Y. Jin, Y. Hu, H. Wu, H. Duan, L. Chen, Y. Fu, G. Ju, Z. Mu and M. He, A Deep Red Phosphor Li2MgTiO4:Mn4+ Exhibiting Abnormal Emission: Potential Application as Color Converter for Warm w-LEDs, *Chem. Eng. J.*, 2016, **288**, 596–607, DOI: 10.1016/j.cej.2015.12.027.

123 A. Rusydi, R. Rauer, G. Neuber, M. Bastjan, I. Mahns, S. Müller, P. Saichu, B. Schulz, S. G. Singer, A. I. Lichtenstein, D. Qi, X. Gao, X. Yu, A. T. S. Wee, G. Stryganyuk, K. Dörr, G. A. Sawatzky, S. L. Cooper and M. Rübhausen, Metal-Insulator Transition in Manganites: Changes in Optical Conductivity up to 22 EV, *Phys. Rev. B:Condens. Matter Mater. Phys.*, 2008, **78**(12), 125110, DOI: 10.1103/PhysRevB.78.125110.

124 E. V. Mostovshchikova, S. V. Naumov, A. A. Makhnev, N. I. Solin and S. V. Telegin, Evolution of the Optical Properties and the Electrical Resistivity of CaMnO3 during the Substitution of Mo for Mn Ions, *J. Exp. Theor. Phys.*, 2014, **118**(2), 297–303, DOI: 10.1134/S1063776114010257.

125 E. A. Balykina, E. A. Ganshina, G. S. Krinchik, A. Y. Trifonov and I. O. Troyanchuk, Magneto-Optical Properties of New Manganese Oxide Compounds, *J. Magn. Magn. Mater.*, 1992, **117**(1–2), 259–269, DOI: 10.1016/0304-8853(92)90319-J.

126 R. Rozilah, M. K. Yaakob, Z. Mohamed and A. K. Yahya, Effects of On-Site Coulomb Interaction (U) on the Structural and Electronic Properties of Half-Metallic Ferromagnetic Orthorhombic Pr0.75Na0.25MnO3 Manganite: A LDA + U Calculation and Experimental Study, *Mater. Res. Express*, 2017, **4**(6), 066103, DOI: 10.1088/2053-1591/aa7437.

127 O. Rejaiba, K. Khirouni, M. H. Dhaou, B. Alzahrani, M. L. Bouazizi and J. Khelifi, Investigation Study of Optical and Dielectric Parameters Using Absorption and Diffuse Reflectance Spectroscopy Method on La0.57Nd0.1Sr0.13Ag0.2 MnO3 Perovskite for Optoelectronic Application, *Opt. Quantum Electron.*, 2022, **54**(5), 315, DOI: 10.1007/s11082-022-03633-8.

128 D. Raj and M. V. Manjusha, Synthesis and Optical Characterization of Fe Doped Barium Titanate (BaTiO3) Nanoparticles, *Mater. Today: Proc.*, 2023, DOI: 10.1016/j.matpr.2023.11.131.

129 H. Salehi, N. Shahtahmasebi and S. M. Hosseini, Band Structure of Tetragonal BaTiO3, *Eur. Phys. J. B*, 2003, **32**(2), 177–180, DOI: 10.1140/epjb/e2003-00086-6.

130 H.-F. Cheng, Structural and Optical Properties of Laser Deposited Ferroelectric (Sr0.2Ba0.8)TiO3 Thin Films, *J. Appl. Phys.*, 1996, **79**(10), 7965–7971, DOI: 10.1063/1.362346.

131 M. Cardona, Optical Properties and Band Structure of SrTiO3 and BaTiO3, *Phys. Rev.*, 1965, **140**(2A), A651–A655, DOI: 10.1103/PhysRev.140.A651.

132 H. F. Mohamed, A. M. Ahmed, M. R. Ahmed, J. A. Paixão and S. A. Mohamed, Enhancement of Optical, Electrical, Magnetic, and Thermopower Properties of LaMnO3 by Potassium-Doping, *Phys. Status Solidi B*, 2023, **260**(10), 2300175, DOI: 10.1002/pssb.202300175.

133 S. Selvarajan, P. Malathy, A. Suganthi and M. Rajarajan, Fabrication of Mesoporous BaTiO3/SnO2 Nanorods with Highly Enhanced Photocatalytic Degradation of Organic Pollutants, *J. Ind. Eng. Chem.*, 2017, **53**, 201–212, DOI: 10.1016/j.jiec.2017.04.026.

134 H. Volkova, Photo-Response of Ferroelectric Oxides, Université Paris Saclay, 2019. https://theses.hal.science/tel-02015830v1.

135 F. M. Michel-Calendini and G. Mesnard, Band Structure and Optical Properties of Tetragonal BaTiO3, *J. Phys.*

C:Solid State Phys., 1973, **6**(10), 1709–1722, DOI: 10.1088/0022-3719/6/10/007.

136 F. R. Afje and M. H. Ehsani, Size-Dependent Photocatalytic Activity of La0.8Sr0.2MnO3 Nanoparticles Prepared by Hydrothermal Synthesis, *Mater. Res. Express*, 2018, **5**(4), 045012, DOI: 10.1088/2053-1591/aaba51.

137 R. Korotana, G. Mallia, Z. Gercsi, L. Liborio and N. M. Harrison, Hybrid Density Functional Study of Structural, Bonding, and Electronic Properties of the Manganite Series La1-x Cax MnO3 (X = 0, 14,1), *Phys. Rev. B.*, 2014, **89**(20), 205110, DOI: 10.1103/PhysRevB.89.205110.

138 A. Haoui, M. Elchikh, S. Hiadsi and A. Hireche Baghdad, DFT Analysis of Mechanical, Thermal, Half-Metallic, and Thermoelectric Properties of Perovskites PrMnO3 and NdMnO3 Ortho-Manganite, *Phys. B*, 2024, **684**, 416001, DOI: 10.1016/j.physb.2024.416001.

139 A. Madani, M. Alghamdi, B. Alamri and S. Althobaiti, Structural and Optical Properties of Sb–BaTiO3 and Y– BaTiO3 Doped Ceramics Prepared by Solid-State Reaction, *Opt. Mater.*, 2023, **137**, 113480, DOI: 10.1016/j.optmat.2023.113480.

140 M. Moustafa, A. Wasnick, C. Janowitz and R. Manzke, Temperature Shift of the Absorption Edge and Urbach Tail of ZrSxSe2−x Single Crystals, *Phys. Rev. B*, 2017, **95**(24), 245207, DOI: 10.1103/PhysRevB.95.245207.

141 A. Canul, D. Thapa, J. Huso, L. Bergman, R. Vaughan Williams and R. Machleidt, Mixed-Strategy Approach to Band-Edge Analysis and Modeling in Semiconductors, *Phys. Rev. B*, 2020, **101**(19), 195308, DOI: 10.1103/PhysRevB.101.195308.

142 A. E. Rakhshani, Study of Urbach Tail, Bandgap Energy and Grain-Boundary Characteristics in CdS by Modulated Photocurrent Spectroscopy, *J. Phys.: Condens. Matter*, 2000, **12**(19), 4391–4400, DOI: 10.1088/0953-8984/12/19/309.

143 A. Canul, D. Thapa, J. Huso, L. Bergman, R. Vaughan Williams and R. MacHleidt, Mixed-Strategy Approach to Band-Edge Analysis and Modeling in Semiconductors, *Phys. Rev. B*, 2020, **101**(19), 195308, DOI: 10.1103/PhysRevB.101.195308.

144 J. Yang, Y. Gao, Z. Huang, X. Meng, M. Shen, H. Yin, J. Sun and J. Chu, Dielectric Functions of Ferroelectric Pb0.5Sr0.5TiO3 Film Determined by Transmittance Spectroscopy, *J. Phys. D: Appl. Phys.*, 2009, **42**(21), 215403, DOI: 10.1088/0022-3727/42/21/215403.

145 A. Jana, S. Ram and T. K. Kundu, BaTiO3 Nanoparticles of Orthorhombic Structure Following a Polymer Precursor. Part I. X-Ray Diffraction and Electron Paramagnetic Resonance, *Philos. Mag.*, 2007, **87**(35), 5485–5495, DOI: 10.1080/14786430701689721.

146 J. Wu and C. Leighton, Glassy Ferromagnetism and Magnetic Phase Separation in La1xSrxCoO3, *Phys. Rev. B:Condens. Matter Mater. Phys.*, 2003, **67**(17), 174408, DOI: 10.1103/PhysRevB.67.174408.

147 A. Raeliarijaona and H. Fu, Ferromagnetism in Ferroelectric BaTiO3 Induced by Vacancies: Sensitive Dependence on Charge State, Origin of Magnetism, and Temperature Range of Existence, *Phys. Rev. B*, 2017, **96**(14), 144431, DOI: 10.1103/PhysRevB.96.144431.

148 D. Cao, M. Q. Cai, Y. Zheng and W. Y. Hu, First-Principles Study for Vacancy-Induced Magnetism in Nonmagnetic Ferroelectric BaTiO3, *Phys. Chem. Chem. Phys.*, 2009, **11**(46), 10934, DOI: 10.1039/b908058a.

149 P. Esther Rubavathi, M. Veera Gajendra Babu, B. Bagyalakshmi, L. Venkidu, D. Dhayanithi, N. V. Giridharan and B. Sundarakannan, Impact of Ba/Ti Ratio on the Magnetic Properties of BaTiO3 Ceramics, *Vacuum*, 2019, **159**, 374–378, DOI: 10.1016/j.vacuum.2018.10.063.

150 J. Wu, Magnetoresistance Effects for the Inhomogeneous Perovskite System of Ag Doped La0.833Na0.167MnO3, *Appl. Mech. Mater.*, 2011, **110–116**, 553–558, DOI: 10.4028/www.scientific.net/AMM.110-116.553.

151 K. De, S. Majumdar and S. Giri, Magnetic and Electrical Transport Properties of La0.87Mn1−xFexO3 ($0 \leq x \leq 0.15$): Coexistence of Ferromagnetic and Glassy Magnetic States, *J. Phys. D: Appl. Phys.*, 2007, **40**(19), 5810–5818, DOI: 10.1088/0022-3727/40/19/002.

152 Z. H. Wang, G. L. Yu, Y. Nie, Z. F. Wu, L. Qiu, Z. Luo and J. Gao, Effect of Applied Magnetic Field on the Rectifying Characteristics in Self-Doped La0.9MnO3/0.8wt%Nb–SrTiO3 Heteroepitaxial Junctions, *J. Appl. Phys.*, 2008, **103**, 07A913, DOI: 10.1063/1.2836964.

153 P. A. Joy, C. R. Sankar and S. K. Date, The Limiting Value of x in the Ferromagnetic Compositions La1−xMnO3, *J. Phys.: Condens. Matter*, 2002, **14**(39), L663–L669, DOI: 10.1088/0953-8984/14/39/104.

154 V. Ferris, G. Goglio, L. Brohan, O. Joubert, P. Molinie, M. Ganne and P. Dordor, Transport Properties and Magnetic Behavior in the Polycrystalline Lanthanum-Deficient Manganate Perovskites ($\approx$ La1−xMnO3), *Mater. Res. Bull.*, 1997, **32**(6), 763–777, DOI: 10.1016/S0025-5408(97)00044-5.

155 M. Patra, K. De, S. Majumdar and S. Giri, Multifunctionality Attributed to the Self-Doping in Polycrystalline La0.9MnO3: Coexistence of Large Magnetoresistance and Magnetocaloric Effect, *Appl. Phys. Lett.*, 2009, **94**, 092506, DOI: 10.1063/1.3095519.

156 S. L. Ye, W. H. Song, J. M. Dai, K. Y. Wang, S. G. Wang, J. J. Du, Y. P. Sun, J. Fang, J. L. Chen and B. J. Gao, Large Room-Temperature Magnetoresistance and Phase Separation in La1−xNaxMnO3 with $0.1 \leq x \leq 0.3$, *J. Appl. Phys.*, 2001, **90**(6), 2943–2948, DOI: 10.1063/1.1396823.

157 A. Ghosh, S. Paul and S. Raj, Understanding Bifurcations in FC–ZFC Magnetization of Dilutely Fe3+ Doped CdS Nanoparticles, *Solid State Commun.*, 2015, **208**, 1–6, DOI: 10.1016/j.ssc.2015.02.010.

158 P. Tiwari, S. A. Atkar, P. Sharma, A. Datta, A. D. Singha, M. Roy-Chowdhury, T. Sarkar and S. Thota, Field-Induced Spin-State Transition, Critical Exponents and Non-Equilibrium-Memory Effects in Semi Spin-Glass Perovskite (LaNd)(CoMn)O3, *J. Phys. D: Appl. Phys.*, 2025, **58**(15), 155301, DOI: 10.1088/1361-6463/adb417.

159 S. Ghanta, A. Das, P. P. Jana, S. Vrtnik, D. Gačnik, J. Luzar, A. Jelen, P. Koželj, M. Wencka and J. Dolinšek, Structure and Spin Glass Magnetism of the MnxNi2Zn11−x Pseudobinary Γ Brasses at Low Mn Contents, *Inorg. Chem.*, 2021,

60(16), 12226–12236, DOI: 10.1021/acs.inorgchem.1c01418.

160 A. Karmakar, S. Majumdar and S. Giri, Structural and Magnetic Properties of Spontaneously Phase-Separated Eu0.5Sm0.5MnO3, *J. Phys.: Condens. Matter*, 2011, **23**(13), 136003, DOI: 10.1088/0953-8984/23/13/136003.

161 N. A. Viglin, S. V. Naumov and Ya. M. Mukovskii, A Magnetic Resonance Study of La1−x SrxMnO3 Manganites, *Phys. Solid State*, 2001, **43**(10), 1934–1940, DOI: 10.1134/1.1410634.

162 C. Autret-Lambert, M. Gervais, S. Roger, F. Gervais, M. Lethiecq, N. Raimboux and P. Simon, Inhomogeneous Magnetism Studied by ESR in La1-XSrxMnO3 ($0.45 \leq x \leq 0.62$), *Solid State Sci.*, 2017, **71**, 139–145, DOI: 10.1016/j.solidstatesciences.2017.06.017.

163 S. Duhalde, M. F. Vignolo, F. Golmar, C. Chiliotte, C. E. R. Torres, L. A. Errico, A. F. Cabrera, M. Rentería, F. H. Sánchez and M. Weissmann, Appearance of Room-Temperature Ferromagnetism in Cu-Doped TiO2−δ Films, *Phys. Rev. B:Condens. Matter Mater. Phys.*, 2005, **72**(16), 161313, DOI: 10.1103/PhysRevB.72.161313.

164 M. Arshad, M. Abushad, M. Azhar, H. Ahmed, M. Nadeem, A. Ansari, V. K. Chakradhary, S. Husain and W. Khan, Origin of Enhanced Dielectric and Multiferroic Properties in Pb-Doped BaTiO3 Ceramics, *Appl. Phys. A:Mater. Sci. Process.*, 2022, **128**(12), 1123, DOI: 10.1007/s00339-022-06239-9.

165 K. Binder and A. P. Young, Spin Glasses: Experimental Facts, Theoretical Concepts, and Open Questions, *Rev. Mod. Phys.*, 1986, **58**(4), 801–976, DOI: 10.1103/RevModPhys.58.801.

166 A. Malinowski, V. L. Bezusyy, R. Minikayev, P. Dziawa, Y. Syryanyy and M. Sawicki, Spin-Glass Behavior in Ni-Doped La1.85Sr0.15CuO4, *Phys. Rev. B:Condens. Matter Mater. Phys.*, 2011, **84**(2), 024409, DOI: 10.1103/PhysRevB.84.024409.

167 Q. Zhang, D. Li, W. B. Cui, J. Li and Z. D. Zhang, Magnetic Properties and Spin-Glass-like Behavior in Stoichiometric Mn3In Compound, *J. Appl. Phys.*, 2009, **106**, 113915, DOI: 10.1063/1.3266016.

168 K. S. Sivaranjani, G. A. Jacob and R. J. Joseyphus, Comprehensive Law-of-Approach-to-Saturation for the Determination of Magnetic Anisotropy in Soft Magnetic Materials, *Phys. Status Solidi B*, 2022, **259**(10), 2200050, DOI: 10.1002/pssb.202200050.

169 D. J. Dunlop, A Method of Determining Demagnetizing Factor from Multidomain Hysteresis, *J. Geophys. Res.:Solid Earth*, 1984, **89**(B1), 553–558, DOI: 10.1029/JB089iB01p00553.

170 R. N. Bhowmik, S. Kazhugasalamoorthy and A. K. Sinha, Role of Initial Heat Treatment of the Ferrite Component on Magnetic Properties in the Composite of Ferrimagnetic Co1.75Fe1.25O4 Ferrite and Non-Magnetic BaTiO3 Oxide, *J. Magn. Magn. Mater.*, 2017, **444**, 451–466, DOI: 10.1016/j.jmmm.2017.08.061.

171 Y. Machakanti, K. Chandra Babu Naidu, D. Baba Basha, C. Madunuri, N. Suresh Kumar, A. Ratnamala and A. Khan, Low-Temperature Hydrothermal Synthesis of NiEuFe2O4 Nanoparticles: Magnetic, Thermal, and Magneto-Dielectric Behavior, *Int. J. Appl. Ceram. Technol.*, 2023, 1–12, DOI: 10.1111/ijac.14574.

172 E. C. Devi and S. D. Singh, Tracing the Magnetization Curves: A Review on Their Importance, Strategy, and Outcomes, *J. Supercond. Novel Magn.*, 2021, **34**(1), 15–25, DOI: 10.1007/s10948-020-05733-6.

173 G. J. Kumar, M. Sarathbavan, E. S. Kumar, M. Navaneethan and K. K. Bharathi, Structural, Chemical and Low-Temperature Magnetic Properties of Lead-Free 0.6NiFe2O4-0.4Na0.5Bi0.5-TiO3 Magnetoelectric Composite, *J. Mater. Sci.:Mater. Electron.*, 2022, **33**(11), 8344–8354, DOI: 10.1007/s10854-021-06184-y.

174 G. Datt, M. M. Raja and A. C. Abhyankar, Steering of Magnetic Interactions in Ni0.5Zn0.5Fe2- x(Mn) XO4Nanoferrites via Substitution-Induced Cationic Redistribution, *J. Phys. Chem. C*, 2021, **125**(19), 10693–10707, DOI: 10.1021/acs.jpcc.1c01606.

175 V. Rajeevan and R. Justin Joseyphus, Structural and Magnetic Properties of Ni Substituted FeCo Alloy Obtained through Polyol Process, *J. Magn. Magn. Mater.*, 2022, **563**, 170016, DOI: 10.1016/j.jmmm.2022.170016.

176 Y. B. Zainal, Dedi and A. Manaf, Microstructure and Microwave Absorption Characteristics of Batio3-Cofe2o4 Composites, *Key Eng. Mater.*, 2020, **855 KEM**, 322–329, DOI: 10.4028/www.scientific.net/KEM.855.322.

177 R. Ramadan, G. A. Alzaidy, F. N. Almutairi and V. Uskoković, Comparative Analysis of Adsorption of Pb(II) Ions by Different Hexagonal Nanoferrites Synthesized Using the Flash-Combustion Method, *Appl. Phys. A: Mater. Sci. Process.*, 2023, **129**(11), 753, DOI: 10.1007/s00339-023-06976-5.

178 G. Channagoudra, S. Gupta and V. Dayal, Study of Structural, Transport and Magneto-Crystalline Anisotropy in La1-XSrxMnO3($0.30 \leq x \leq 0.40$) Perovskite Manganites, *AIP Adv.*, 2021, **11**, 025305, DOI: 10.1063/9.0000119.

179 R. E. Cohen and H. Krakauer, Lattice Dynamics and Origin of Ferroelectricity in BaTiO3. Linearized-Augmented-Plane-Wave-Energy Calculations, *Phys. Rev. B:Condens. Matter Mater. Phys.*, 1990, **42**(10), 6416–6423, DOI: 10.1103/PhysRevB.42.6416.

180 L. Jin, F. Li and S. Zhang, Decoding the Fingerprint of Ferroelectric Loops: Comprehension of the Material Properties and Structures, *J. Am. Ceram. Soc.*, 2014, **97**(1), 1–27, DOI: 10.1111/jace.12773.

181 K. Banerjee and S. Asthana, Scaling Behavior of Different Shapes of Hysteresis Loops and Recoverable Energy Storage Density in Na0.5Bi0.5TiO3, K0.5Bi0.5TiO3, and Na0.25K0.25Bi0.5TiO3 Ferroelectrics, *J. Materiomics*, 2022, **8**(4), 918–927, DOI: 10.1016/j.jmat.2021.12.007.

182 A. Li, C. Ge, P. Lü, D. Wu, S. Xiong and N. Ming, Fabrication and Electrical Properties of Sol-Gel Derived BaTiO3 Films with Metallic LaNiO3 Electrode, *Appl. Phys. Lett.*, 1997, **70**(12), 1616–1618, DOI: 10.1063/1.118633.

183 P. C. Joshi and S. B. Desu, Structural, Electrical, and Optical Studies on Rapid Thermally Processed Ferroelectric BaTiO3 Thin Films Prepared by Metallo-Organic Solution Deposition Technique, *Thin Solid Films*, 1997, **300**(1–2), 289–294, DOI: 10.1016/S0040-6090(96)09468-0.

184 X. Li, Y. Wang, Y. Rao, X. Ma, Y. Yang and J. Zhang, Enhanced Energy Storage in PVDF-Based Nanocomposite Capacitors through (00l) Oriented BaTiO3 Single-Crystal Platelets, *ACS Appl. Mater. Interfaces*, 2024, **16**(21), 27785–27793, DOI: 10.1021/acsami.4c04340.

185 M. M. Hoque, M. T. Islam, M. R. Islam and M. A. Zubair, Effective Bandgap Tuning with Non-Trivial Modulation in Room Temperature Magnetic and Electrical Responses of Low Level Ba–Cr Co-Substituted BiFeO3 Nanoparticles, *Ceram. Int.*, 2022, **48**(14), 19583–19596, DOI: 10.1016/j.ceramint.2022.03.067.

186 A. Z. Simões, L. S. Cavalcante, F. Moura, E. Longo and J. A. Varela, Structure, Ferroelectric/Magnetoelectric Properties and Leakage Current Density of (Bi0.85Nd0.15)FeO3 Thin Films, *J. Alloys Compd.*, 2011, **509**(17), 5326–5335, DOI: 10.1016/j.jallcom.2011.02.030.

187 J. Ramesh, S. S. K. Reddy, N. Raju, M. S. Reddy, C. G. Reddy, P. Y. Reddy, K. R. Reddy and V. R. Reddy, The Electrical, Magnetic and 57Fe Mössbauer Studies of Al Doped PrFeO3 Polycrystalline Materials, *Ceram. Int.*, 2018, **44**(16), 19314–19318, DOI: 10.1016/j.ceramint.2018.07.159.

188 S. Mishra and S. K. Parida, Lead-Free Complex Double Perovskite SrLiFeWO6: Structural, Microstructure, Electrical and Optical Study, *Phys. B*, 2023, 668, DOI: 10.1016/j.physb.2023.415246.